Title

High repetition rate exploration of Biermann battery generated magnetic fields in vacuum and hydrodynamic shock waves

Author

Pilgram, Jessica Jean

Publication Date

2023

Peer reviewed|Thesis/dissertation

UNIVERSITY OF CALIFORNIA
Los Angeles

High repetition rate exploration of Biermann battery generated magnetic fields in vacuum and hydrodynamic shock waves

A dissertation submitted in partial satisfaction
of the requirements for the degree
Doctor of Philosophy in Physics

by

Jessica Jean Pilgram

2023

ABSTRACT OF THE DISSERTATION

High repetition rate exploration of Biermann battery generated magnetic fields in vacuum and hydrodynamic shock waves

by

Jessica Jean Pilgram
Doctor of Philosophy in Physics
University of California, Los Angeles, 2023
Professor Christoph Niemann, Chair

Magnetic fields are ubiquitous throughout the Universe, but the origin of cosmic and galactic magnetic fields is still under investigation. One theorized source of cosmic magnetic seed fields, which also occurs in many astrophysical and laboratory plasma environments, is the Biermann battery effect. This is a thermoelectric effect that spontaneously generates magnetic fields due to non-parallel electron temperature and density gradients in a plasma. In this dissertation, we present high repetition rate, three-dimensional investigations of the Biermann battery effect in laser-generated plasmas and laser-driven hydrodynamic shock waves. Magnetic field measurements revealed azimuthally symmetric magnetic fields reaching values up to 60 G in vacuum and up to 350 G in the presence of laser-driven Sedov-Taylor shock waves. Two-dimensional Thomson scattering measurements of electron temperature and density in laser-driven shock waves revealed electron temperatures up to 25 eV and electron densities up to $2 \times 10^{16}\ cm^{-3}$. 2D Thomson scattering measurements were used to obtain the novel measurements of electron temperature and density gradients within a plasma. The gradients were used to calculate a theoretical value of the Biermann fields due to the laser-driven shock waves, which was in general agreement with the experimental measurements, confirming that magnetic fields are generated by shock waves. Preliminary uncalibrated 3D FLASH simulations were generally in agreement with the experiments, from which we conclude that the majority of the fields measured in the shock waves are due to

magnetic field generation by the Biermann battery effect. Dimensionless parameters were used to compare the laboratory experiments with astrophysical systems. The Reynolds and magnetic Reynolds numbers in the shock fronts were found to be much larger than unity, as in many astrophysical systems. A comparison of the experimental R_m and R_e with several astrophysical systems revealed that our experiments may be relevant to supernova remnant shocks, stellar atmospheres, and protogalactic and primordial magnetic field generation.

The dissertation of Jessica Jean Pilgram is approved.

Troy A. Carter

Petros Tzeferacos

Smadar Naoz

Christoph Niemann, Committee Chair

University of California, Los Angeles

2023

Table of Contents

1 Introduction **1**

2 The Biermann Battery Effect Theory **7**

2.1 The Induction Equation 7

2.2 MHD Treatment of the Biermann Battery Effect 8

2.3 Laser Produced Plasmas 12

2.4 Scaling to Astrophysics 14

3 Experimental Design **18**

3.1 Heater Beam 20

3.2 Magnetic Flux Probes 22

3.2.1 Magnetic Flux Probe Calibration 23

3.2.2 Voltage conversion to magnetic field 24

3.3 Self-emission Imaging 25

3.4 Optical Thomson Scattering 26

3.4.1 Scattering from electrons 27

3.4.2 Collective Thomson scattering 30

3.4.3 Non-collective Thomson scattering 30

3.4.4 Thomson Scattering Setup 33

3.4.5 Absolute calibration of Thomson scattering system 36

3.4.6 Automatic alignment and data collection technique 38

4 Experimental Results and Discussion **42**

4.1 Mapping of Biermann-Generated Fields in Vacuum 42

4.2 Characterization of Shock Waves via Self-Emission Images 46
4.2.1 Blast Wave Characterization 49
4.3 Thomson scattering measurements of laser induced blast waves 52
4.3.1 One dimensional Thomson scattering measurements 55
4.3.2 Two dimensional Thomson scattering measurements 60
4.4 Biermann Battery in Shock Fronts 64
4.5 Comparison to FLASH simulations 70
4.5.1 Vacuum data comparison to FLASH simulations 70
4.5.2 3D FLASH simulations in the presence of Shock waves 77
4.6 Relevance to Astrophysics 83

5 Conclusions 87
5.1 Future Directions 89

A Magnetic Flux Probe Building Guide 92
A.1 Materials 92
A.2 Winding the wires 93
A.3 Feeding wires through the probe shaft 94
A.4 Soldering the wires 96
A.5 Testing the probe 97
A.6 Final Steps 99

B Additional Data 100

C Diversity, Equity and Inclusion Involvement 108

References 112

List of Figures

2.1 Conceptual diagram of how the Biermann battery effect occurs in laser produced plasmas 13

3.1 Top down view of experiemental set up 19

3.2 Orientation of data planes 19

3.3 Images of vacuum chamber 20

3.4 Image of the Peening Laser 21

3.5 Magnetic flux probe calibration plots 23

3.6 Representative Thomson scattering spectra 31

3.7 Thomson scattering set up 34

3.8 Spectrum used for absolute Raman calibration of TS scattering diagnostic . 39

4.1 Contour plots of measured azimuthal magnetic field and current density . . . 43

4.2 Maximum measured B vs distance from target 44

4.3 Streak plot determining speed of magnetic field propagation 45

4.4 Maximum B vs time 46

4.5 Self-emission images at t=100 ns after laser fire in various pressures of N_2 gas 48

4.6 Self-emission images at t=100 ns after laser fire in various pressures of He gas 49

4.7 Streak plots of shock wave position vs distance from the target in 95 mTorr N_2 and 510 mTorr He 50

4.8 Mach number vs time of the Sedov-Taylor blast waves for N_2 and He. 51

4.9 Abel inversions of a line-out of pixels along the y-axis for images taken at various pressures of N_2 gas. 53

4.10 Abel inversions of a line-out of pixels along the y-axis for images taken at various pressures of He gas. 54
4.11 Thomson scattering spectra 56
4.12 Measured parameters of blast waves in N_2 and He background gas at $t = 100 \pm 5$ ns vs pressure. 57
4.13 Comparison of T_e and n_e in vacuum, 95 mTorr N_2 and 95 mTorr He 59
4.14 y line-outs of n_e and T_e for various times after heater beam fire 61
4.15 Two dimensional map of n_e and T_e in Sedov-Taylor blast waves 62
4.16 n_e and T_e gradients in 95 mTorr N_2 background gas 63
4.17 Calculated $\partial B/\partial t$ from electron temperature and density gradients for 95 mTorr of N_2 64
4.18 Comparison of a B-dot trace in Vacuum (blue) and 95 mTorr of N_2 gas (black) at (x,y,z) = (12,11,1) mm 65
4.19 Contour plots of the magnitude of the magnetic field in an YZ plane at $x =$ 0 mm for various times after heater beam fire. 66
4.20 B_x component of magnetic field measurements at t=100 ns in XZ and YZ planes 67
4.21 Magnetic field magnitude at t=100 ns after heater beam fire in three different planes 68
4.22 Comparison between TS dB/dt and B-dot dB/dt 69
4.23 Vacuum simulation Initialization 71
4.24 Plasma parameters from vacuum FLASH Simulations 73
4.25 Simulation values of Magnetic field at t=150 ns after laser fire 74
4.26 Comparison of shock wave propagation speed of a streak plot in 95 mTorr of N_2 background gas and FLASH simulations 78
4.27 Comparison of experiment and FLASH simulation n_e and T_e 79

4.28 2D contours of electron and ion temperature from FLASH simulations 80

4.29 2D contours of B_{mag} from FLASH simulations with Biermann on and off. . . 82

4.30 Comparison between B_{mag} from FLASH simulations with the Biermann term on and off 82

4.31 Parameters from FLASH simulations used to calculate n_i and T_i 83

4.32 Contour plots of R_e and R_m calculated using 2D TS data 84

A.1 Examples of b-dot winding 95

A.2 b-dot assembly before soldering 96

A.3 Example for how wires should be soldered to board 98

A.4 Picture of set up for testing probe 99

B.1 Orientation of data planes (translucent orange planes) with respect to the laser path and LPP blow-off axis 100

B.2 Contour plots of the B_x component of magnetic field measurements in an XZ plane at $y = 11$ mm for various times after heater beam fire 101

B.3 Contour plots of the B_z component of magnetic field measurements in an XZ plane at $y = 11$ mm for various times after heater beam fire 102

B.4 Contour plots of the magnitude of the measured magnetic fields in an XZ plane at $y = 11$ mm for various times after heater beam fire 103

B.5 Contour plots of the B_x component of magnetic field measurements in an YZ plane at $x = 0$ mm for various times after heater beam fire 104

B.6 Contour plots of the B_z component of magnetic field measurements in an XY plane at $z = -0.5$ mm for various times after heater beam fire 105

B.7 Contour plots of B_{mag} measurements in an XY plane at $z = -0.5$ mm for various times after heater beam fire 106

B.8 Magnetic field magnitude at t=100 ns after heater beam fire in three planes 107

List of Tables

4.1 Table comparing experimental and simulated plasma quantities to astrophysical systems 85

Acknowledgments

This work is supported by the Department of Energy (DOE) under award number DE-SC0019011, the National Nuclear Security Administration (NNSA) Center for Matter Under Extreme Conditions under Award Number DE-NA0003842 and the National Science Foundation Graduate Fellowship Research Program under award number DGE-1650604. The Flash Center for Computational Science acknowledges support by the U.S. DOE NNSA under Subcontracts No. 536203 and 630138 with Los Alamos National Laboratory, Subcontract B632670 with LLNL, and support from the Cooperative Agreement DE-NA0003856 to the Laboratory for Laser Energetics University of Rochester. We thank the University of Rochester's Center for Integrated Research Computing (CIRC). We also thank NIWC Pacific and Curtiss-Wright MIC for help with the slab laser system.

Thank you to the members of UCLA HEDP group, Chris Niemann, Carmen Constantin, Derek Schaeffer, Robert Dorst, and Lucas Rovige for your help and guidance. A special thanks my simulation collaborators, Marissa B.P. Adams, Tristan Bachmann, and Petros Tzeferacos at the Flash Center at the University of Rochester. Their simulations inspired the investigation of Biermann fields in blast waves and provided valuable insight into the physics we were exploring.

I give thanks to God for all of my blessings, especially my family and friends that have supported me through this journey. Thank you to my brother, Nick Pilgram, you are my biggest supporter and I would not be where I am today without you. I also want to thank my parents, Mark and Kathleen Pilgram, for your unconditional love and support through all of my pursuits in life. Thank you to my best friend, Dana Morshead, for your unconditional support, love, and compassion. A special thank you to Noah Miller and Juan Pablo Gatica, both of you cared for me when I did not know how to care for myself, and I am eternally grateful. Lastly, I want to acknowledge and thank the rest of my LA family; Kristian Barajas, Caroline Riley, Leah Phillips, Robert Dorst, Sophie Crisp, and Rory Bentley. Your support and friendship have truly been a highlight of my PhD journey.

Vita

2017 B.S. (Physics), California Polytechnic State University, San Luis Obispo

2020 M.S. (Physics), University of California, Los Angeles

2020-2023 Fellowship, Graduate Research Fellowship Program, National Science Foundation.

Publications

H. Zhang, J. J. Pilgram, C.G. Constantin, L. Rovige, P.V. Heuer, S. Ghazaryan, M. Kaloyan, R.S. Dorst, D.B. Schaeffer, C. Niemann, *Two-Dimensional Thomson Scattering in Laser-Produced Plasmas*, Instruments, 7(3), 25, (2023) https://doi.org/10.3390/instruments7030025

J.J. Pilgram, M.B.P. Adams,C.G. Constantin, P.V. Heuer, S. Ghazaryan, M. Kaloyan, R.S. Dorst, D.B. Schaeffer, P. Tzeferacos, C. Niemann. "High Repetition Rate Exploration of the Biermann Battery Effect in Laser Produced Plasmas Over Large Spatial Regions", High Power Laser Science and Engineering, Cambridge University Press (2022) p.1–11, 10.1017/hpl.2022.2

J. J. Pilgram, M. I. Syed, M. Tajrian, and A. Kreide, *Student voices and experiences on DEI.* California Classroom Science (https://classroomscience.org/articles/fyi/student-voices-and-experiences-dei), Feb 18, 2022

M. Kaloyan, S. Ghazaryan, C. G. Constantin, R. S. Dorst, P. V. Heuer, J. J. Pilgram, D. B. Schaeffer, and C. Niemann , "Raster Thomson scattering in large-scale laser plas-

mas produced at high repetition rate", Review of Scientific Instruments 92, 093102 (2021) https://doi.org/10.1063/5.0059244

R. S. Dorst, C. G. Constantin, D. B. Schaeffer, J. J. Pilgram, and C. Niemann , "Planar laser induced fluorescence mapping of a carbon laser produced plasma", Review of Scientific Instruments 93, 103518 (2022) https://doi.org/10.1063/5.0099171

R. S. Dorst, D. B. Schaeffer, A. Le, J. J. Pilgram, C. G. Constantin, S. Vincena, S. K. P. Tripathi, D. Winske, D. Larson, M. Cowee, and C. Niemann , "High repetition rate mapping of the interaction between a laser plasma and magnetized background plasma via laser induced fluorescence", Physics of Plasmas 29, 082113 (2022) https://doi.org/10.1063/5.0097748

CHAPTER 1

Introduction

Magnetic fields are present throughout the universe on various scales, from planets and stars to galaxies and galaxy clusters. Having a good understanding of the generation and amplification of these fields allows us to obtain better understanding of the cosmological evolution of the universe and the structure of the magnetic fields that are currently observed. Moreover, the mechanisms responsible for producing magnetic fields are themselves astronomically significant and intriguing. Magnetic fields affect the properties of the interstellar medium, play a critical role in star formation, participate in the origin and confinement of cosmic rays, potentially influence the formation and evolution of galaxies, and contribute to the balance and stability of galactic disks.[51]. Magnetic fields also have an impact on astrophysical shocks resulting from phenomena such as gamma-ray bursts, jets from active galactic nuclei, and supernova remnants. On a solar system scale, magnetic fields facilitate the bow shocks between the solar wind and Earth's magnetosphere, and participate in magnetic reconnection processes[59]. Although magnetic fields pervade the universe, the origin of galactic and cosmic magnetic fields is still somewhat of a mystery[51].

It is widely accepted that magnetic fields were not formed during the Big Bang[51]. Instead, it is hypothesized that magnetic fields were produced during the recombination phase of our universe at a level of 10^{-20} G and then amplified through various processes to the current observed level of 10^{-6} G[51]. There are two primary theories on the origin of magnetic fields in the present era: dynamo theory and primordial theory. The dynamo theory posits that magnetic fields attain their presently-observed values through magnification of small initial seed fields via large-scale plasma flows and small-scale turbulent flows[105].

Primordial theory, on the other hand, conjectures that galactic disks initially are endowed with large-scale micro-Gauss magnetic fields when they form. These fields then evolve over time solely through advection by plasma flow[105]. Both theories require further magnetic field sources. Moreover, astrophysical observations do not provide solid backing for either theory[105].

To comprehend the amplification of the fields to their current state, it is necessary to understand the origin of the fields themselves. Various mechanisms have been proposed as the origin of the primordial magnetic seed fields. These mechanisms include, but are not limited to, the Weibel instability, in which magnetic fields arise due to temperature anisotropy within a plasma, the creation of magnetic fields through the acceleration of cosmic rays[66], and the Biermann battery effect[51, 105, 67].

The Biermann battery effect was first described by Ludwig Biermann in 1949[3]. This thermoelectric process generates magnetic fields in plasmas through non-parallel temperature and density gradients which result from an electron pressure gradient in plasma ejections such as laser produced plasmas. Electrons within the plasma flow down this pressure gradient at high velocities relative to the heavier ion species, causing charge separation and an electromotive force (EMF). Following Faraday's law, this EMF generates a magnetic flux, thereby spontaneously creating a magnetic field.

The Biermann battery effect is a prominent theory for producing cosmic fields since it can generate fields on both small scales, such as in objects like accretion disks, and on large cosmological scales.[104] Additionally, simulations by Naoz and Narayan [67] suggest that the Biermann battery effect generated seed fields in the early universe sooner than previously suggested. This would allow for more time to amplify the weak Biermann seed fields. Schoeffler et al.'s simulations[83, 84] further promote the Biermann battery effect as a source of cosmic seed fields. Their simulations suggest that seed fields generated by the Biermann battery mechanism could have been pre-amplified by the Weibel instability before amplification by the dynamo effect, thus allowing even the smallest Biermann seed fields to produce the observed magnetic field magnitudes. Additionally, simulations of cosmic shocks during

galaxy formation demonstrated magnetic field generation through the Biermann battery effect at levels around 10^{-20} G[50, 51] which could be elevated by the galactic dynamo to values that are observed in our current era.

The Biermann battery effect is also a source of magnetic fields in the universe through its presence in astrophysical shock waves. Shock waves are an intriguing phenomenon in astrophysics due to their occurrence and impact on numerous space and astrophysical systems. Explosive outflows, like blast waves generated by supernovae, create shocks that mix the interstellar medium[60, 49]. Shock waves also impact the evolution of supernova remnants[60, 49] and contribute to star formation[60, 1]. Shocks are also produced by accretion in galaxy clusters [99], within stellar winds [54], and at the interface between stellar winds and the interstellar medium [98].

As described by Kulsrud and Zweibel[51], the cosmological evolution of the universe cannot be fully understood without a solid knowledge of the origin, structure, and evolution of magnetic fields. These fields are difficult to detect because they are very weak (micro-Gauss) and far away[51, 76, 2, 39]. Diagnostic techniques such as Faraday rotation and Zeeman splitting are difficult to implement in such contexts[105, 41, 51]. However, laboratory astrophysics experiments that reproduce astrophysical plasmas scaled by dimensionless parameters can complement observational measurements by overcoming these limitations[78, 79]. Thus, the combination of astrophysical observations, theory, laboratory plasma experiments, and computational modeling of such scenarios helps in the pursuit of answers to questions about cosmic magnetic fields.

Dimensionless parameters allow us to compare laboratory and astrophysical systems by looking at aspects of the overall dynamics and flow of each plasma system. If the dynamics and flow are governed by similar mechanisms, we can consider the plasma systems to behave similarly and thus they can be compared. The Reynolds number is an example of a dimensionless parameter that describes if the flow of a fluid is turbulent or laminar. When the value of this number is high, the flow of the system is in a turbulent state; conversely, when the number is very small, the flow is laminar. The magnetic Reynolds number, which is the

magnetic equivalent of the Reynolds number, describes how magnetic fields are distributed through a plasma system. This number is a ratio which compares magnetic advection and diffusion within a magnetized fluid system. When the magnetic Reynolds number is high, the magnetic fields are advected with the plasma flow whereas in low values, the fields diffuse through the system. These parameters are often very large in many astrophysical scenarios. For instance, these dimensionless parameters for intergalactic medium are exceedingly large ($>> 1$). Laboratory environments can create similar conditions to these astrophysical systems[36] and give us insight into processes occurring in these systems.

Laser-produced plasma (LPP) platforms are frequently utilized to investigate astrophysically relevant plasmas and spontaneously generated magnetic fields[29, 9]. LPPs generate the density and temperature gradients required for the Biermann battery while the resulting magnetic fields play an essential role in plasma energy transportation, influencing particle dynamics[8]. They also lead to the creation of hotspots[14] and the production of fast electrons and ions[15]. In addition, these magnetic fields generate significant amounts of pressure. Biermann fields have been generated in laboratory conditions with amplitudes that range from weak (a few micro-Gauss) to very strong (mega-Gauss). These fields have a direct correlation with the intensity of laser irradiation within the range of 10^{12}-10^{14} W/cm^2.

Magnetic field generation through the Biermann battery effect has been examined in various laboratory plasma regimes[91, 75, 33, 61, 90, 29]. This phenomenon holds significance not only for cosmic fields but also for its influential role in several laboratory phenomena. Some examples of these phenomena include laser-target interactions[26], magnetic reconnection[71, 58], laboratory shocks[35, 36, 70, 69, 81, 82, 6, 101, 42, 43], and during inertial confinement fusion experiments[55, 100].

Various laboratory experiments have investigated magnetogenesis via the Biermann battery effect, examining magnetic fields within distances ranging from a few micrometers to several centimeters from the surface of the target. The magnetic fields produced were measured through various techniques such as magnetic flux probes, Faraday rotation[92, 77], Zeeman splitting[62], proton radiography[29], and harmonic polarimetry[33]. The measured fields

demonstrated azimuthally-symmetric magnetic fields with strengths ranging from 450 G to 10 MG [91, 77, 62, 75]. The study of Biermann-generated fields in the presence of background gases [4, 61, 10] revealed that elevated gas pressure results in greater Biermann-generated magnetic fields. Experiments have also shown that the strength of the field generated by Biermann scales with laser energy.[10]

Blast waves have been analyzed in lab experiments via high-power lasers to examine shock structure's temporal evolution [94], hydrodynamic instabilities [37, 23, 22], radiative effects [40], and magnetic field generation and amplification [36, 57]. Gregori et al. conducted experiments to investigate the generation of Biermann fields by laser-driven Sedov-Taylor blast waves in He background gas at 0.8 and 1.6 mbar[36]. Magnetic fields were measured with a three-axis magnetic flux probe located at distances of 2.8 and 3.6 cm from the surface of the carbon target, and reached values of 10-30 G. Researchers Gregori et al. compared experimental findings to HELIOS-CR simulations, confirming that the Biermann battery effect generated the measured magnetic fields in the blast wave front and postulated that this mechanism could have been a source of primordial magnetic seed fields[36].

The Biermann battery effect is known to be present in many plasma systems, but the study of this effect over large volumetric regions under various conditions have not been conducted. Prior experiments only studied the Biermann battery effect over short spatial and temporal ranges. We extend the previous studies to include 3-dimensional measurements over tens of cm and temporal scales up to 3 μs. In addition, the experiments described in this dissertation were performed at high repetition rate, which allowed us to obtain 1000s of data points in a matter of hours. As a result, we were able to study magnetic field generation via the Biermann battery effect with higher spatial resolution than previous work.

Simulations conducted by M. B. Adams and P. Tzeferacos identified the presence of a background gas during the recording of some of the earlier HEDP group Thomson scattering (TS) data[47]. M. B. Adams' subsequent simulations matched the TS data once background gas was introduced, and shock waves occurred. This inspired the exploration of electron temperature and density and magnetic field generation in the presence of hydrodynamic

blast waves. Experiments to study this regime have been performed in the past[36], but only a few spatial points were measured, and no measurements of electron temperature or density were made. Detailed measurements of the electron temperature and density gradients within the blast waves greatly facilitate understanding the generation of magnetic fields by Biermann battery effects in blast waves. For this purpose, we correlated 3D magnetic fields measurements and novel 2D measurements of electron temperature and density gradients within laser-driven blast waves.

In terms of simulation efforts, the Biermann term in the induction equation of magnetohydrodynamic (MHD) simulation codes has been challenging to implement[26, 34]. The unprecedented data resolution of our experiments allows for integrated validation of the implementation of the Biermann battery term in simulations. We worked with collaborators at the Flash Center at the University of Rochester to create MHD simulations for our experiments. The data were used to validate the implementation of the Biermann term[26, 34] in the FLASH code[28, 95] and, in turn, the results of the simulations were used to better understand the physics observed in the experiments.

In this dissertation, we present a series of high repletion rate experiments that investigate the generation of magnetic fields via the Biermann battery effect over large spatial regions under various conditions. In chapter 1, we present the theory underlying the Biermann battery effect and how our experiments are scaled to astrophysical systems. The experimental setup and explanations of the diagnostics used are presented in chapter 3. Experimental results can be found in chapter 4. The study of Biermann fields in vacuum conditions is presented in section 4.1, two-dimensional measurements of electron and temperature gradients in section 4.3.2, magnetic field measurements in blast waves in section 4.4. The comparison of experimental results with FLASH simulations is discussed in section 4.5, and a comparison of experimental results with astrophysical systems can be found in section 4.6. A summary, conclusions and possible future directions of this research can be found in chapter 5.

CHAPTER 2

The Biermann Battery Effect Theory

2.1 The Induction Equation

The Biermann battery effect is the spontaneous generation of magnetic fields due to non-parallel electron temperature and density gradients in a plasma. To get a physical intuition of how this effect works in general, consider a plasma ejection, such as a laser-produced plasma or a solar flare. When the plasma is created, pressure gradients naturally form. The lighter electrons move down this pressure gradient much faster than the heavier ion species, the charge separation creating an electromotive force (EMF). According to Faraday's Law, this EMF creates a magnetic field. The Biermann battery effect mathematically appears in the manetohydrodynamic (MHD) induction equation which is given by

$$\frac{\partial \vec{B}}{\partial t} = \vec{\nabla} \times (\vec{v} \times \vec{B}) + \frac{\eta c^2}{4\pi} \nabla^2 \vec{B} - \frac{1}{en_e} \vec{\nabla} \times (\vec{J} \times \vec{B}) + \frac{c}{en_e} \vec{\nabla} T_e \times \vec{\nabla} n_e \tag{2.1}$$

where $\vec{B}$ is magnetic field, $\vec{v}$ is electron velocity, η is the plasma resistivity, c is the speed of light, e is the charge of an electron, n_e is electron density, $\vec{J}$ is current density, and T_e is electron temperature. The first term on the right-hand side of equation 2.1 describes the magnetic induction (or advection) in the plasma, the second term denotes the diffusion of the magnetic field with respect to the plasma, the third term describes the redistribution of the magnetic fields due to the Hall effect, and the fourth term is the magnetic source term, known as the Biermann battery term. Note that the Biermann term is the only term in the induction equation that explicitly depends on the plasma properties. This term is also the only term in equation 2.1 that does not depend on the magnetic field or the plasma flow

($\vec{u}$). Thus, when the magnetic fields in the plasma are very small, this term will dominate magnetic field evolution.

2.2 MHD Treatment of the Biermann Battery Effect

Ideal MHD describes the interaction between electromagnetic fields and conducting fluids without viscosity, resistivity, or thermal conductivity. It is an approximation that holds when charge separation effects are negligible and it is valid only on length scales larger than Debye length and electron/ion gyroradii, and on time scales much longer than the inverse of the electron/ion gyro-frequencies. Many astrophysical plasmas and extremely hot, strongly magnetized plasmas can be reasonably described by MHD models.

In an ideal MHD approach, four main assumptions come into play: a) the electromagnetic fields in the system are of low frequency, which allows us to ignore relativistic effects ($v^2/c^2 << 1$), and the displacement current in the system simplifies to Ampere's law; b) the plasma is quasi-neutral, $\varrho = 0$, where $\varrho = \varrho_e + \varrho_i$; c) collisions in the plasma are frequent enough that the distribution function is Maxwellian; d) the plasma equation of state is adiabatic and that there is no additional heating or dissipation. These assumptions lead to the following ideal MHD equations (in CGS units):

$$\frac{\partial \rho}{\partial t} + \nabla \cdot (\rho \vec{u}) = 0 \tag{2.2}$$

$$\frac{\partial \vec{u}}{\partial t} + \nabla \cdot (\rho \vec{u}\vec{u}) = \frac{1}{c}\vec{J} \times \vec{B} - \nabla P \tag{2.3}$$

$$\frac{d}{dt}(\frac{P}{\rho^\gamma}) = 0 \tag{2.4}$$

$$\vec{J} = \frac{c}{4\pi}\nabla \times \vec{B} \tag{2.5}$$

$$\frac{\partial \vec{B}}{\partial t} = \nabla \times (\vec{u} \times \vec{B}) \tag{2.6}$$

where ρ is the density, $\vec{u}$ is the velocity, $\vec{J}$ is the current density, $\vec{B}$ is the magnetic field, P is the pressure, γ is the adiabatic index ($\gamma = 5/3$), and c is the speed of light. The equation 2.2 is a scalar equation describing the evolution of the total mass density in a plasma. Equation 2.3 describes the conservation of vectorial momentum. Equation 2.4 is the scalar conservation equation. Equation 2.5 is commonly known as Ampere's Law. Finally, the equation 2.6 is the induction equation.

An important consequence of the MHD equations is the "frozen-in" condition (Alfvén theorem). This condition states that, in the limit of large magnetic Reynolds numbers, the magnetic flux through any closed loop moving with the fluid remains constant. Mathematically, this is described as

$$\frac{d\Psi}{dt} = -\oint (\vec{E} + \frac{1}{c}\vec{u} \times \vec{B}) \cdot d\vec{l} = 0 \tag{2.7}$$

In ideal MHD, we additionally have the condition that $E + \frac{1}{c}u \times B = 0$, making the frozen-in condition trivial so the magnetic fields moves with the plasma, preserving the magnetic field topology. Although this framework is good for approximations in astrophysical settings, it needs to be extended to include additional terms, such as resistivity and viscosity, to describe laboratory plasma systems. In our experiments, the main interest is magnetic field generation, and thus the dynamics of the plasma will be described using the generalized Ohm's law.

To obtain generalized Ohm's law, we will consider a quasineutral plasma with singly charged ions. We can then define the mass density ρ, the mass velocity $\vec{v}$, and the current density $\vec{J}$ as:

$$\rho = n_i M = n_e m = n(M + m) \tag{2.8}$$

$$\vec{v} = \frac{1}{\rho}(n_i M\vec{v_i} + n_e m\vec{v_e}) \approx \frac{M\vec{v_i} + m\vec{v_e}}{M+m} \tag{2.9}$$

$$\vec{J} = e(n_i\vec{v_i} - n_e\vec{v_e}) \approx ne(\vec{v_i} - \vec{v_e}) \tag{2.10}$$

We will assume that the Larmor radius is much smaller than the length scale of the system and thus neglect the viscosity tensor. With the above definitions and assumptions in mind, we can write the electron and ion fluid equations as

$$Mn\frac{\partial\vec{v_i}}{\partial t} = en(\vec{E} + \frac{1}{c}\vec{v_i}\times\vec{B}) - \nabla P_i + Mng + K_{ie} \tag{2.11}$$

$$mn\frac{\partial\vec{v_e}}{\partial t} = -en(\vec{E} + \frac{1}{c}\vec{v_e}\times\vec{B}) - \nabla P_e + mng - K_{ei} \tag{2.12}$$

where g is the acceleration due to gravity and K_ie and K_ie are the collision terms and $K_{ei} = -K_{ie}$. Here we have also assumed that the velocity of the electrons and ions is small, so that the quadratic velocity terms can be neglected. By multiplying the equation 2.11 by m and the equation 2.12 by M, and then subtracting the equation 2.12 from 2.11, we obtain

$$Mmn\frac{\partial}{\partial t}(\vec{v_i}-\vec{v_e}) = en(M+m)\vec{E}+\frac{en}{c}(m\vec{v_i}+M\vec{v_e})\times\vec{B}-m\nabla P_i+M\nabla P_e-(M+m)K_ei \tag{2.13}$$

Using the definitions given in equations 2.8 and 2.10, and noting that the collision term is given by $K_{ei} = \eta e^2 n^2(\vec{v_i} - \vec{v_e})$, where η is the resistivity of the plasma, our equation becomes

$$\frac{Mmn}{e}\frac{\partial}{\partial t}\left(\frac{\vec{J}}{n}\right) = e\rho\vec{E} - en\eta(M+m)\vec{J} - m\nabla P_i + M\nabla P_e + \frac{en}{c}(m\vec{v_i} + M\vec{v_e})\times\vec{B} \tag{2.14}$$

Using the definitions in the equations 2.8, 2.10 and a little algebra, we can further simplify the last term

$$(m\vec{v_i} + M\vec{v_e}) = (M\vec{v_i} + m\vec{v_e}) + M(v_e \vec{-} v_i) + m(v_i \vec{-} v_e) = \frac{\rho}{n}\vec{v} - (M-m)\frac{\vec{J}}{ne} \tag{2.15}$$

We now divide by equation 2.14 by $e\rho = en(M+m)$ and rearrange the terms to obtain

$$\vec{E} + \frac{1}{c}\vec{v} \times \vec{B} - \eta\vec{J} = \frac{1}{en(M+n)}\left[\frac{Mmn}{ce}\frac{\partial}{\partial t}\left(\frac{\vec{J}}{n}\right) + \frac{(M-m)}{c}\vec{J} \times \vec{B} + m\nabla P_i - M\nabla P_e\right] \tag{2.16}$$

By assuming that inertial effects, i.e. cyclotron motion, are negligible, we can ignore the $\partial/\partial t$ term. Taking the limit where $m << M$, or in other words $m/M \to 0$, and rearranging, we have

$$E + \frac{1}{c}(\vec{v} \times \vec{B}) = \eta\vec{J} + \frac{1}{cen}(\vec{J} \times \vec{B}) - \frac{1}{en}\nabla P_e \tag{2.17}$$

Equation 2.17 is the generalized Ohm's law. Note that the frozen-in condition in equation 2.7 now no longer applies since $E + \frac{1}{c}(\vec{v} \times \vec{B}) \neq 0$ and plasma can now move across magnetic field lines.

To describe the evolution of the magnetic field in a plasma over time, we combine the Faraday's law of induction, $\frac{\partial \vec{B}}{\partial t} = -c\nabla \times \vec{E}$ and the generalized Ohm's law in equation 2.17.

$$\frac{\partial B}{\partial t} = -c\nabla \times \left(-\frac{1}{c}(\vec{v} \times \vec{B}) + \eta\vec{J} + \frac{1}{cen_e}(\vec{J} \times \vec{B}) - \frac{1}{en}\nabla P_e\right) \tag{2.18}$$

One of the assumptions we make is that the equation of state of the plasma is adiabatic and thus follows the ideal gas law. This allows us to express the electron pressure as the product of electron density and temperature, $P_e = n_e T_e$. Additionally, we can express the current density in terms of the magnetic field, $\nabla \times \vec{B} = \frac{4\pi}{c}\vec{J}$. Plugging this into the equation 2.18 and simplifying, the induction equation becomes

$$\frac{\partial \vec{B}}{\partial t} = \vec{\nabla} \times (\vec{v} \times \vec{B}) + \frac{\eta c^2}{4\pi}\nabla^2\vec{B} - \frac{1}{en_e}\vec{\nabla} \times (\vec{J} \times \vec{B}) + \frac{c}{en_e}\vec{\nabla}T_e \times \vec{\nabla}n_e \tag{2.19}$$

This form allows us to see the dependence of the time evolution of the magnetic field in terms of electron temperature and density. Note that the Biermann term is the only term in the induction equation that explicitly depends on the plasma parameters, and does not

depend on the plasma flow ($\vec{u}$) nor on magnetic field. Thus, when the magnetic fields in the plasma are very small, this term will dominate magnetic field evolution.

2.3 Laser Produced Plasmas

When a laser hits the surface of a target, the high electric fields of the laser cause the electrons in the target to vibrate, resulting in heating and vaporization and, if intense enough, direct ejection of the target material[87, 88]. The plasma created is highly collisional and isothermal, and the initial temperature of the plasma is determined by the laser-target interaction[87]. If the plasma density is high enough, the plasma can also be heated by direct absorption of laser energy through an inverse Bremmstrahlung radiation process[65]. As the plasma expands, the density rapidly decreases and the ablated plasma is transparent to the laser everywhere except directly adjacent to the target surface where a high density of ions are produced during the laser pulse[87]. This leads to a dynamic equilibrium in which the high-density plasma near the target surface absorbs laser energy, causing less material to be vaporized, lowering the plasma density and restarting the process. The thermal energy gained in the region near the target surface is rapidly converted to kinetic energy as the plasma expands[87].

In the experiments discussed, the duration of the laser pulse (15-20 ns) was much shorter than the dynamics of interest. Thus, the LPP production was considered instantaneous and can be modeled as a hot, highly confined gas. Pressure gradients in the gas cause rapid expansion of the LPP mainly in the direction perpendicular to the target surface, resulting in an ellipsoidal plasma. When the plasma is generated in a vacuum environment, the expansion can be considered adiabatic because the plasma cannot exchange energy with its surroundings. When the plasma expands into a background gas at sufficient pressure, shock waves are formed and the expansion is no longer adiabatic[102].

When an LPP expands into a vacuum environment, the primary temperature gradient is perpendicular to the axis of the plasma plume and the primary density gradient is normal

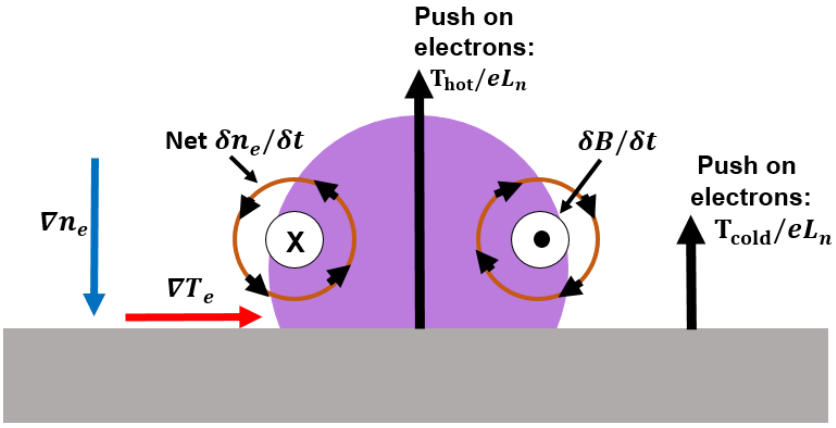

Figure 2.1: Conceptual diagram of how the Biermann battery effect occurs in laser produced plasmas. The push on the electrons is denoted by the black arrows, once the plasma is created from the laser target interaction electrons are pushed away from the target. The electron density gradient is denoted by the blue arrow and the electron temperature gradient is denoted by the red arrow. The non-parallel temperature and density gradients cause a net change in electron density over time, denoted by the brown circles. This then causes magnetic fields, the direction from this perspective is into and out of the board as denoted by the white circles.

to the target surface (with higher density closer to the target). This generates azimuthal magnetic fields with respect to the blow-off axis of the plasma[38]. A conceptual diagram of the Biermann battery process and a cartoon representation of the Biermann generated magnetic fields in our experimental system are shown in Figure 2.1.

Mathematically, the source term in cylindrical coordinates is given by:

$$\vec{B}_{source} = -\frac{c}{en_e}\left(\frac{\partial T_e}{\partial r}\frac{\partial n_e}{\partial z} - \frac{\partial T_e}{\partial z}\frac{\partial n_e}{\partial r}\right)\hat{\theta}, \tag{2.20}$$

where $\hat{\theta}$ is the azimuthal unit vector. Note that in a cylindrical framework, $r = \sqrt{x^2 + y^2}$ is the radial coordinate, and z is the axial coordinate. Thus the gradients in the radial and

axial directions for the electron temperature and density are crucial to our understanding of Biermann fields generated in the LPP context.

2.4 Scaling to Astrophysics

Laser-produced plasmas are an essential tool in the laboratory astrophysics framework, offering the much needed ability to reproduce various astrophysical processes and test theories related to the physics driving those processes. Although the length and time scales over which laboratory experiments occur are much smaller, we are able to compare these two regimes through the use of dimensionless parameters[11]. Among the most employed parameters that make the laboratory experiments relevant to astrophysical events are the Reynolds number, the magnetic Reynolds number, and the Prandtl number[11, 50, 36].

The Reynolds number is a dimensionless parameter that represents the ratio of inertial forces to viscous forces in a fluid undergoing relative inertial motion due to different fluid velocities. Because this number quantifies the relative importance of inertial and viscous forces in a fluid, it can be used to determine whether turbulent flow is occurring in a system.

The Reynolds number can be derived in a number of ways, but here we will use the non-dimensional form of the Navier-Stokes equations for a Newtonian fluid. This equation in terms of the Lagrangian derivative is given by

$$\rho \frac{D\vec{v}}{Dt} = -\nabla p + \mu \nabla^2 \vec{v} + \rho \vec{f} \tag{2.21}$$

where ρ is the fluid density, μ is the dynamic viscosity of the fluid, p is pressure and $\vec{v}$ is fluid velocity, and $\vec{f}$ is body force. All terms in this equation have units of force per unit volume, which means that each term depends on the exact measurement of a flow. In order to arrive at a parameter with no dimensions, we multiply this equation by a factor with inverse units. For our purposes, we will multiply by a factor of

$$\frac{L}{\rho V^2} \tag{2.22}$$

where L is the characteristic length scale and V is the mean velocity. We also define the following parameters

$$\vec{v'} = \frac{\vec{v}}{V},\ p' = p\frac{1}{\rho V^2},\ \vec{f'} = \vec{f}\frac{L}{V^2},\ \frac{\partial}{\partial t'} = \frac{L}{V}\frac{\partial}{\partial t},\ \nabla' = L\nabla \tag{2.23}$$

Using these, we can now write equation 2.21 as

$$\frac{D\vec{v'}}{Dt'} = -\nabla' p' + \frac{1}{R_e}\nabla'^2\vec{v'} + \vec{f'} \tag{2.24}$$

Where the Reynolds number, R_e, is defined as

$$R_e = \frac{LV}{\mu} \tag{2.25}$$

with the viscosity, μ, given by

$$\mu = 1.92 \times 10^{19}\frac{T_i^{5/2}}{A^{1/2}Z^4 n_i ln\Lambda}\ cm^2 s^{-1} \tag{2.26}$$

where T_i is the ion temperature, n_i is the ion density, A is the average atomic weight, Z is the average ionization and $ln\Lambda$ is the Coulomb logarithm: $ln\Lambda = 23.5 - ln(n_e^{1/2}T_e^{5/4}) - \sqrt{10^{-5} + (ln(T_e) - 2)^2/16}$

The Reynolds number determines whether the fluid is in a laminar or turbulent flow regime. When the Reynolds number is small, $R_e << 1$, the fluid is in the laminar flow regime where viscous forces dominate. In this regime, the flow is characterized by smooth and constant fluid motion. On the other hand, if the Reynolds number is large, $R_e >> 1$, the fluid is in the turbulent regime. In the turbulent regime, inertial forces dominate and flow instabilities and turbulence occur.

The magnetic Reynolds number is the magnetic analog of the Reynolds number. It is a dimensionless parameter used to estimate the relative effects of advection of a magnetic field through a plasma and magnetic diffusion in a plasma. The magnetic Reynolds number is derived from the induction equation. The first term on the right hand side of equation 2.19 is the magnetic induction or advection term and the second term is the magnetic diffusion term. The relative effects of these terms can be found by taking the ratio of them. Assuming

that both of these terms have the same scale velocity, V, where $\vec{v} = V$ and the same length scale, L, where $\nabla \approx 1/L$ we can write the induction term as

$$\nabla \times (\vec{v} \times \vec{B}) \approx \frac{V\vec{B}}{L} \tag{2.27}$$

and we can write the diffusion term as

$$\eta \nabla^2 \vec{B} \approx \frac{\eta \vec{B}}{L^2} \tag{2.28}$$

We now take the ration of these terms to obtain the magnetic Reynolds number

$$R_m = \frac{VL}{\eta} \tag{2.29}$$

Magnetic resistivity η is given by:

$$\eta = 3.2 \times 10^5 cm^2 s^{-1} \frac{Zln\Lambda}{T^{3/2}} \tag{2.30}$$

When the magnetic Reynolds number is large, $R_m >> 1$, advection is dominant and magnetic fields are advected with the plasma flow. On the other hand, when the magnetic Reynolds number is small, $R_m << 1$, advection plays little or no role in the plasma and the magnetic fields are diffused through the plasma. When the magnetic fields are diffusing through a plasma, the motion of the fields is determined by the boundary conditions of the plasma rather than by flow as in the advective regime.

The momentum or viscous diffusivity and the magnetic diffusivity within a plasma can be compared using the magnetic Prandtl number. As we stated earlier, the Reynolds number compares inertial forces to viscous forces and the magnetic Reynolds number compares magnetic advection to magnetic diffusion. Thus, the Prandtl number which compare viscous diffusion and magnetic diffusion is the ratio of the magnetic Reynolds number and the Reynolds number.

$$P_m = \frac{viscous\ diffusion}{magnetic\ diffusion} = \frac{\nu}{\eta} = \frac{R_m}{R_e} \tag{2.31}$$

When this number is large, the viscous diffusion dominates and when this number is small, magnetic diffusion dominates. The equations for μ, η and $ln\Lambda$ are from Tzeferacos et al[96].

Generally, astrophysical systems have very large R_e and R_m. For example, our galaxy has a magnetic Reynolds number estimated to be $R_m \approx 10^{19}$[51]. Other examples include Interstellar medium (ISM) with a Reynolds number of $R_e \approx 10^8$ and a magnetic Reynolds number of $R_m \approx 10^{19}$[11] and Stellar atmospheres with $R_e \approx 5 \times 10^{12}$ and $R_m \approx 4 \times 10^9$[11]. The magnetic Prandtl number, however, varies depending on the astrophysical system. Looking at our two examples of ISM and stellar atmospheres, we see very different numbers. For ISM $P_m \approx 10^{12}$ where as for stellar atmospheres, $P_m \approx 8 \times 10^{-4}$.

CHAPTER 3

Experimental Design

All experiments were conducted in a one meter diameter stainless steel cylindrical vacuum chamber. A three-axis Velmex stepper motor drive assembly was mounted inside the chamber to allow probe mounting and scanning over large spatial regions in the chamber at a repetition rate of 1 Hz. The full spatial scanning capability of the 3D motor drive setup is $[-7, -63]$ mm in the x direction, $[7, 139]$ mm in the y direction, and $[-85, 85]$ mm in the z direction, with the laser spot representing the origin of the coordinate system. LPPs were generated by irradiating a 25 mm diameter cylindrical high density polyethylene (C_2H_4) target with a pulsed high energy heater beam at an angle of incidence of 34 degrees with respect to the target surface normal. The target was rotated and vertically translated in a helical pattern to ensure there is a new and unused target surface for each shot. Five shots were taken at each spatial position for data averaging to account for shot-to-shot variations in laser energy ($2 - 5\%$ per shot).

To observe in great detail the structure and evolution of the Biermann generated fields we employed the magnetic flux probes described in Section 3.2, as well as a self-imaging diagnostic (Section 3.3). For investigating the effects created by the density and temperature gradients on the Biermann magnetism we developed a 1 Hz raster Thomson scattering diagnostic (Section 3.4) probing the laser plasma in vacuum and in either nitrogen (N_2) or helium (He) background gases, at various pressures between 25-1000 mTorr. Dynamically monitoring the pressure changes in the chamber during the 1 Hz runs is important for data comparison between different conditions in the background ambient. Therefore the pressure inside the chamber was measured for all experiments using two separate pressure sensors.

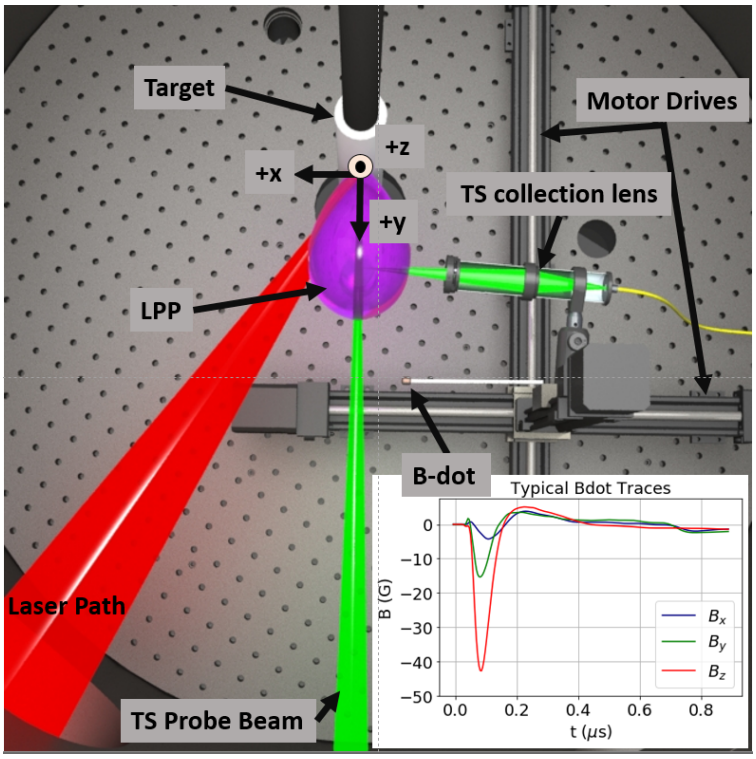

Figure 3.1: A rendering of the experimental setup used for the Biermann field measurements. **a)** Top view. The origin of the coordinate system is the laser spot on the target, with the corresponding axis directions as shown. **b)** Typical B-dot probe traces for all three axes of the probe.

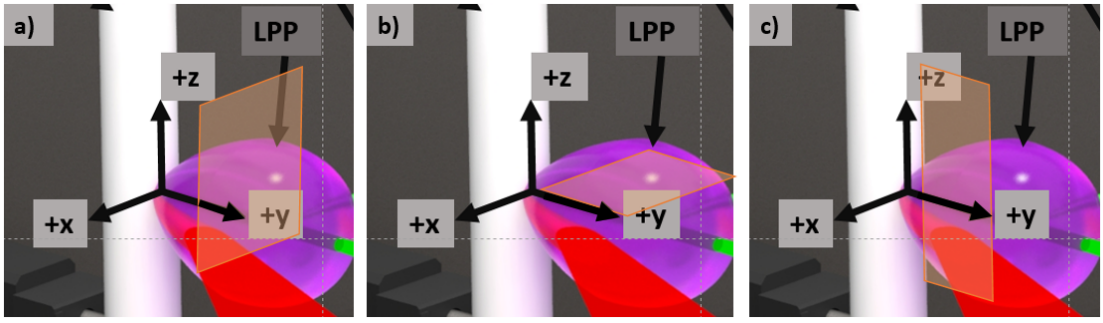

Figure 3.2: Orientation of data planes (translucent orange planes) with respect to the laser path and LPP blow-off axis (+y-axis). **a)** Representation of an XZ plane which is perpendicular to the y-axis. **b)** Representation of an XY plane which is perpendicular to the z-axis. **c)** Representation of a YZ plane which is perpendicular to the x-axis.

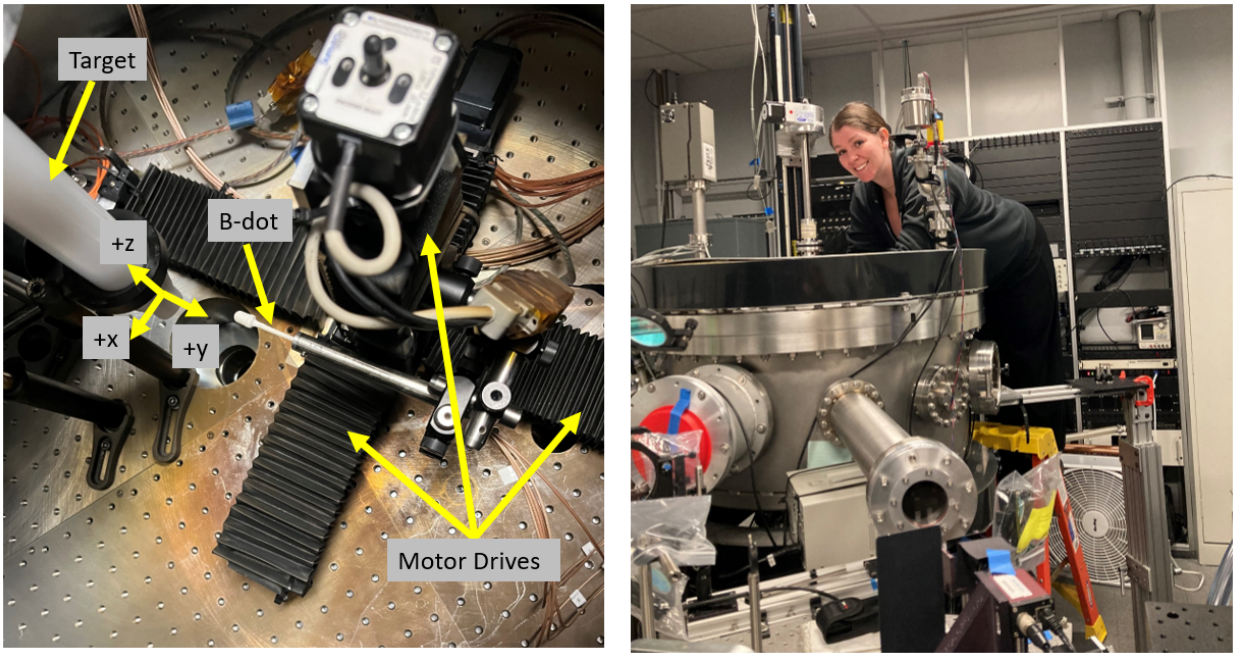

Figure 3.3: **Left:** Top down picture of the inside of the experimental vacuum chamber. The B-dot in this image is mounted along the y-axes, this positioning was used during blast wave experiments. The motor drives are covered with custom designed bellows to protect them from LPP debris. **Right**: Image of outside of experimental chamber as I am working inside the chamber.

A top down schematic of the experimental set up with the magnetic flux probe mounting for the vacuum experiments and representative magnetic flux probe traces is shown in figure 3.1. A picture of the inside of the vacuum chamber including the magnetic flux probe mounting for the blast wave experiments and custom bellows for the motor drives is shown in figure 3.3.

3.1 Heater Beam

Laser produced plasmas (LPP) were created via the Peening laser at the UCLA Phoenix Laser Laboratory [68]. The Peening laser is a high-energy (up to 20 J), pulsed (in these experiments, 15 ns or 20 ns pulse duration at FWHM), and high-repetition rate system

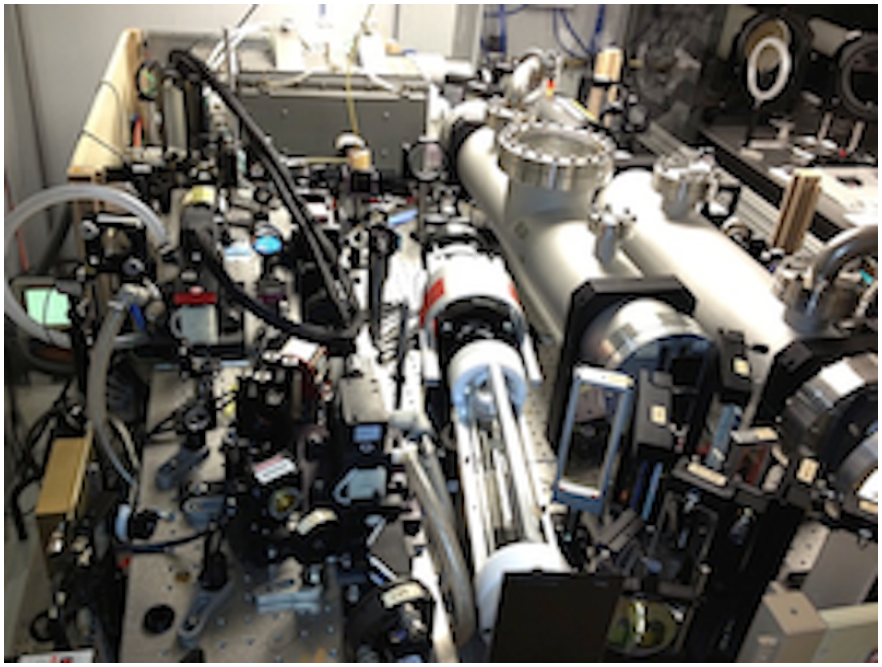

Figure 3.4: Overview of the high-energy, high-repetition rate Peening laser system, in the PHOENIX Laser Laboratory at UCLA.

(1-6 Hz) [17]. The nominal wavelength is 1053 nm, obtained in a ring cavity through an electronic line-width narrowing technique (by using single mode selective elements in the Q-switched cavity, such as a pair of etalons). The system builds up the energy in an eight-pass amplification scheme, with a phase-conjugation technique after the fourth pass, in order to correct the wavefront distortions caused by the thermally induced birefringence effects in the amplifier. For this purpose, a pairs of cells filled with fluorinert FC-72 is used to produce a stimulated Brillouin scattering process through which every ray in the beam is back-scattered. The result is a near-diffraction limited beam profile. In the process, the pulse suffers a steepening of the rising edge and a slight shortening of the beam (< 1 ns).

To match the rectangular amplifier slab (20x1 cm), the round beam delivered by the front-end is passed through an anamorphic telescope which stretches one dimension of the beam to match the slab dimensions. Farther on in the system, a mask is used to give the beam a final square shape of 4x4 cm dimensions at the output. An image of the Peening laser is shown in figure 3.4.

All laser, target, and diagnostics controls, as well as data acquisition are based on a custom LabView-based program, which enables the automatic synchronization of all systems, at 1 Hz repetition rate.

In the experiments presented hereby, the Peening laser beam was passed into the vacuum chamber through an infra-red anti-reflective coated window and guided onto a cylindrical graphite target at an incidence angle of 34 degrees, creating an LPP which expanded perpendicular to the target surface, along the +y axis (see figure 3.2). The laser energy was 10 J with a pulse width of 15 ns for the vacuum experiments and 20 ns for the shock wave experiments. The beam was focused to a 250 μm diameter spot onto the target by a f/25 lens, resulting in $I \approx 10^{12}\ W/cm^2$ intensity.

3.2 Magnetic Flux Probes

Magnetic flux measurements were collected using a three-axis magnetic flux ("B-dot") probe mounted on the 3D motor system. The B-dot probe consists of three sets of thin wire coils wound around three perpendicular axes. When a magnetic flux passes through the wire coils in the probe, a voltage proportional to $d\vec{B}$ is produced in the coil. This signal is amplified, numerically integrated, and multiplied by a calibration factor to obtain $\Delta\vec{B}$. A static electric field can also induce a voltage in the coil, but this effect is removed by winding each coil with a pair of wires (differential winding) and subtracting the result using a differential amplifier to remove electrostatic components. After passing through the differential amplifier, the voltage is recorded by a digitizer (250 MSamples/s, 125 MHz bandwidth, 12 bit), which recorded signals for 3.5 μs after the heater beam was fired.

The design and construction of the probes used in this experiment are very similar to the probes described by Everson et. al. [25]. A complete guide to building the B-dot probes used in this experiment can be found in the Appendix A.

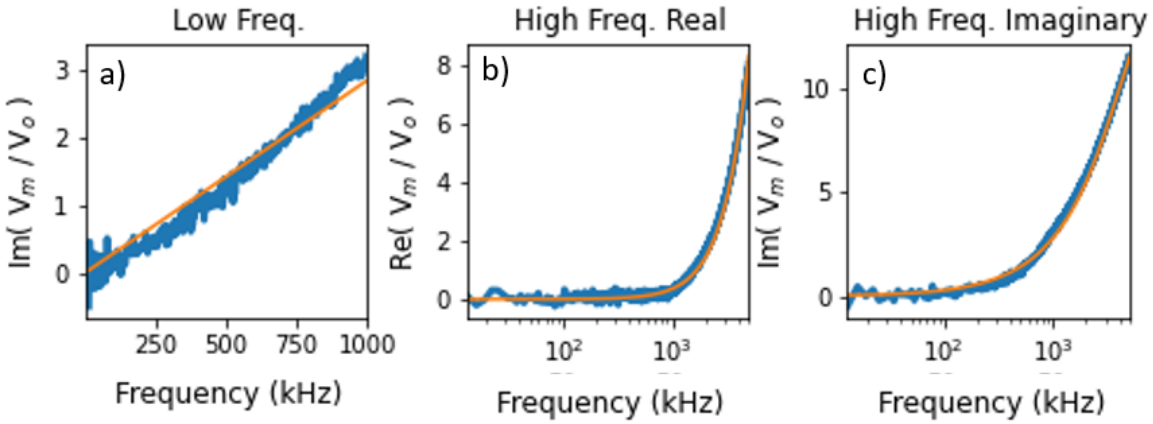

Figure 3.5: Frequency response of a 3 mm B-dot probe in the calibration Helmholtz coil (blue) and the fits used to determine the calibration factors (orange). **a)** Linear fit in the low frequency range used to determine the area of the probe axis. **b)** Real part of the probe's high frequency response. **c)** Imaginary part of the probe's high frequency response. The fits from b and c are used to determine the inductance constant τ_s.

3.2.1 Magnetic Flux Probe Calibration

Magnetic flux probes are calibrated using a well-characterized magnetic field generated by a Helmholtz coil driven between frequencies of 10 kHz - several MHz. The drive current and the induced voltage on the probe are recorded using a network analyzer. The first axis calibrated was the one pointing along the probe shaft. The wires associated with this axis were connected to the network analyzer through a custom 100 MHz differential amplifier. The probe was placed in the center of the Helmholtz coil with the magnetic field pointing in the positive direction along the shaft. The probe was also tested with the field pointing along the other two axes to ensure that there was little or no cross-talk between the axes. This process is repeated for the other two axes with the magnetic field pointing in the direction associated with the axes to be calibrated.

The resulting signals can be used to find the probe area in two ways. The first is by using

the following equation

$$a = \frac{10^{A/20} \times r}{n_H \times \frac{4}{5}^{1.5} \times \mu_o \times N \times g \times \omega} \tag{3.1}$$

where a is the area of the probe axis, A is the magnitude of the signal along the axis in dB, r is the radius of the Helmholtz coil in meters, N is the number of turns in the B-dot, g is the gain of the differential amplifier and ω is the angular frequency provided by the network analyzer.

The second method is to apply fit functions to the frequency response of the probe. The theoretical response of the probe to the magnetic field is[25]:

$$\frac{V_{measured}}{V_{Helmholtz}} = \frac{4}{5}^{3/2} \frac{\mu_o n_H a n_b g}{r_H R_p} \frac{\omega}{1 + (\omega\tau_s)^2} (\omega\tau_s + i) e^{i\omega\tau} \tag{3.2}$$

where n_H is the number of turns in the Helmholtz coil, a is the area of a coil, n_b is the number of turns in the probe, g is the amplifier gain, r_H is the radius of the Helmholtz coil, R_p is the resistance of the coil, ω is the frequency, τ_s is the time constant associated with the RL circuit of the internal B-dot coils, and τ is the cable time delay. For our purposes, we are only concerned with the low frequency limit ($\omega\tau_s << 1$), so the equation becomes

$$\frac{V_{measured}}{V_{Helmholtz}} = \frac{4}{5}^{3/2} \frac{\mu_o n_H a n_b g}{r_H R_p} [\omega^2(\tau_s - \tau) + i\omega]. \tag{3.3}$$

In this limit, the imaginary part of the above equation is independent of induction effects. Therefore, the imaginary parts can be fit to determine the coil area, as shown in Figure 3.5a. Once the area is known, the signals can be fit over the full frequency range to determine τ_s, as shown in Figure 3.5b&c.

3.2.2 Voltage conversion to magnetic field

The recorded voltage signals were integrated to obtain magnetic field measurements using the following integration method described by Everson et al. [25]:

$$\vec{B} = \frac{A}{a n_b g} \left[\int \vec{V}_{measured}(t) dt + \tau_s \vec{V}_{measured}(t) + \vec{V}_o \right] + \vec{B}_o \tag{3.4}$$

where $g = 10$ is the gain of the amplifier, A is the attenuation factor which varies with signal strength, $n_b = 10$ is the number of turns in the coils, a is the area of the B-dot coils determined by calibration, $\vec{B_o} = 0$ is the initial background field, V_0 is the previously subtracted background noise, and τ_s is the time constant associated with the RL circuit formed by the coils ($\tau \approx 30\ ns$). The error of the resulting magnetic fields was calculated using the standard deviation of the five shots taken at each spatial position.

Extensive volumetric scans consisting of thousands of shots were created by moving the probe in predefined 3D patterns at a rate of 1 Hz. The closest distance to the target for the B-dot probe when mounted along the x-axis was 7 mm. When mounted along the y-axis, the closest distance was 11 mm. In both instances, minimal distance to the target surface was limited by the proximity to the laser path.

For the vacuum Biermann scans, to better observe the azimuthal structure of the Biermann generated fields, the scans focused on planes perpendicular to the plasma blow-off axis. By combining many of these perpendicular planes, three-dimensional insights of the measured Biermann fields could be obtained. In these experiments, data were collected at the same x and z points in planes at different distances from the target surface along the plasma blow-off axis (y-axis). The experimental setup for magnetic flux scanning is shown in figure 3.1.

Magnetic field measurements were also made in 95 mTorr of the N_2 background gas. For these scans, the B-dot probe was aligned along the blow-off axis to reduce the amount of probe perturbation of the laser-driven blast waves. Data were acquired in the xy, xz, and yz planes with 2 mm steps between spatial points. Depictions of the data planes are shown in figure 3.2.

3.3 Self-emission Imaging

Self-emission images of the LPP and generated hydrodynamic shock waves were captured using an Intensified Charged Couple Device (ICCD) camera. The camera was mounted

outside the chamber on a window flange. The field of view of the camera was along the x-axis pointing in the +x direction spanning 136×136 mm. Images were recorded in the yz plane. The LPP is axially symmetric, so these yz images can be used for comparison with Thomson scattering data in the xy plane and magnetic field data along the xy or yz plane.

The chamber was pumped down to vacuum ($\approx$ 0.02 mTorr) and then filled with either N_2 or He gas, at various pressures ranging from 25 mTorr to 10 Torr. For all pressures except 10 Torr, an adjustable flow valve was used to allow continuous vacuum pumping and background gas filling to maintain a constant background gas pressure. Self-emission images were acquired with an exposure time of 3 ns at various delay times ranging from 30-800 ns after the heating beam was fired. For each time delay, five to ten images were recorded for averaging.

The ICCD camera used to acquire the self-emission images was a PI-MAX4:1024f from Teledyne Princeton Instruments. The camera has an e2v CCD 47-10 scientific grade full frame CCD with 1024×1024 imaging pixels, where each pixel is 13×13 μm. The intensifier is an 18 mm Gen II and is coupled to the CCD via a 1:1 fiber optic cable. This CCD is capable of capturing images at wavelengths between 100-900 nm and can run at a sustained repetition rate of up to 1 MHz. Our images were captured within the visible spectrum at a repetition rate of 1 Hz and exposure time of 4 ns. More information about the PI-MAX4:1024f can be found at https://www.princetoninstruments.com/products/pi-max-family/pi-max.

3.4 Optical Thomson Scattering

Thomson scattering (TS) is a common diagnostic tool in plasma physics used to determine the electron temperature and pressure within a plasma. The technique uses a probe laser beam that is scattered by the electrons in the plasma. The light is then focused onto a spectrometer with a notch filter blocking the probe laser wavelength, and the resulting spectrum is detected by a CCD camera. The total intensity of the spectrum corresponds to the electron density, n_e, and the Doppler shift in the spectrum corresponds to the electron

temperature, T_e.

Due to the difficulty of laser alignment in experimental systems, TS measurements are typically made at a single point or a few points along a line in the system[24]. Previous experiments by Kaloyan et al[47] in our laboratory perfected a method in which the probe beam and collecting lens are simultaneously translated horizontally, resulting in TS measurements along multiple lines within the system without the need for laser realignment. By substituting a higher power laser, we have extended this experimental setup to enable the collection of the first 2D TS data planes.

3.4.1 Scattering from electrons

To understand Thomson scattering, we need to understand the scattering of a laser beam from multiple electrons. There are many resources that cover the theory of scattering of lasers off electrons such as:[86, 24, 18, 89]. An abbreviated version of the derivations found in the listed resources will be provided here. It is assumed that the velocity of the electrons is $v << c$, and thus they are not treated relativistically. Due to the much higher mass of ions, the scattering from ions is ignored. We consider a plasma with N electrons and N/Z ions with a total charge of Z_e in a volume of V. With these considerations, the total scattered electric field is given by the vector sum of the individually scattered fields

$$\vec{E_s^T}(\vec{r},t) = \sum_{n=1}^{N} \vec{E_{s,n}}(\vec{r},t) \tag{3.5}$$

with each individual electric field has the form

$$\vec{E_s}(\vec{r},t) = \frac{q^2}{m_e c^2 r}[\hat{s} \times (\hat{s} \times \vec{E_{i0}})]cos(k_s r - \omega_s t - \vec{k} \cdot r(\vec{0})) \tag{3.6}$$

where q is the charge of the scattered particle, m_e is the mass of an electron, c is the speed of light, $\hat{s}$ is a unit vector pointing from the charge to the observer, $k_s = \omega_s/c\hat{s}$ and ω_s are the Doppler-shifted wavenumber and frequency, respectively, and $\vec{k} = \vec{k_s} - \vec{k_i}$ is the wavenumber. Each field is identical up to a phase that depends on the motion of each electron. So the total scattered power is

$$\frac{dP_s}{d\Omega} \propto |\vec{E_s^T}|^2 = \sum_{n=1}^{N} \vec{E_{s,n}}(\vec{r},t) \cdot \sum_{m=1}^{N} \vec{E_{s,m}}^*(\vec{r},t) \tag{3.7}$$

When the electrons in the plasma are randomly distributed ($n = m$), the phases of the scattered fields cancel out on average, so that the total scattered power is the sum of the individual electron motions, which is simply the electron velocity distribution function. This type of scattering is called non-collective scattering. When the motion of the electrons and the scattered waves are correlated, the phases do not cancel ($n \neq m$) and the scattered power depends on both the individual electron motion and the wave motion. This is called collective scattering. The effect of the electron motion on the scattered power is described by the spectral density function, given by

$$S(\vec{k},\omega) = \frac{2\pi}{k} \left|1 - \frac{\chi_e}{\epsilon}\right|^2 f_{e0}(\omega/k) + \frac{2\pi Z}{k} \left|\frac{\chi_e}{\epsilon}\right|^2 f_{i,0}(\omega/k) \tag{3.8}$$

where f_i and f_e are the ion and electron velocity distribution functions, respectively, χ_e and χ_i are the electron and ion susceptibilities, respectively, and ϵ is the dielectric function. These are given by:

$$\chi_e(\vec{k}\omega) = \frac{4\pi e^2 n_{e0}}{m_e k^2} \int_{-\infty}^{\infty} d\vec{v} \frac{\vec{k} \cdot df_{e0}/d\vec{v}}{\omega - \vec{k} \cdot \vec{v} - i\gamma} \tag{3.9}$$

$$\chi_i(\vec{k}\omega) = \frac{4\pi Z e^2 n_{i0}}{m_i k^2} \int_{-\infty}^{\infty} d\vec{v} \frac{\vec{k} \cdot df_{i0}/d\vec{v}}{\omega - \vec{k} \cdot \vec{v} - i\gamma} \tag{3.10}$$

$$\epsilon(\vec{k},\omega) = 1 + \chi_e(\vec{k}\omega) + \chi_i(\vec{k}\omega) \tag{3.11}$$

From the spectral distribution function it can be seen that the total scattered spectrum is the sum of the electron scattered spectra and the ion scattered spectra. To obtain the actual form of Eq. 3.8, we must have the form of the velocity distribution functions.

In a plasma that is quasi-neutral and the particles are assumed to be in thermal equilibrium, the ions and electrons have Maxwellian velocity distribution functions. Thomson scattering measurements are one-dimensional because they only probe along $\vec{k}$, so we only consider a one-dimensional velocity distribution function.

$$f_{q,0}(v) = \left(\frac{1}{\pi v_{Tq}^2}\right)^{1/2} exp\left(-\frac{v^2}{v_{Tq}^2}\right) \tag{3.12}$$

where $v_{Tq} = \sqrt{2k_B T_q/m_e}$ is the thermal speed. To obtain a more explicit spectral distribution function we need the susceptibilities. By using $x_e = \omega/(kv_{Te})$, $x_i = \omega/(kv_{Ti})$ and $\alpha = 1/(k\lambda_{De})$ where λ_{De} is the Debye length then substituting Eq 3.12 into Eqs 3.9 and 3.10 the susceptibilities become

$$\chi_e(\vec{k}\omega) = -\frac{\alpha^2}{2}\frac{\partial}{\partial x_e}W(x_e) = \alpha^2[Re(W(x_e)) + iIm(W(x_e))] \tag{3.13}$$

$$\chi_e(\vec{k}\omega) = -\frac{\alpha^2 ZT_e}{2T_i}\frac{\partial}{\partial x_e}W(x_i) = \frac{\alpha^2 ZT_e}{T_i}[Re(W(x_i)) + iIm(W(x_i))] \tag{3.14}$$

$$W(x_q) = \left(\frac{1}{\pi}\right)^{1/2}\int_{-\infty}^{\infty} dz \frac{1}{z - x_q}e^{-z^2} \tag{3.15}$$

Where $Re(W(x_i))$ and $Im(W(x_i))$ are the real and imaginary parts of the plasma dispersion function, W. Thus the spectral density function is

$$S(k,\omega) = \frac{2\pi^{1/2}}{kv_{T_e}}\left|\frac{1+\chi_i}{\epsilon}\right|^2 e^{-x_e^2} + \frac{2\pi^{1/2}Z}{kv_{Ti}}\left|\frac{\chi_e}{\epsilon}\right|^2 e^{-x_i^2} = \frac{2\pi^{1/2}}{kv_{Te}}\left[\left|\frac{A_e}{\epsilon}\right|^2 + \left|\frac{A_i}{\epsilon}\right|^2\right] \tag{3.16}$$

where A_e and A_i are given by

$$A_e = \left[\left(1 + \frac{\alpha^2 ZT_e}{T_i}Re(W(x_i))\right)^2 + \left(\frac{\alpha^2 ZT_e}{T_i}Im(W(x_i))\right)^2\right] e^{-x_e^2} \tag{3.17}$$

$$A_i = Z\alpha^4\left(\frac{m_i T_e}{m_e T_i}\right)^{1/2}\left[(Re(W(x_i)))^2 + (Im(W(x_i))^2\right] e^{-x_i^2} \tag{3.18}$$

and

$$|\epsilon|^2 = \left[1 + \alpha^4\left(Re(W(x_e)) + \frac{ZT_e}{T_i}Re(W(x_i))\right)\right]^2 + \alpha^4\left[Im(W(x_e)) + \frac{ZT_e}{T_i}Im(W(x_i))\right]^2 \tag{3.19}$$

From this it can be seen that α is the factor that determines the contributions of electron and ion terms. α is known as the scattering parameter which is a measure of how collective a scattered spectrum is. α is defined as

$$\alpha = \frac{1}{k\lambda_{De}} \approx \frac{e\lambda_i}{sin(\theta/2)} \left(\frac{\pi n_{e,0}}{k_B T_e} \right)^{1/2} \tag{3.20}$$

where λ_i is the incident wavelength and the approximation $|k| = 2|k_i|sin(\theta/2)$ was used.

3.4.2 Collective Thomson scattering

When $\alpha > 1$, long-range effects of electrons affected by ions in the plasma are important. Studying long-range electron effects allows the scattering to be coherent, which will be a reflection of both the ion and electron velocity distribution functions. This type of scattering is called collective scattering. Spectra resulting from collective scattering have a non-Gaussian shape, even if the velocity distribution function is Maxwellian.

Collective spectra in this work are due to electron plasma waves and are dominated by two wings on either side of λ_i, as shown in figure 3.6a. The spectrum shown (blue) has a gap around λ_i due to a notch filter used to block the probe beam, which produced a much higher signal than the Thomson spectra. The separation of the wings is proportional to n_e and the width of each of the wings is proportional to T_e. To obtain these values and the total scattered power, the spectral density function in eq. 3.16 must be used. To do this, a fit in the form of the spectral density function is applied to the spectrum and the values for T_e and n_e can be determined from the values for the best fit. An example fit of a collective spectrum is shown as the red line in Fig. 3.6a, which gives values of $n_e = 1.3 \times 10^{17}\ cm^{-3}$ and $T_e = 2.3 \pm 0.3$ eV corresponding to a scattering parameter of $\alpha = 2$.

3.4.3 Non-collective Thomson scattering

When $\alpha << 1$, the scale length of the electron density fluctuation is small compared to λ_D, causing the spectral density function to be proportional to the electron distribution and the

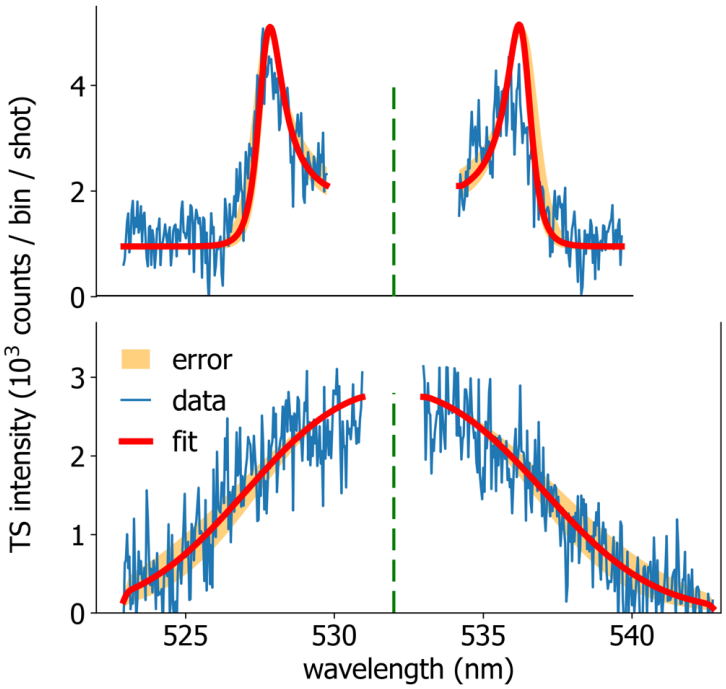

Figure 3.6: Representative collective and non-collective spectra measured via our Thomson scattering diagnostic **Top:** Typical TS collective spectrum (blue) measured at $y < 7$ mm and the PlasmaPy fit (red). **Bottom:** Non-collective TS spectrum (blue) measured at $y > 7$ mm and Gaussian fit (red). The shaded orange regions in both plots represents the error which is about 20% variation of χ^2

scattering to be incoherent. This is called non-collective scattering. Detected non-collective spectra reflect the Maxwellian distribution of electrons and thus have a Gaussian shape. From this, the electron temperature can be determined directly by applying a Gaussian fit to the spectrum

$$T_e = \frac{m_e c^2}{8k_B}\left(\frac{\sigma}{\lambda_i sin\theta/2}\right)^2 = s\sigma^2 \tag{3.21}$$

where s is a constant and σ is the half-width of the Gaussian fit. For the experiments discussed, the constant was determined to be $s = 0.903$ and thus $T_e = 0.903\sigma^2$.

To apply a Gaussian fit to obtain n_e, the relationship between the number of counts detected, N, and n_e is needed. When laser light scatters off microscopic particles, the total number of counts, N, measured by a detector is

$$N = \overbrace{\underbrace{\frac{\tau_L \cdot I_L}{h\nu_i}}_{laser}\underbrace{\Delta V \Delta\Omega}_{collection}\cdot\underbrace{\mu\eta G}_{optics}}^{k} \cdot n \cdot \frac{d\sigma}{d\Omega} \tag{3.22}$$

where τ_L is the laser pulse length, I_L is the probe laser intensity, $h\nu_i$ is the energy of a laser photon, ΔV is the scattering volume, $\Delta\Omega$ is the scattering solid angle, μ is the transmission through the optics, η is the quantum efficiency of the ICCD, G is the ICCD gain, n is the density of the scattering particles, and $d\sigma/d\Omega$ is the differential cross section. The part of this equation that includes the probe beam, the collection optics and the scattering volume is known as the experimental throughput parameter, k, as indicated by the upper bracket. Thus, the total number of counts from a Thomson scattering spectrum is

$$N_T = k \cdot n_e \frac{d\sigma_T}{d\Omega} \tag{3.23}$$

where $d\sigma/d\Omega = r_e^2$ for scattering perpendicular to the probe beam with $r_e = 2.818 \times 10^{-15}$ m is the radius of an electron. k is quite difficult to calculate *a priori*, so it is better and much easier to determine the throughput parameter experimentally. This is done by absolute calibration, which is described in the section 3.4.5. Once k is determined, n_e is obtained from a Gaussian fit to the non-collective spectra using the following relationship:

$$n_e = s \cdot N_T \tag{3.24}$$

where $s = 1/(k \cdot d\sigma_T/d\Omega)$ is a constant with units $cm^{-3}/counts$ and N_T is given by the area under the Gaussian fit. An example of a weakly non-collective spectrum and the corresponding Gaussian fit is shown in Fig. 3.6b. The fit yields values of $n_e = 2.5 \times 10^{16}$ $cm^{-3}$and $T_e = 14 \pm 4$ eV corresponding to a scattering parameter of $\alpha = 0.34$.

3.4.4 Thomson Scattering Setup

The experimental setup used is essentially the same as that used by Kaloyan et al. [47] with a higher power probe laser and the addition of a motorized mirror stage for the probe beam. A schematic of the experimental setup for the Thomson scattering diagnostic is shown in Figure 3.7. The vacuum chamber layout and heating beam were the same as those discussed in sections 4.1 and 3.1.

A frequency-doubled Nd:YAG laser ($\lambda = 532$ nm) was used as the TS probe beam. The probe beam is a high repetition rate laser running at 20 Hz and delivering 460 mJ over a 4 ns pulse. The probe laser is focused using an f/150 spherical lens with a focal length of 75 cm and enters the chamber directly along the plasma blow off axis ($-\hat{y}$). This configuration produces a cylindrical "pencil" beam of 150 μm diameter with a depth of focus of $\pm$3 cm. The mirror that directs the probe beam into the chamber is mounted on a stepper motor drive, allowing the probe beam to be perpendicular to the plasma blow-off axis ($\pm\hat{x}$) with sub-mm precision. The heater and probe beams are synchronized by a trigger pulse, then the probe beam is delayed by a timing box to take data at different times after plasma ablation. However, the lasers run at different repetition rates. To ensure that only one pulse of the 20 Hz probe laser is used for data acquisition, an automated shutter was added to the diagnostic system that opens at a rate of 1 Hz, allowing the first pulse to pass through and then blocking the remaining 19 pulses. Once in the chamber, the probe beam terminates either on the target or in a beam dump mounted behind the target, depending on where

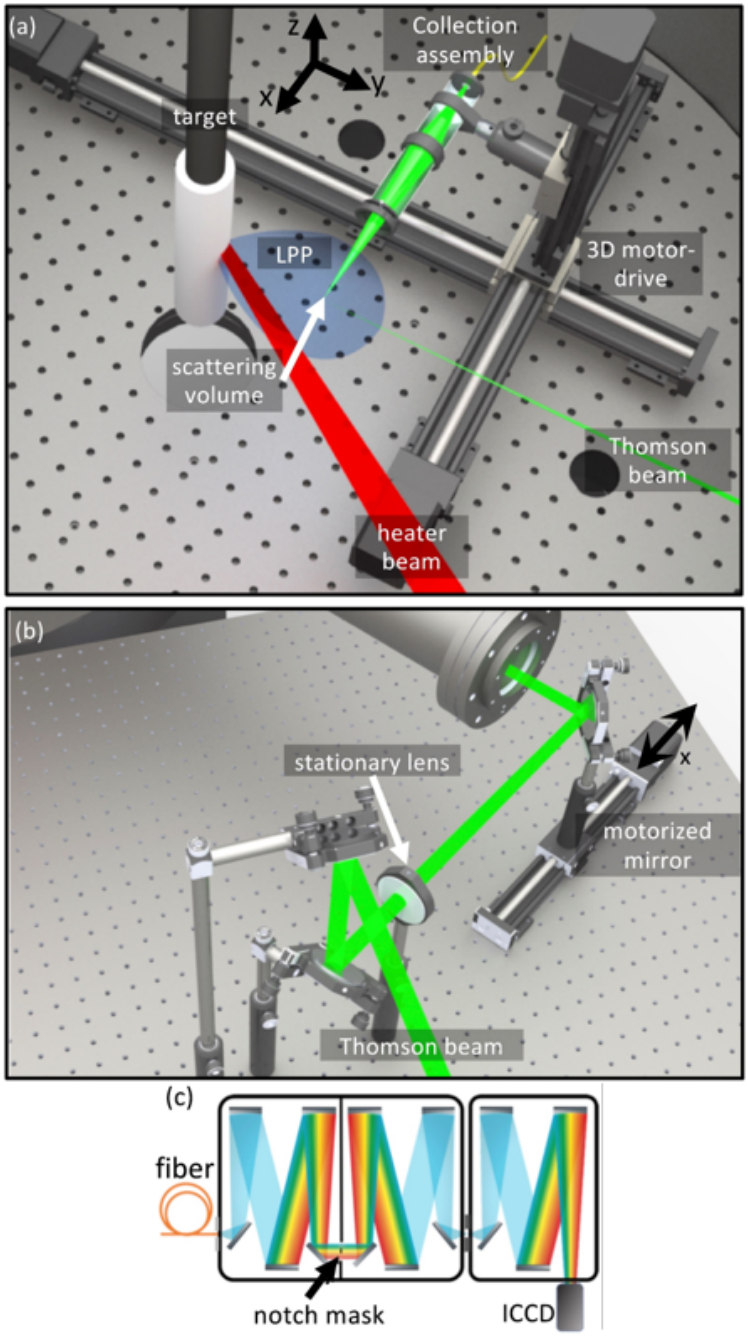

Figure 3.7: (a) Top-down schematic of the Thomson scattering setup with labeled beam configuration, scattering volume, and collecting lens. (b) Beam path of the TS probe laser through the focusing lens and the final motorized rotating mirror. (c) Layout of the light path through the triple spectrometer to the ICCD detector.

the probe beam is along the x-axis. When the laser terminates, it produces larger amounts of stray light, and when it terminates on target, it produces a secondary plasma plume. However, this secondary plume is insignificant to our results because it reached the TS collection volume hundreds of ns after the measurements were taken.

The scattered light was collected perpendicular to the probe beam by a 5.0 cm focal length, 12 mm diameter aspherical collection lens into an f/20 collection cone. This cone was focused at f/5.3 into a 40 m long, 200 μm core optical fiber with a numerical aperture of NA = 0.22. The collection lens projected the fiber with a 3.8× magnification onto the probe beam so that the 0.76 mm diameter fiber core projection exceeds the probe beam by a factor of 3-4. The fiber was coupled to the entrance slit of a spectrometer via a vacuum fiber feed-through. A light-tight 25 mm diameter tube with a 3 mm aperture housed the collecting lens, a fused silica blast shield, and the fiber launch. The collection tube assembly was mounted to a three-dimensional stepper motor drive inside the vacuum chamber. This 3D motor drive was capable of moving to any position within a $10 \times 10 \times 10$ cm^3 volume within the chamber at a repletion rate of 1 Hz and a precision of 5 μm.

The scattering volume is defined by the intersection of the probe beam and the projection of the magnified fiber core cross section. The collection branch is designed to project the fiber core onto the probe beam with a magnification of 3.8, which exceeds the probe beam by a factor of 3-4. The total number of collected photons is proportional to the optical extent of the source, $G' = A' \cdot \Omega'$ where A' is the source area and $\Omega' = \pi/(2 \cdot f\#')^2$ is the solid angle of the collection cone, where in this case $f\#' = 20$ is the f-number of the collection cone. The larger f-number of the collection cone results in a larger source area because the magnification of the fiber onto the probe beam, $M = f\#'/f\#$, increases linearly with $f\#'$, but the f-number on the fiber is fixed, $f\# = 5.3$. and G' scales inversely with $f\#'$. With our parameters, $G' = 3.0 \times 10^{-4}$ $rad\ mm^2$. This gives an efficiency that is 35% of the theoretical upper limit of the spectrometer's throughput ($G_{max} = 8.8 \times 10^{-4}$ $rad\ mm^2$). This acceptable loss of photons significantly reduces the sensitivity of the alignment, making it possible to automatically move the scattering volume along the probe beam using motorized stages [48].

Once collected, the scattered light was fed into a triple spectrometer with a tunable notch filter centered at 532 nm [30], which allowed for a significant reduction in stray light without blocking the TS signal. The spectrometer had a 0.5 m focal length, $f/4$ Czerny-Turner type imaging system with three 1200 grooves/mm holographic aluminum coated gratings blazed at 500 nm. The collected light entered the spectrometer through a 200 μm input slit, was collimated, then imaged via internal toroidal mirrors onto a notch filter, a 2.0 mm intermediate slit, and finally the detector plane. The first two gratings in the spectrometer use subtractive dispersion to reject stray light. The third grating disperses the light onto the detector. As can be seen in figure 3.7(c), a notch filter was placed in the center of the double subtractive spectrometers. This filter was a 0.75 mm wide, 50 μm thick stainless steel mask that blocks a wavelength range of 1.5 nm centered on the wavelength of the probe beam. The total transmission through the triple spectrometer without the notch in place was measured to be 25%. This transmission is dominated by the reflectivity of the three holographic gratings. The spectral resolution was measured to be 0.22 nm over a range of 19.4 nm.

The final spectra were then recorded using a Princeton Instruments Image Intensified Charge Couple Device (ICCD). The camera contains a Generation III photocathode with a quantum efficiency of 50% at a wavelength of 532 nm. The microchannel plate (MCP) was gated at 4 ns and synchronized to the probe beam pulse. The MCP gain was fixed at maximum gain for all measurements and a 2x2 hardware binning was used for all images. Since the spectra of interest did not cover the entire pixel area, the images were further binned over 250 pixels vertically along the fiber and over 2 pixels horizontally for a total of 256 bins at 0.076 nm/bin.

3.4.5 Absolute calibration of Thomson scattering system

The system has been absolutely calibrated by Raman scattering off gas. This calibration method was first performed by Kaloyan *et al.* for 1D raster Thomson scattering experiments[47]. The calibration was performed again during this experimental campaign

to account for the change in probe laser and any optical components.

The calibration was performed by experimentally determining the throughput parameter, k, from Eq. 3.23. This is done using the relative intensity of Raman or Rayleigh scattering from an ambient gas [31]. Rayleigh scattering has the same wavelength as the scattered light, making it very difficult to distinguish between the Rayleigh signal and the scattered light without using a variety of pressures and a notch filter. Raman scattering produces light at wavelengths other than the wavelength of the probe beam, which appears outside the notch filter. Thus, the calibration was done by Raman scattering in 0.86 atm of N_2 gas.

The Raman scattered spectra consist of a series of spectral lines appearing on either side of the notch filter placed at 532 nm. Each peak is the result of a transition between rotational states in the N_2 molecules, with each state characterized by the rotational quantum number, J. J is defined as $E_J = B \cdot J(J+1)$, where $B = 2.48 \times 10^{-4}$ eV for nitrogen. The only transitions allowed are the Stokes, $J \to J+2$, and the anti-Stokes, $J \to J-1$, transitions. Wavelengths produced by red shifted Stokes lines are approximated by

$$\lambda_{J \to J+2} \approx \lambda_i + \frac{\lambda_i^2}{hc} B(4J+6) \tag{3.25}$$

and the total number of scattered photons in a single Raman line with rotational number J is

$$N_{J \to J'} = k \cdot n_J \frac{d\sigma_{J \to J'}}{d\Omega} \tag{3.26}$$

where the differential cross-section is dependent on the state around the weighted average of $3.8 \times 10^{-34}\ m^2$. The density, n_J of rotational state J is

$$n_j = n_{gas} \frac{g_J(2J+1)}{Q} e^{-\frac{E_J}{k_B T}} \tag{3.27}$$

where Q is the partition sum, $Q \approx 9k_BT/B$, and g_J is a wight factor which is either 6 for even J or 3 for odd J. The counts of the Raman spectrum fine-structure as a function of

wavelength is then

$$I_{fs} = k\Sigma_J n_j \frac{d\sigma_{J\to J'}}{d\Omega}\delta(\lambda - \lambda_{J\to J'}) \tag{3.28}$$

Where $\delta(\lambda - \lambda_{J\to J'})$ represents the delta function. Instrument broadening determines the widths of Raman peaks and a synthetic Raman spectrum can be created by convolving the fine structure profile and experimentally measured instrument function, I_{instr}, in the form of $I_{fit} = I_{fs} \otimes I_{instr}$. The total intensity of all Stokes lines is calculated by summing over Eq. 3.28 and determining the area under the synthetic fit. When measuring the Raman scattering, we can determine the total counts in the Stokes spectrum at a certain density by examining all visible Stokes lines at room temperature ($J < 25$).

$$N_{Stokes} = k \cdot n_{gas} \cdot 3.82 \times 10^{-34} m^2 \tag{3.29}$$

The Raman scattering spectrum utilized for calibration appears in Fig. 3.8 and was obtained at 658 Torr of N_2 gas, which corresponds to $n_{gas} = 2.12 \times 10^{19}\ cm^{-3}$. Based on the fit, the detected Stokes signal was $N_{Stokes} = 5.55 \times 10^4$, allowing us to deduce the absolute calibration equation linking N_T with n_e.

$$n_e = (3.11 \pm 0.22) \times 10^{10} N_T. \tag{3.30}$$

3.4.6 Automatic alignment and data collection technique

The collection system was aligned automatically using Rayleigh scattering off of N_2 at approximately 100 mTorr pressure. The alignment process involved fixing the probe beam at x=0 and scanning the collection tube over the probe beam along the $\hat{y}$ and $\hat{z}$-axes, with steps measuring 1 mm × 0.01 mm. The beam's position was determined from the peak of a Gaussian fit. The beam width remains constant throughout the full scanned range of a Gaussian with a width of $\sigma = 0.28$ mm. This stable width is also in line with the probe beam focus's large Rayleigh length.

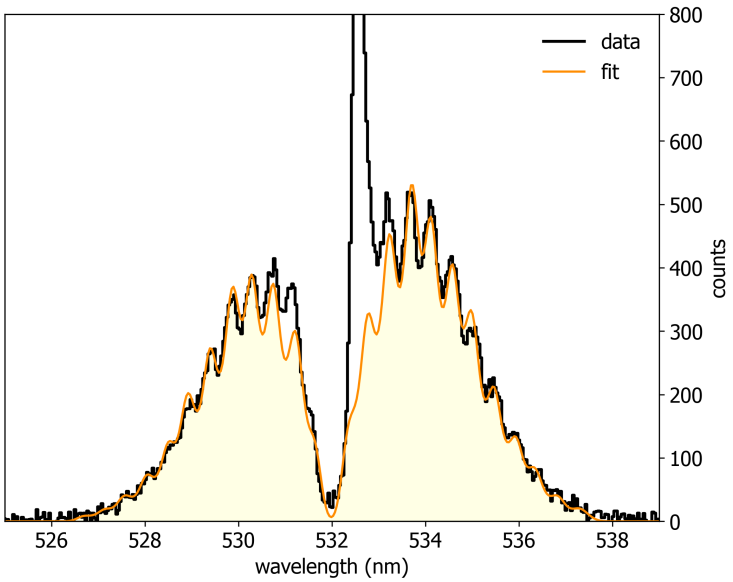

Figure 3.8: Spectrum used for absolute Raman calibration of TS scattering diagnostic. The black spectrum was captured in 658 Torr of N_2 gas and yielded a total Stokes signal of $N_{Stokes} = 5.55 \times 10^4$, which was determined from the yellow area under the applied orange fit. The peak in the spectrum is a result of unshifted Rayleigh scattering that passed through the notch filter and is therefore disregarded in the calibration.

This technique created a height and inclination map of a 2D plane by measuring the beam height along the $\hat{z}$-axis at the four corners of the plane, labeled $C_1 - C_4$. To obtain the data, the beam was moved to the desired x-coordinate and scanned over z in 0.1 mm increments. By using the corner positions, $C_1 = (x_o, 0)$, $C_2 = (-x_o, 0)$, $C_3 = (x_o, y_o)$, $C_4 = (-x_o, y_o)$, the z-coordinate of the beam at any point on the plane can be calculated via the equation.

$$z(x,y) = (1-\frac{x_o - x}{2x_o})(1-\frac{y}{y_o})z_1 + \frac{x_o - x}{2x_o}(1-\frac{y}{y_o})z_2 + \frac{y}{y_o}(1-\frac{x_o - x}{2x_o})z_3 + \frac{(x_o - x)y}{2x_o y_o}z_4. \quad (3.31)$$

Data was acquired by alternating between Thomson and background spectra at every spatial point in a 2D x-y plane. At each spatial position, ten Thomson and background shots were captured and then averaged during data analysis to attain a desirable signal-to-noise ratio and compensate for fluctuating laser intensity (around 5% per shot). The automated data acquisition software synchronously controls the heater beam, target, probe beam, motorized translation stages, and ICCD camera at a rate of 1 Hz. A weakly collective TS spectrum, shown in figure 3.6, can be observed in a N_2 environment of 95 mTorr at 16 mm from the target surface within the blast-wave. This condition occurs 100 ns after heater beam fire. The red line fit is employed to gather data on electron temperature (T_e) and electron density (n_e).

To automatically handle the large volume of TS spectra collected, we utilize the *PlasmaPy* Thomson scattering package in Python[13], along with a fit model script developed by Zhang *et al.*[103]. The script fits the spectra using a nonlinear least squares fit algorithm to produce T_e and n_e values from the *PlasmaPy* spectral density function. In weakly collective spectra, determining n_e from the spectra is not possible and therefore is obtained through a Gaussian fit of the data. Density is then calculated from the total signal intensity using the absolute Raman calibration.

The automated fitting for the collected Thomson spectra generally performed well. However, some spectra produced non-physical values for temperature or density, resulting in diverging T_e and n_e or values several orders of magnitude higher than expected. For these

spectra, fits were manually applied. Comparison between manually applied fits and the fit model script indicated good agreement in both T_e and n_e, except for a few outlier cases.

CHAPTER 4

Experimental Results and Discussion

Multiple experimental campaigns were conducted to investigate magnetic field generation through the Biermann battery effect under different conditions, including vacuum, Nitrogen (N_2) gas at various pressures, and Helium (He) at various pressures. This section shares the results of the experiments, compares them to FLASH simulations, and discusses their significance to astrophysical processes.

4.1 Mapping of Biermann-Generated Fields in Vacuum

To comprehend the behavior of magnetic fields generated by the Biermann battery effect over extensive spatial regions and extended temporal scales, we initially examined the occurrence in a minimally impacted environment. Consequently, we conducted our research in a vacuum environment. The necessary equipment, heater beam, and diagnostic techniques used for the data presented in this section are detailed in Chapter 3.

Magnetic flux measurements were taken at different distances from the target surface, and in multiple planes. The magnetic flux was calculated using equation 3.4, based on the voltage traces obtained through measurement. The resulting magnetic fields' error was calculated from the standard deviation of five shots per each position on target. Averaging over these five shots per position accounts for the laser energy fluctuations from shot to shot (2-5%) and improves signal-to-noise ratio.

The B-dot probe was positioned and scanned in multiple transverse planes, ranging from 7 to 42 mm from the target surface, with each plane separated by 5 mm. These planes

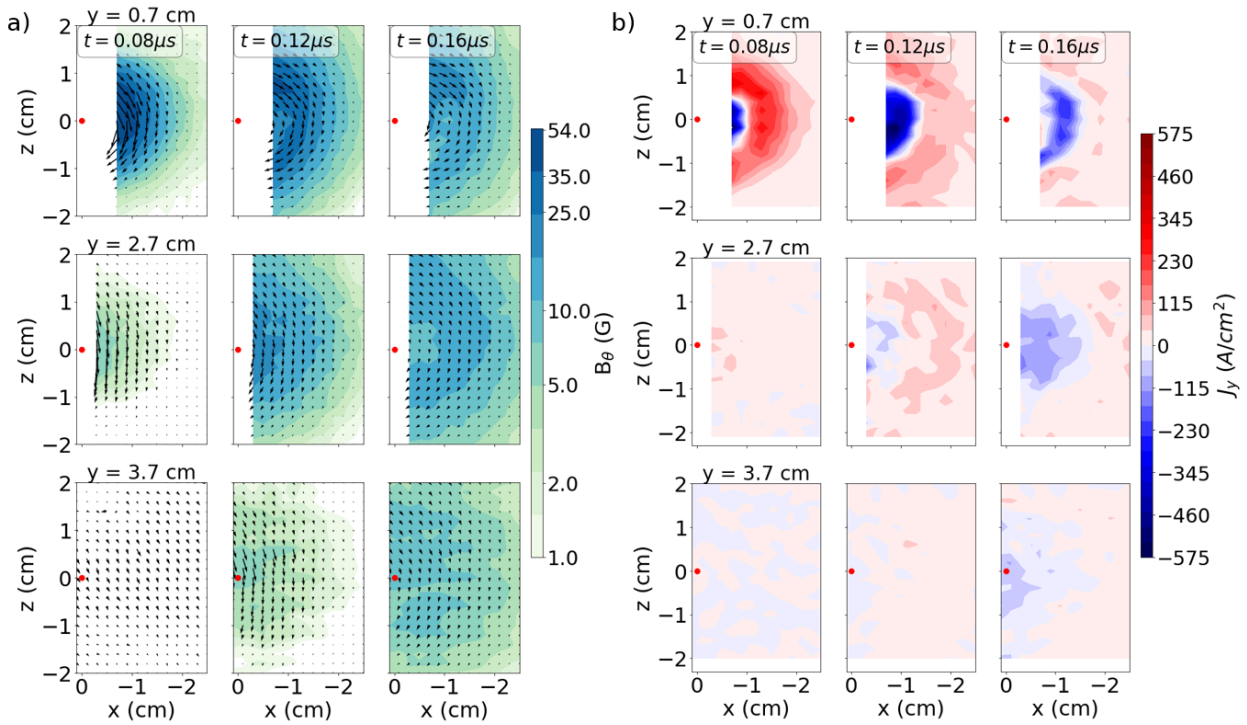

Figure 4.1: **a)** Contour plots show the azimuthal magnetic field structure in different transverse planes at three representative times, with magnetic field vectors depicted as black arrows. **b)** The current density along the plasma blow-off axis is calculated in various transverse planes at three representative times. The laser spot is indicated by a red dot and positions where the probe could not reach due to mechanical constraints are represented as blank spaces.

were then combined to enable three-dimensional analysis of the magnetic field structure. Figure 4.1a depicts a representative data segment of the magnetic field. This figure shows three data planes displaying the detected azimuthal magnetic fields, B_θ, at three different distances from the target surface. In these planes, the LPP expands out of the page, with the propagation axis origin indicated by a red dot in each plot. The contour values represent the magnitude of B_θ and the black vectors overlaid on the plots indicate the orientation of the magnetic field, as measured by the B-dot probe.

The maximum azimuthal magnetic field values decrease as distance from the target increases (see Figure 4.1a). Figure 4.2 shows the maximum azimuthal magnetic field values

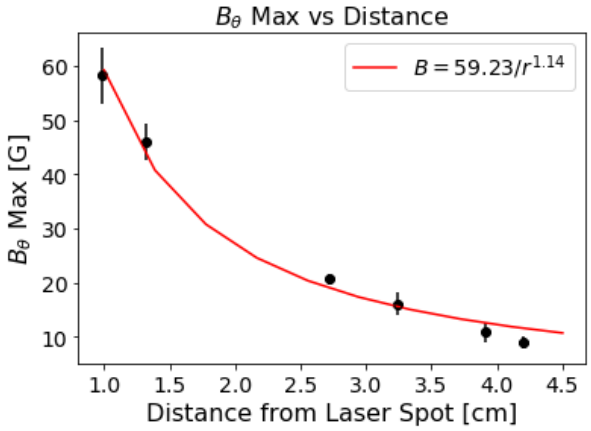

Figure 4.2: Plot showing the maximum azimuthal magnetic field versus distance from the laser spot. Each point corresponds to the times in Figure 4.4. The data fits well with a $1/r^a$ curve (red line) with a value of $a = 1.3$.

for all planes, plotted against distance to the plane. The data reveals good agreement with a $1/r^a$ fit, while the inverse distance fit illustrates a $1/r^{1.3}$ spatial decay for maximum magnetic field values as a function of distance from the target. Similar behavior was observed in previous experiments[91].

We calculate the current density J_y normal to each x-z plane of data using Ampere's law, $J \propto \nabla \times B$. The current densities are shown in Figure in 4.1b, corresponding to the same parameters as Figure 4.1a. Initially, the current density within each plane flows in the direction of plasma propagation (not shown). At times corresponding to the detection of Biermann fields, the current begins to flow in both the positive (red) and negative (blue) directions along the blow-off axis. The current flowing toward the target surface begins near the origin of the plane and expands radially outward along with the Biermann fields. This current structure suggests that a current loop has formed, with the central current acting as a return current. Our measurement planes are too course to allow calculations of three-dimensional current structures, these measurements should be attempted in future experiments. Based on FLASH simulations which are discussed in section 4.5.1, the current structures seen in Figure 4.1b are formed from spatial gradients of the Biermann magnetic

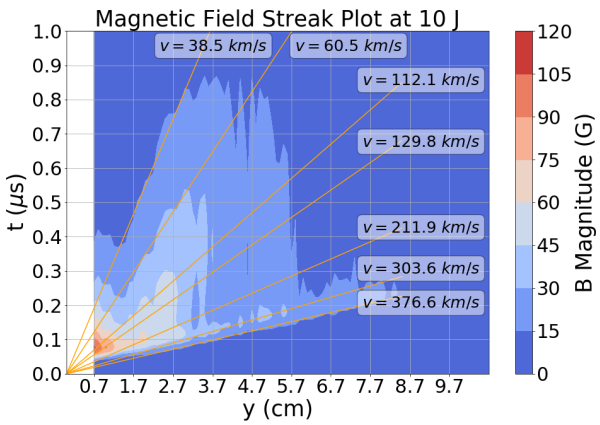

Figure 4.3: A streak plot showing the total magnetic field (contour) generated from a y-lineout at $x = -0.7$ mm, $z = 0$ mm. Orange lines represent linear fits applied to magnetic field features for determining their respective speeds.

fields.

Figure 4.3 displays a streak plot of the magnetic field at $x = -0.7$ mm. Linear fits were employed to various characteristics in the plot to estimate the magnetic field expansion speed, which ranged from 300 - 370 km/s. This is comparable to the ∼330 km/s expansion velocity estimated by time-of-flight measurements of the peak magnetic field, as displayed in Fig. 4.4. An analytical model developed by Shaeffer et al.[80] applied to the laser plasma expansion gives a result of $v \approx 300 \pm 50$ km/s, which matches the speed of the magnetic fields experimentally determined and thus indicates that the magnetic fields are moving with the plasma bubble via advection, as explained further below.

Electron temperature and density values were measured using an optical Thomson scattering (TS) diagnostic described in Chapter 5. A single data point at y = 1.5 cm from the heater beam spot along the blow-off axis indicates that T_e is 10 ± 2 eV and n_e is (5.55 ± 1) × 10^{16} cm^{-3}. Using this Thomson scattering and magnetic field data, we directly calculate the magnetic Reynolds number via equation Ref. 2.29 to be $R_m \approx 1.4 \times 10^4$ at y = 1.5 cm. At this point in the system, the advection with the plasma fluid flow is dominant in the propagation of magnetic fields.

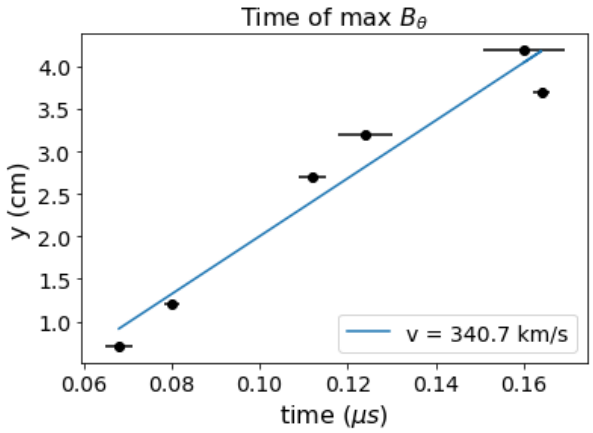

Figure 4.4: Graph displaying the highest azimuthal magnetic field measured by the magnetic flux probe (black) at various time intervals. A linear fit (blue line) indicates a velocity of 330 km/s.

Now that we had an understanding of how Biermann fields are generated in a vacuum, we wanted to study Biermann fields under different conditions. Results from FLASH simulations by M.B.P. Adams showed that in the presence of a background gas the laser could produce shock waves and lead to an increase in n_e and T_e, as well as higher gradients, and thus higher Biermann generated magnetic fields. We therefore decided to study Biermann field generation in the presence of hydrodynamic shock waves.

4.2 Characterization of Shock Waves via Self-Emission Images

Before measuring the Biermann fields in background gases, we imaged the LPP in various background gases to determine the onset of hydrodynamic shock wave formation and to characterize the resulting shocks. This was accomplished using the setup discussed in section 3.3.

For the type of shocks discussed in this thesis, we examine the propagation of a high-intensity spherical shock resulting from the instantaneous release of a significant amount of energy in a small volume (in our case, from an LPP ejection). Assuming that the pressure,

p_2, behind the shock front is significantly higher than that of the gas the shock expands into, p_1, the shock flow depends only on the initial gas density, ρ_1, and the energy produced by the explosion, E. Based on this, a dimensionless ratio can be expressed as $\xi = r(\rho_1/Et^2)^{1/5}$. Using this dimensionless combination, a self-similar solution for shock propagation can be derived, as described in [52]. The rate at which the shock wave propagates through time is determined by:

$$r_o = \xi_o \left(\frac{E}{\rho_o}\right)^{1/5} t^{\alpha} \tag{4.1}$$

where ξ_0 represents a constant associated with ξ, r_0 denotes the distance between the origin and the shock, and time is denoted by t. In the previously described self-similar scenario, $\alpha = 2/5$. This type of shock wave is commonly referred to as a Sedov-Taylor blast wave[85]. Since Sedov-Taylor blast waves are adiabatic, they are non-radiative shocks. However, for other instances when radiation is present and removes energy from the shock, the relation $r \propto t^{\alpha}$ still holds but shock expansion occurs at a slower pace according to analytical solutions. For $\alpha = 2/7$, the pressure-driven snow plow is observed. For $\alpha = 1/4$, the momentum-driven snowplow occurs with the shock coasting, while for $2/7 < \alpha < 2/5$, only partial radiation of thermal energy from the shock is detected.[40].

To determine the type of shock forming in the experimental system, self-emission images were captured of the LPP at different pressures and times using N_2 and He background gas fills. Self-emission images were taken by a CCD camera along the $\hat{x}$ axis producing images of the blast waves in the y-z plane. Self-emission images of blast waves observed in both N_2 and He at different pressures are displayed in Figure 4.5 and Figure 4.6, respectively, at $t = 100 \pm 5$ ns. The panel for He at a pressure of 25 mTorr was not captured; hence it is intentionally left blank in the figure. As the pressure increases, the shock waves become sharper and travel shorter distances for both background gases. No shocks were observed in helium up to a pressure of 280 mTorr, which is significantly higher than the pressure at which shocks were seen in nitrogen. The sound speed in helium at the pressures where the images were taken is approximately $v_s = 1$ km/s, well below the initial LPP velocity, which suggests that shocks should have formed. We hypothesize that either the shocks were too

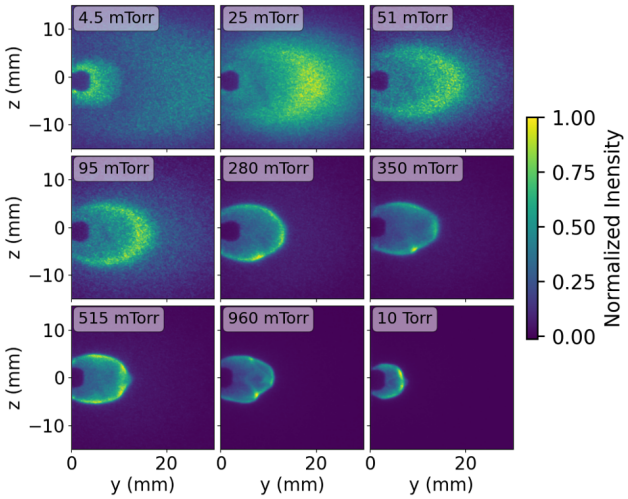

Figure 4.5: Normalized self-emission images of laser driven blast waves in various pressures of N_2 gas at t = 100 ns after heater beam fire.

diffuse or there was insufficient self-emission for the CCD camera to detect them. Hence, only shocks in helium above a pressure of 280 mTorr were characterized.

Streak plots depicting blast wave fronts versus time were generated from line-outs along the LPP blow-off axis in the ICCD images, for every time point. Figure 4.7a and b show the streak plots of the blast wave front versus time along the LPP blow-off axis for 95 mTorr of N_2 and 510 mTorr of He background gas. A linear fit was used to the leading edge of Figure 4.7a and b, yielding the LPP leading edge velocity in N_2 and He of $v = 370$ km/s. This velocity is consistent with bulk laser-plasma ion velocity measurements made with identical laser target parameters using laser-induced fluorescence [21, 19] and time-of-flight spectroscopy [20].

By applying a fit to the blast wave front, it was determined that the blast waves in both N_2 and He initially propagate linearly, but at about 60 ns begin to propagate at a rate of $r \propto t^{2/5}$. From this we concluded that the shock waves generated were Sedov-Taylor shock waves. Streak plots at other pressures of N_2 and He give similar streak plots and also have expansion rates of Sedov-Taylor shock waves.

Sedov-Taylor shock waves were formed in both He and N_2 background gases, but, since

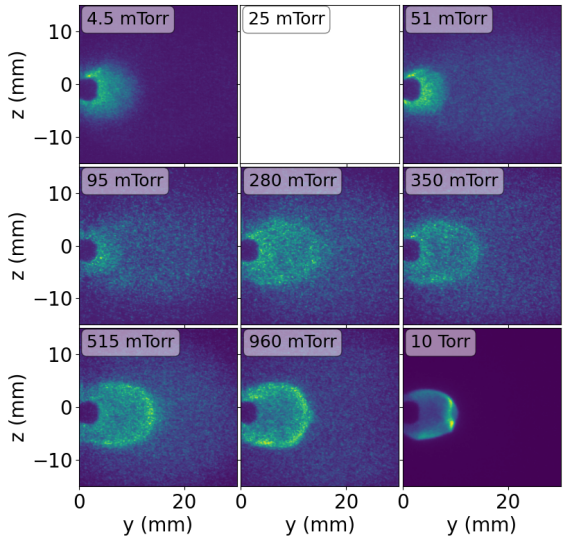

Figure 4.6: Normalized self-emission images of laser driven blast waves in various pressures of He gas at t = 100 ns after heater beam fire. The image for 25 mTorr is left blank because no images were taken at this pressure of He.

He is much lighter, higher pressures was required to reach similar intensities and velocities as in N_2. Based on the Thomson scattering data discussed in section 4.3.2, similar values of T_e and n_e are obtained in He at P= 700 mTorr and N_2 at P= 95 mTorr.

4.2.1 Blast Wave Characterization

The Mach number of the Sedov-Taylor shock waves was determined for times up to 600 ns after the firing of the heater beam. A plot of Mach number versus time for N_2 and He is shown in figure 4.8. The speed of sound was calculated for both N_2 and He at their respective pressures using $C_s = \sqrt{\gamma P/\rho}$, where γ is the adiabatic index, P is the pressure, and ρ is the mass density of the gas. For N_2 at 95 mTorr $C_s = 350$ m/s and for He at 700 mTorr $C_s = 1013$ m/s. The velocity of the shock waves as a function of time was found by taking the time derivative of the radial expansion of the shock waves determined by the fit functions applied to the streak plots in figure 4.7. The shock waves in 95 mTorr N_2 range from 216 at

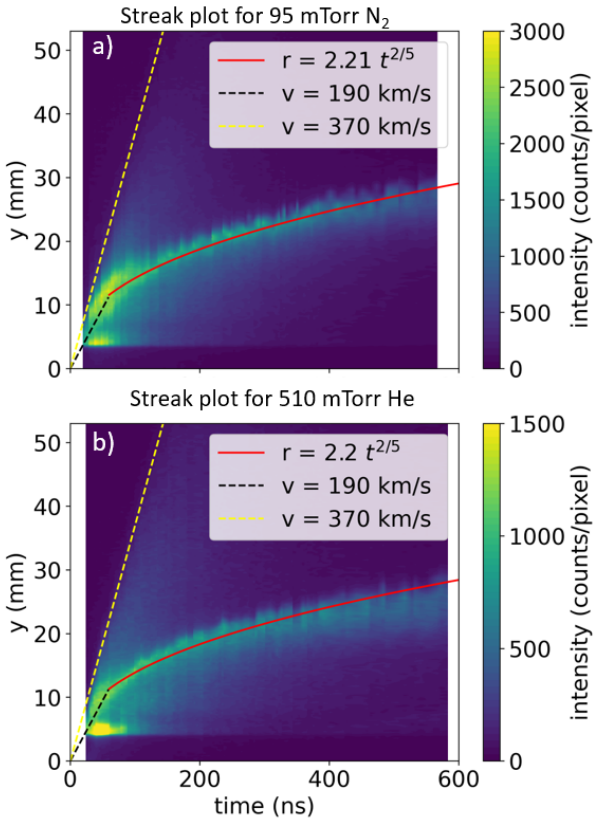

Figure 4.7: Streak plots for N2 and He background gas. **a)** Streak plot in 95 mTorr of N_2 background gas. **b)** Streak plot in 510 mTorr of N_2 background gas. Linear fits (yellow dashed line) of leading edge reveal the leading edge velocity of the LPP in N_2 and He of $v = 370$ km/s. Linear fits (black dashed lines) of the initial expansion of the shock give $v = 190$ km/s. Fits applied to the blast wave front give an expansion rate of $r \propto t^{2/5}$ showing these are Sedov-Taylor blast waves.

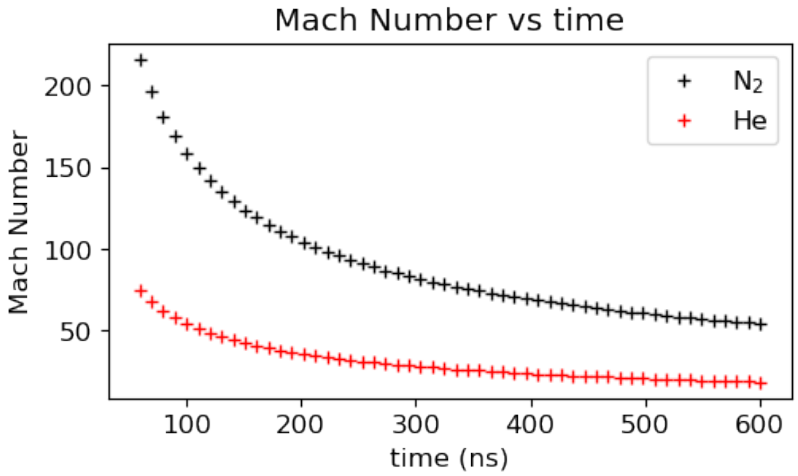

Figure 4.8: Mach number vs time of the observed Sedov-Taylor blast waves for N_2 (black) and He (red).

shock formation to 54 at 600 ns. At 700 mTorr He, the pressure at which the TS data were obtained, Mach numbers ranged from 74 at shock formation to 19 at 600 ns. At the time of the TS data, $t = 100$ ns, the Mach number of the shocks in N_2 was $M_{N_2} = 158$ and the Mach number of the shocks in He was $M_{He} = 55$.

The position and width of the shocks for N_2 and He at $t = 100 \pm 5$ ns for all pressures were determined by examining the intensity of a strip of pixels along the $\hat{y}$ axis of the self-emission images. However, these images are a 2D projection of 3D LPPs, which causes line-of-sight distortions in the captured images. To account for this, inverse Abel transforms were applied to the images. An Abel transform is an integral transform used to analyze spherical or axially symmetric functions or objects. There are two types of Abel transforms, forward and inverse. Forward Abel transforms are used to project an optically thin, axially symmetric emission function onto a plane, while an inverse Abel transform is used to calculate the emission in a plane given a projection (i.e., an image) of an emission function. We have images of a 3D emission, so we apply inverse Abel transforms to the images. The inverse Abel transform is given by:

$$f(r) = -\frac{1}{\pi}\int_r^\infty \frac{dF}{dy}\frac{dy}{\sqrt{y^2 - r^2}} \tag{4.2}$$

where dF/dr is the emission function, y is distance from origin of object and r is radius of the emission object. The inverse Abel transforms were applied to images using the PyAbel python package[32].

Line-outs of a 10 pixel strip centered on the y-axis were then performed on the Abel inverted images. Line-outs of the Abel inverted images at each pressure for both background gases are shown in figures 4.9 and 4.10. A comparison of the lineout for the original and Abel inverted images is shown in figure 4.12b. This comparison shows that the Abel inversion corrects the images by removing the intensity spike before the shock wave peak due to the plasma bubble in planes in the near and far field of the imaging plane.

The position and width of the shocks for N_2 and He at $t = (100 \pm 5)$ ns for pressures ranging from 4-1000 mTorr were determined by examining the Abel inverted line-outs and using the mean and standard deviation of Gaussian fits to these line-outs. A comparison of how the shock wave parameters change with pressure in He and N_2 is shown in figure 4.12a and 4.12c, respectively. The fit (purple line) to the nitrogen data in figure 4.12c shows the width $\sigma_{conv} = (\sigma_1^2+\sigma_2^2)^{1/2}$ of the Gaussian obtained by convolution of the Gaussian blast wave profile with variance σ_1^2 and the Gaussian spatial resolution profile with variance σ_2^2. The fit is consistent with a blast wave width proportional to the mean free path $\sigma_1 \sim \lambda_{mfp} \sim p^{-1}$, decreasing inversely with gas pressure p, and a spatial resolution of 1 mm full width at half maximum dominating the data at higher pressures. Measurements in He at low pressures indicate that shock waves are not formed. Therefore, the relationship between shock wave width and position for He could not be concretely established, although the points at p = 280, 350, 515, and 960 mTorr show a similar trend as in N_2 over pressures of 4-1000 mTorr, respectively.

4.3 Thomson scattering measurements of laser induced blast waves

The electron temperature and density gradients are needed to determine whether Biermann fields were generated in blast wave fronts. A multi-month experimental campaign was con-

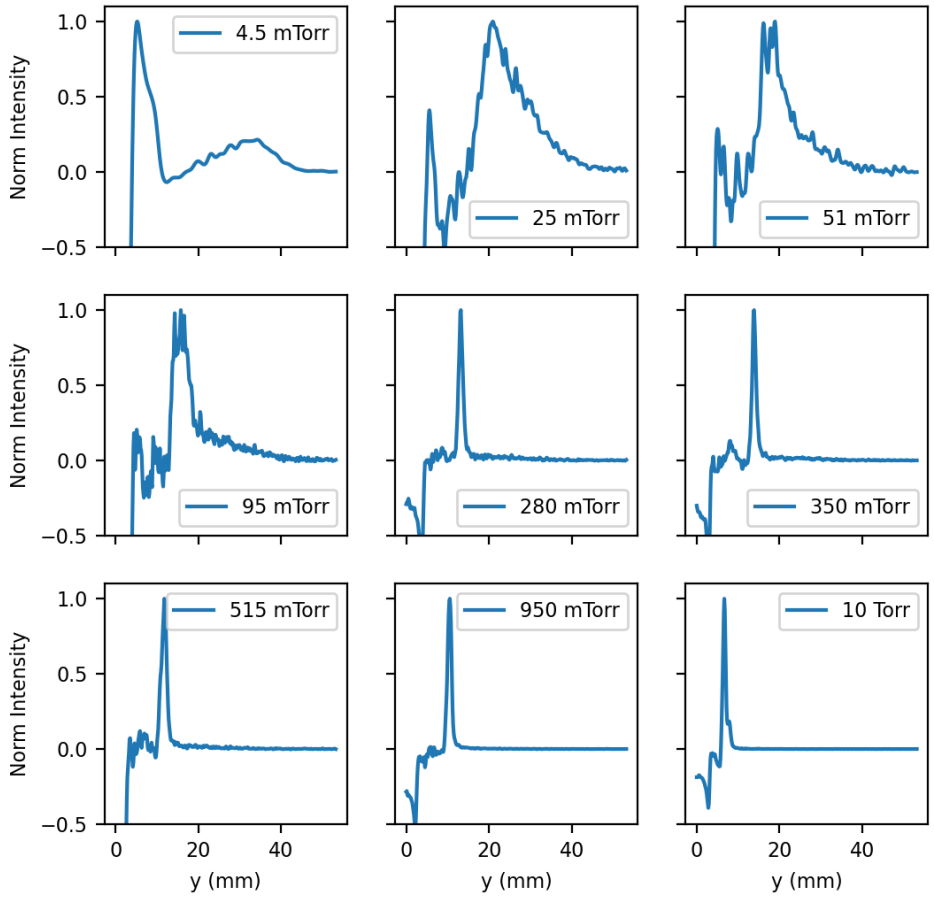

Figure 4.9: Abel inversions of a line-out of pixels along the y-axis for images taken at various pressures of N_2 gas.

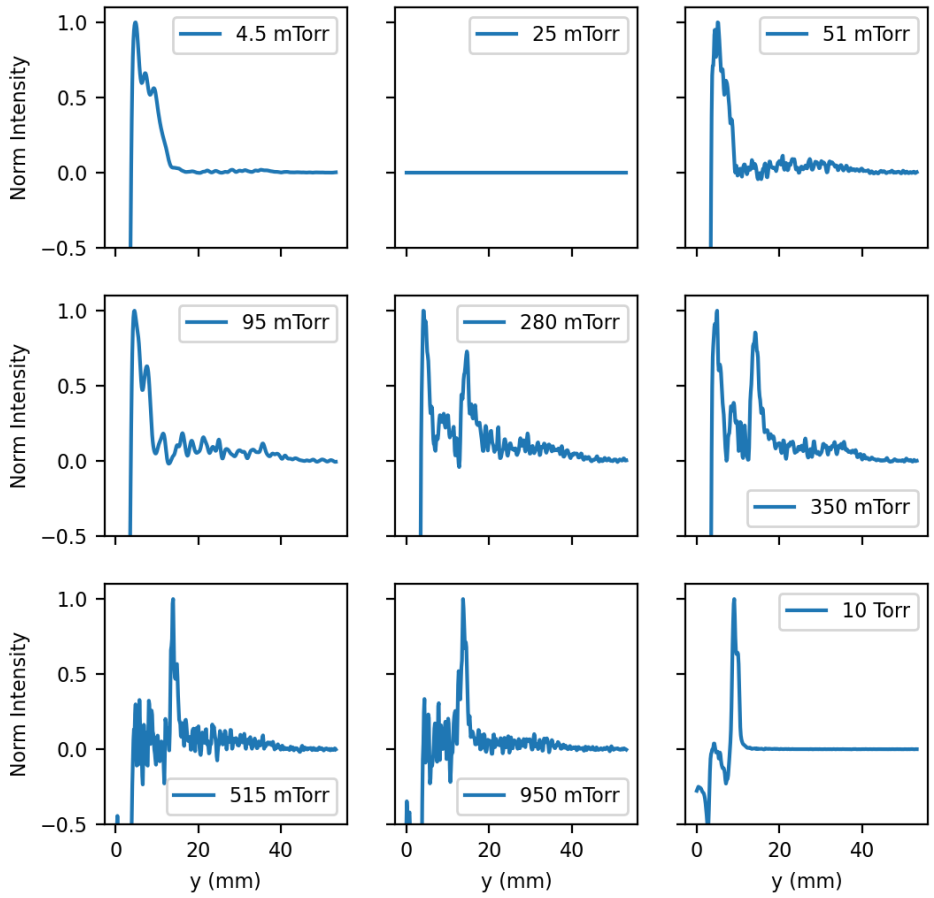

Figure 4.10: Abel inversions of a line-out of pixels along the y-axis for images taken at various pressures of He gas. The 25-mTorr line is flat because no images were taken in He at that pressure.

ducted using 1D[47] and 2D[103] Thomson scattering to measure T_e and n_e in laser generated shock waves over a pressure range of 4-1000 mTorr in both N_2 and He background gas. Examples of the collective and non-collective spectra measured during this campaign are shown in figure 4.11. The high-repetition rate capability of the laser driver and the novel raster Thomson scattering diagnostic enabled the first ever measurements of ∇T_e and ∇n_e in an LPP, indicating production of Biermann effect in blast wave fronts. The theory behind Thomson scattering is described in the sections 3.4.1, 3.4.3 and 3.4.2. Information on experimental setup, absolute calibration and data processing is given in sections 3.4.4, 3.4.5 and 3.4.6 respectively.

4.3.1 One dimensional Thomson scattering measurements

Thomson scattering spectra were measured in 1D line-outs along the blow-off axis for a variety of pressures of both N_2 and He. The setup used for all TS measurements is described in section 3.4.4. The relationship between T_e and n_e in the blast waves vs. pressure, shown in figure 4.12d and Figure 4.12e respectively, are determined from Thomson scattering measurements taken in one-dimensional (1D) line-outs along the blow off axis for a range of pressures between 4-1000 mTorr. T_e increases with pressure in both the He and N_2, following the same general upward trend for both background gases, with maximum values at 1000 mTorr reaching $T_e = 23 \pm 6$ eV for N_2 and $T_e = 27 \pm 3$ eV for He. n_e increases with pressure as the mean free path in the shock front decreases, reaching a maximum of $n_e = (3.0 \pm 0.3) \times 10^{16}\ cm^{-3}$ for 1000 mTorr of He and $n_e = (2.6 \pm 1.0) \times 10^{16}\ cm^{-3}$ for 1000 mTorr of N_2. The values for n_e in the shock waves are higher in N_2 than in He, due to the smaller collision mean free path in N_2. From the blast wave parameters vs. pressure, it is concluded that as pressure increases, the blast waves travel at higher velocities and the mean free path decreases, corresponding to an increase in electron density and temperature inside the blast wave fronts. It should be noted that the blast wave width shown in Figure 4.12c is the convolution of the width of the shock and the resolution of the ICCD camera, thus the actual mean free path ($\lambda_{mfp} \propto 1/P$) is smaller than what is shown in this figure.

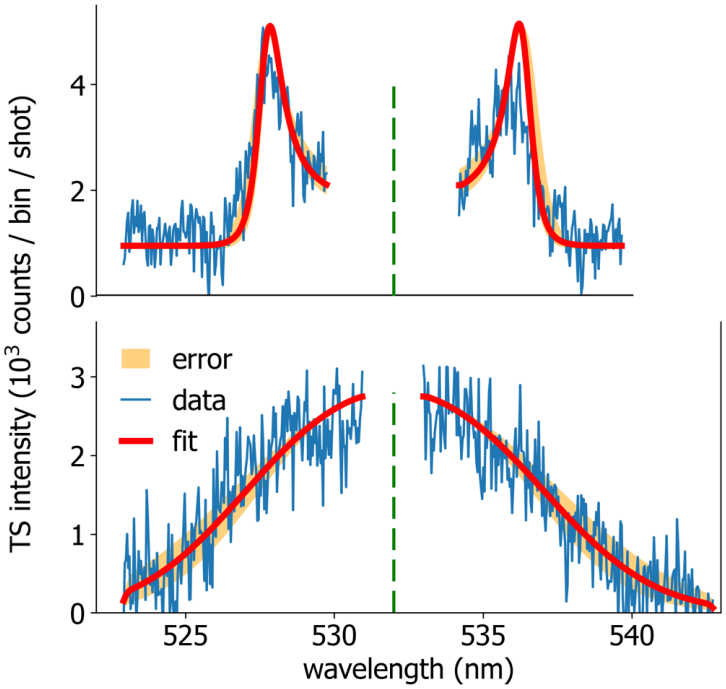

Figure 4.11: Examples of collective and non-collective spectra measured via our Thomson scattering diagnostic. **Top:** Typical TS collective spectrum (blue) measured at $y < 7$ mm and the PlasmaPy fit (red). The shown spectra give values of $n_e = 1.3 \times 10^{17}\ cm^{-3}$ and $T_e = 2.3 \pm 0.3$ eV corresponding to a scattering parameter of $\alpha = 2$. **Bottom:** Non-collective TS spectrum (blue) measured at $y > 7$ mm and Gaussian fit (red). The shown spectra has values of $n_e = 2.5 \times 10^{16}\ \ cm^{-3}$and $T_e = 14 \pm 4$ eV corresponding to a scattering parameter of $\alpha = 0.34$. The shaded orange regions in both plots represents the error which is 20% variation of χ^2

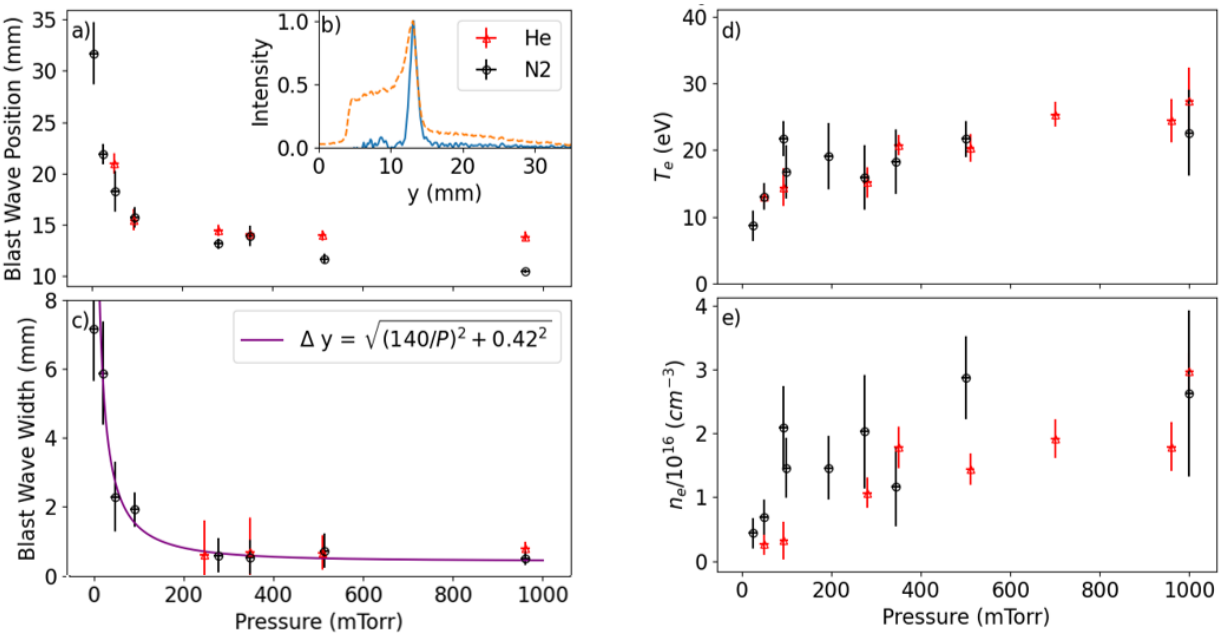

Figure 4.12: Measured parameters of blast waves in N_2 (black circles) and He (red triangles) background gas at $t = 100 \pm 5$ ns. **a)** Position of blast wave vs pressure. No data is shown for He below a pressure of 280 mTorr as shock waves were not visible in self emission images at lower pressures. **b)** Representative blast wave line out from original images (orange dash) and an Abel inverted image (solid blue). Intensity shown has been normalized. **c)** Blast wave width vs pressure. Purple line represents fit Δ y = $\sqrt{(140/P)^2 + 0.42^2}$. d) Electron temperature vs pressure inside blast waves fronts. **e)** Electron number density vs pressure inside blast waves fronts.

A comparison of how T_e and n_e vary with distance from the target at $t = 100$ ns after laser fire in vacuum, 94 mTorr N_2 and 94 mTorr He is shown in Figure 4.13a and Figure 4.13b, respectively. The T_e and n_e values in vacuum (blue) are initially high due to the plasma near the target surface, then drop to near zero and remain constant as the distance from the target increases. The shock wave region is visible in the peaks in T_e and n_e for N_2 (black). This data (red) also shows a peak in T_e but not in n_e, most likely because this is a region where plasma is present but the density is not high enough to form a shock wave. The values of T_e in N_2 are much higher and peak closer to the target surface than those in He. This is due to the higher density and effective charge state of the N_2 gas causing the mean free path of N_2 at 95 mTorr ($\lambda_{N_2} \approx 0.8$ mm) to be smaller than that of He at 95 mTorr, ($\lambda_{He} \approx 7.2$ mm). The increase in n_e for the N_2 background gas is sharper than that of the T_e values. The broadening of T_e is a result of heat transfer from the electrons in the blast wave to the surrounding plasma.

1D TS line-outs were also taken at a range of times between 4-260 ns after the heater beam fire in 95 mTorr of N_2 gas. Plots of n_e and T_e vs. y at various times are shown in figure 4.14. It can be seen in the top plot of figure 4.14 that the shock waves are most dense between 33-55 ns, reaching peak densities of up to $12 \times 10^{16}\ cm^{-3}$. The high density seen near the target at early times is due to plasma near the target surface. As can also be seen in the 4.1 figure, the density drops to nearly zero until it peaks again at the shock wave. Small density peaks further away from the target are also present at all times with values of about $n_e = 2 \times 10^{16}\ cm^{-3}$. These small peaks correspond to the position of the shock wave at the measured time. The electron density in the shock wave seems to stay around a value of $n - e = 2 \times 10^{16}\ cm^{-3}$ as it expanded with time. The electron temperature, shown in the lower plot of figure 4.14, generally increased with time and peaked at a value of about $T_e = 28$ eV around 200 ns. The temperature peaks occurred at the same spatial positions as their corresponding density peaks, but the widths of the spikes are much wider. This is most likely due to heat exchange with plasma downstream and gas upstream of the shock wave. It was observed that the density and temperature begin to decrease at 260 ns. At this

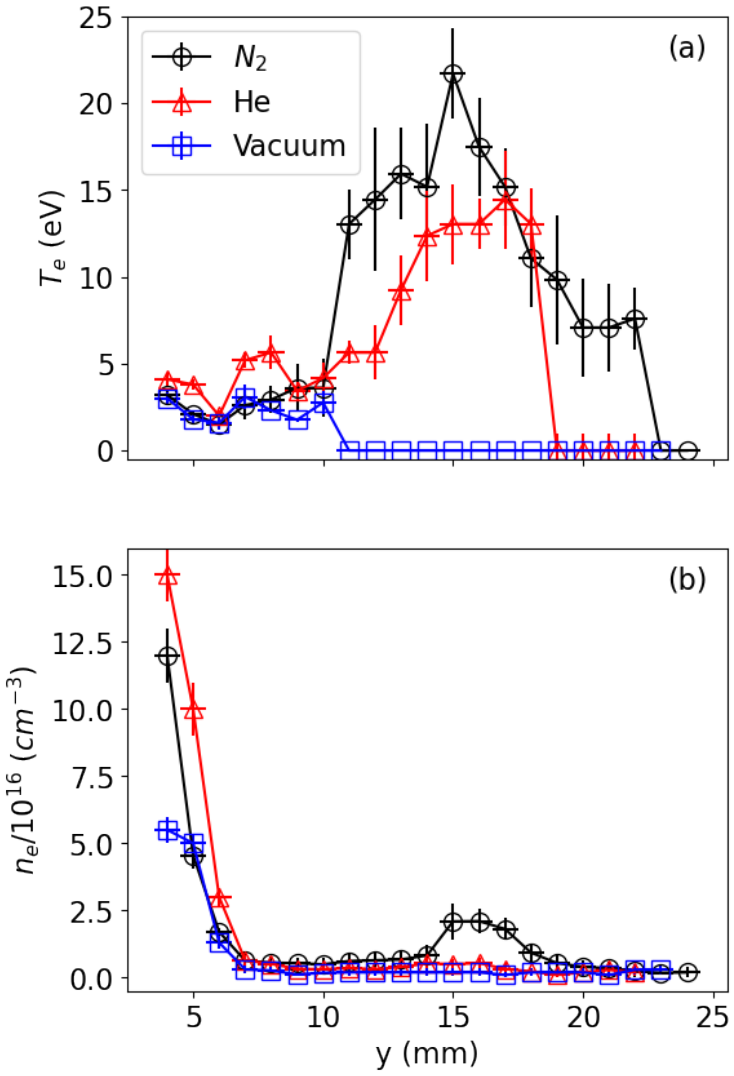

Figure 4.13: Comparison of T_e and n_e in vacuum (blue squares), 95 mTorr N_2 (black circles) and 95 mTorr He (red triangles) versus distance from the target surface. (a) Electron temperature (T_e) versus y. (b) Electron density (n_e) versus y.

point, the shock wave has lost most of its momentum and begins to diffuse.

4.3.2 Two dimensional Thomson scattering measurements

TS scans were also performed in two dimensions (2D) for 95 mTorr of N_2 and 700 mTorr of He. Two-dimensional maps of electron temperature and number density are shown in figure 4.15. The data are only plotted along the -$\hat{x}$ axis, but due to the cylindrical symmetry of the shock waves and the LPP, it can be assumed that both the n_e and T_e data are symmetric along $\hat{y}$. The TS planes in both background gases reveal the blast waves seen in the self-emission images and confirm that both T_e and n_e are higher in the blast wave front than the plasma above and below the blast wave. The blast waves in 95 mTorr N_2 (figure 4.15a) have electron temperature and density reaching values of $T_e = 25$ eV and $n_e = 2 \times 10^{16}$ cm^{-3}. The shock waves in He (figure 4.15b) have the same density values as $n_e = 2 \times 10^{16}$ cm^{-3}, but the temperature reaches a slightly higher value of $T_e = 30$ eV. Helium radiates less than N_2, as reflected by the appearance of fewer spectral lines. Again it can be seen that T_e is much broader than n_e in the blast waves for both gases due to heat exchange with the surrounding plasma before and after the blast wave. The elliptical shape of the blast wave is consistent with a typical initial angular velocity distribution of laser-produced plasmas of $v \sim cos^2(\Theta)$, where Θ is the angle relative to the blow-off axis [44].

Four data planes were collected and averaged in N_2 gas, but only one plane was taken in He. Although the He data have lower resolution, it is clear from the figure 4.15 that the shock waves in 700 mTorr of He and 95 mTorr of N_2 have nearly identical shape, n_e and T_e values. This confirmed our earlier conjecture from the self-emission images that the blast wave dynamics and magnetic field generation should behave similarly in both systems. Henceforth, magnetic field data were only collected in the presence of 95 mTorr of N_2.

The 2D TS data in N_2 were used to obtain novel measurements of the T_e and n_e gradients within an LPP system. These gradients were computed separately in the $\hat{x}$ and $\hat{y}$ directions, as shown in Figure 4.16. The gradients were computed along each axis using second-order

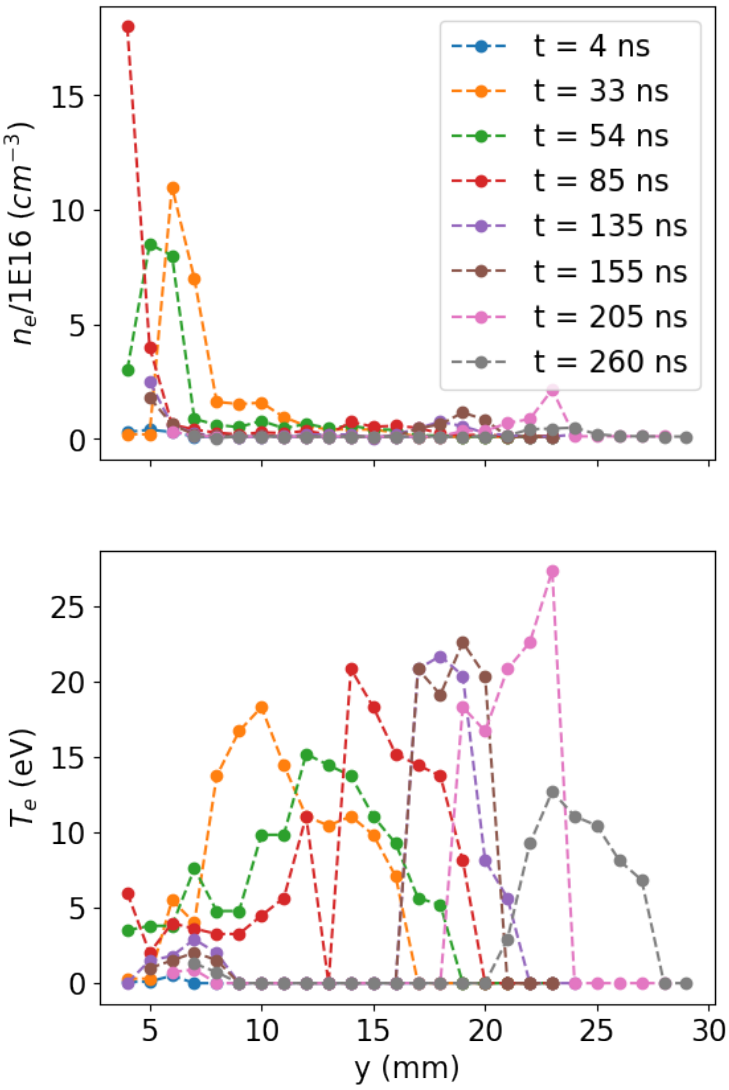

Figure 4.14: y line-outs of n_e and T_e for various times after heater beam fire. (top) n_e vs y for 8 times after heater beam fire. Each color represents a different time. top) T_e vs y for 8 times after heater beam fire. Each color represents the same times in the top plot.

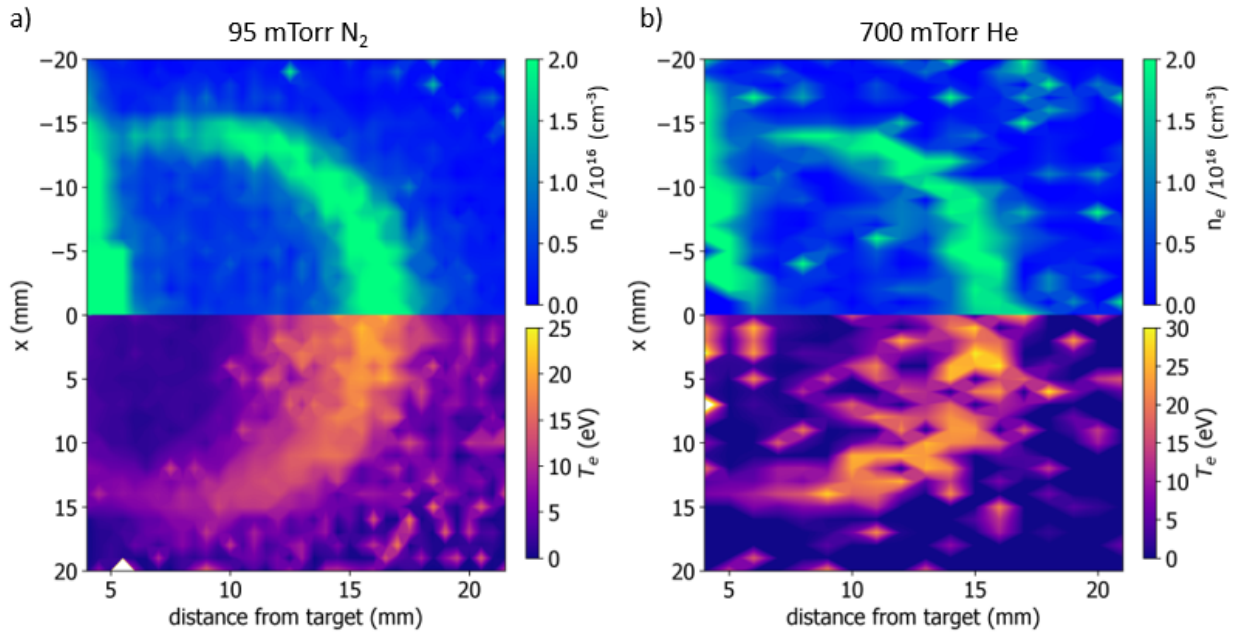

Figure 4.15: Two dimensional map of n_e and T_e in Sedov-Taylor blast waves. **a)** Measurements in 95 mTorr of N_2 gas. Top: map of $n_e/10^{16}$ cm^{-3}. Bottom: mirrored map of T_e. **b)** Measurements in 700 mTorr of He gas. Top: map of $n_e/10^{16}$ cm^{-3}. Bottom: mirrored map of T_e. The mirroring of the T_e data does not effect the values due to the symmetry of the LPP and resultant blast waves. The He data is noisy and has less resolution because only one plane was taken where as the N_2 data shown is the average of 4 data planes. The temperature hot spots seen downstream of the blast wave front are from errors in the code fitting when a flat spectrum is analyzed.

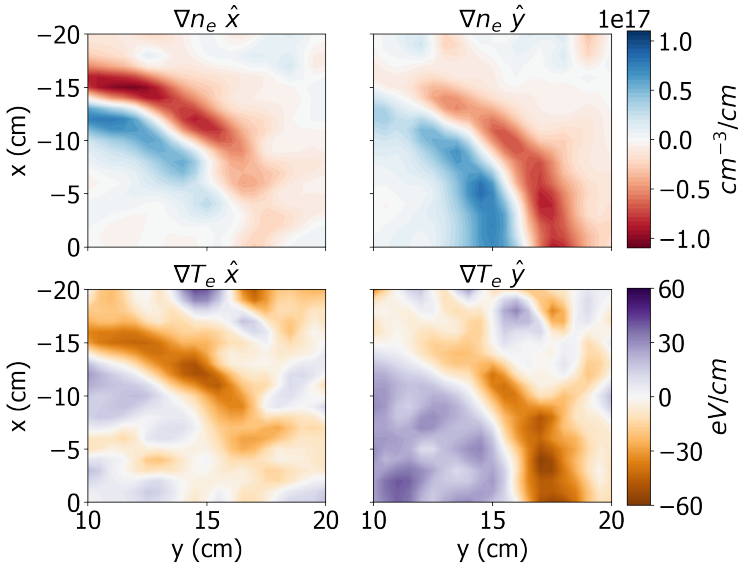

Figure 4.16: n_e and T_e gradients in 95 mTorr N_2 background gas corresponding to the 2D TS data presented in Figure 4.15. Top row: n_e gradients in $\hat{x}$ and $\hat{y}$ directions respectively. Bottom row: T_e gradients in $\hat{x}$ and $\hat{y}$ directions respectively.

central differences at the interior points of the data arrays and first-order one-sided differences at the boundaries of the data arrays. The electron temperature and density gradients were then used to calculate a theoretical value of the Biermann battery source term [74],

$$\frac{\partial \vec{B}}{\partial t} = \frac{c}{en_e}\vec{\nabla}T_e \times \vec{\nabla}n_e \ , \tag{4.3}$$

where c is the speed of light, and e is the elementary charge. A plot of $\partial B/\partial t$ computed from equation 4.3 overlaid with ∇T_e and ∇n_e vectors is shown in figure 4.17. The structure follows the shape of the shock wave, with the highest magnetic field values occurring just behind the shock front. The direction of $\partial B/\partial t$ is as expected from previous magnetic field measurements using the same experimental setup performed by Pilgram *et al*[74]. The $\partial B/\partial t$ was converted to a theoretical magnetic field value by multiplying it by the time it would take the blast wave to travel its width at $t = 100$ ns. This resulted in a value of $B \approx 300 - 500$ G.

The observation of non-parallel n_e and T_e gradients and the calculated $\partial B/\partial t$ via the Biermann battery effect confirm that high Mach number shock waves in plasmas generate

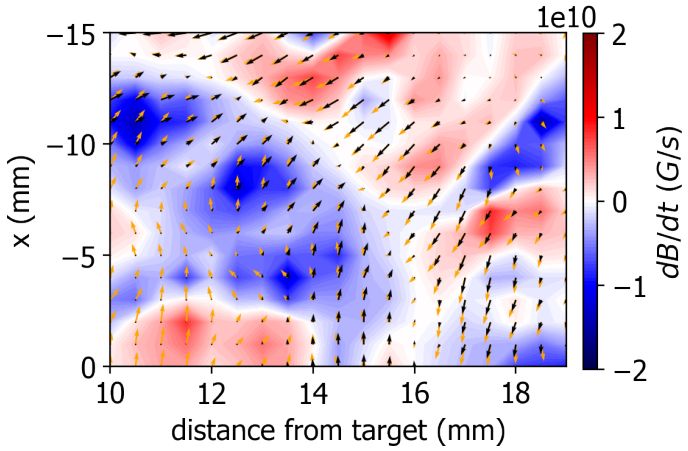

Figure 4.17: Calculated $\partial B/\partial t$ from electron temperature and density gradients for 95 mTorr of N_2. The black arrows are the ∇n_e vectors and the orange arrows are the ∇T_e vectors. The magnetic field values downstream of the shock front are most likely due to the non-physical temperature hot spots seen in Figure 4.3.2.

and amplify magnetic fields. The confirmation of these Biermann-generated fields under such conditions is relevant to the understanding of magnetic fields generated by high Mach number shocks in space, and how these magnetic fields may affect star formation, supernova remnant evolution, and mixing of the interstellar medium. This also supports the idea that the Biermann battery effect may indeed be a major source of protogalactic magnetic field generation.

4.4 Biermann Battery in Shock Fronts

Magnetic field measurements were taken in 95 mTorr of N_2 gas. In addition, we took measurements with a turbo pump and no gas filling to have a comparison to a vacuum case. The pressure for the vacuum measurements was 0.2 mTorr, any remaining gas contributing to the low pressure was air or water vapor. The experimental setup for these measurements, discussed in chapter 3, is the same as for the vacuum measurements, except that the b-dot probe was mounted with the shaft pointing along the blow-off axis and wired so that the

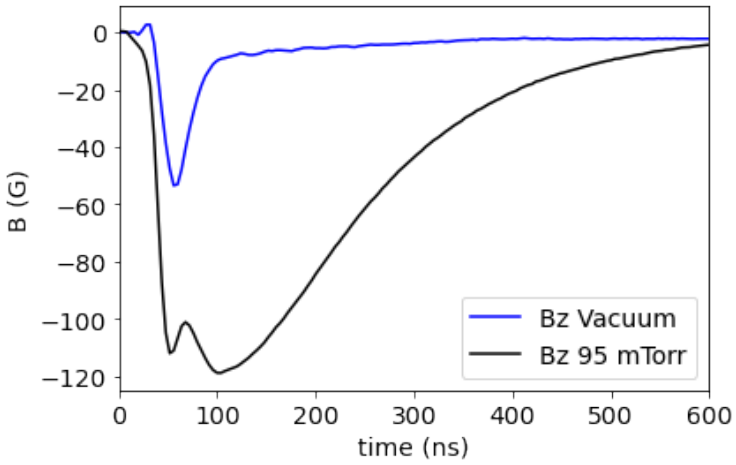

Figure 4.18: Comparison of a B-dot trace in Vacuum (blue) and 95 mTorr of N_2 gas (black) at (x,y,z) = (12,11,1) mm. There is a visible peak in the 95 mTorr trace which occurs at the same time as the peak in the vacuum signal. However, the 95 mTorr trace is much higher and has an additional wider peak with corresponds to the magnetic field by the blast wave front.

probe axes matched the chamber axes. The repositioning of the probe was done to reduce interference with the blast wavefront. Measurements were taken in the XZ, XY, and YZ planes to get an idea of the 3D structure of the blast waves and Biermann field generation.

A comparison between magnetic field traces in vacuum (0.2 mTorr) and 95 mTorr of N_2, shown in figure 4.18, shows a difference in both the magnitude and shape of the traces. Both traces show a spike that occurred around 50 ns, but is about twice as large in the blast wave case. This first spike is from the initial Biermann field generation, which occurs very close to the target surface. The second, larger spike, which is only present in the blast wave case, is thought to be additional Biermann field generation due to the temperature and density gradients in the blast wave front. The magnitude of the vacuum measurements is consistent with those from the first set of vacuum Biermann experiments, confirming that the earlier measurements were made in vacuum and only the TS measurements from that set of experiments had gas present.

The magnitudes of the magnetic fields measured in 95 mTorr N_2 and vacuum (0.2 mTorr)

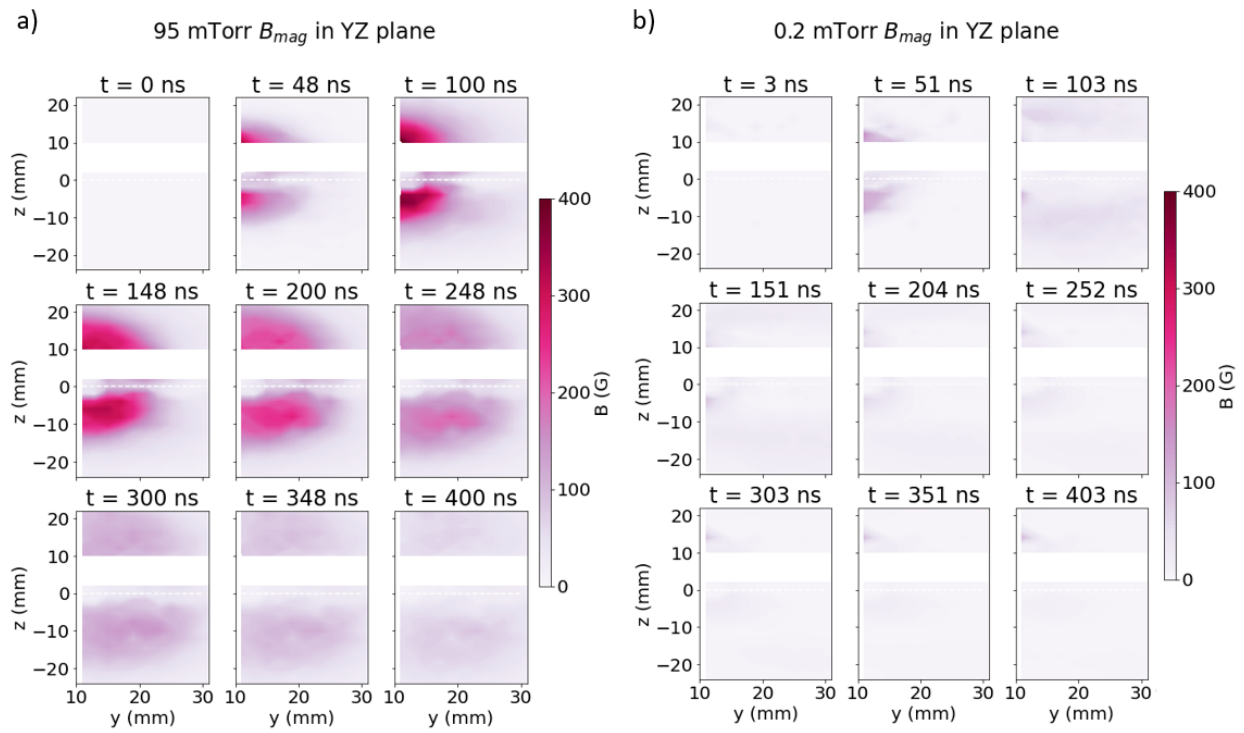

Figure 4.19: Contour plots of the magnitude of the magnetic field in an YZ plane at $x = 0$ mm for various times after heater beam fire. **a)** B_{mag} in the presence of a blast wave in 95 mTorr of N_2 gas. Peak fields of $B_mag = 400$ G were seen to occur between 100-150 ns. **b)** B_{mag} in vacuum (0.2 mTorr). Peak fields of $B_x = 100$ G were seen to occur around 50 ns.

in a YZ plane at $x = 0$ mm are shown in figure 4.19. The peak magnitude of the fields in the presence of a Sedov-Taylor blast wave reached a value of $B_{mag} = 400$ G. This was only 40 G higher than the x-component of the magnetic field in this plane (shown in Appendix B, Figure B.5), indicating that the primary direction of the magnetic fields in this plane is in the ±x-directions. The fields in the presence of blast waves are stronger than in a vacuum environment by a factor of 6. The fields and their structure also persist for a much longer time after the blast wave front than fields in a vacuum where no blast wave is formed.

The directionality of the fields in the presence of blast waves at 95 mTorr of N_2 and in a vacuum environment is consistent in all planes. An example of this can be seen in figure 4.20. Note that the XZ plane was taken at $y = 11$ mm from the target surface, while the YZ plane

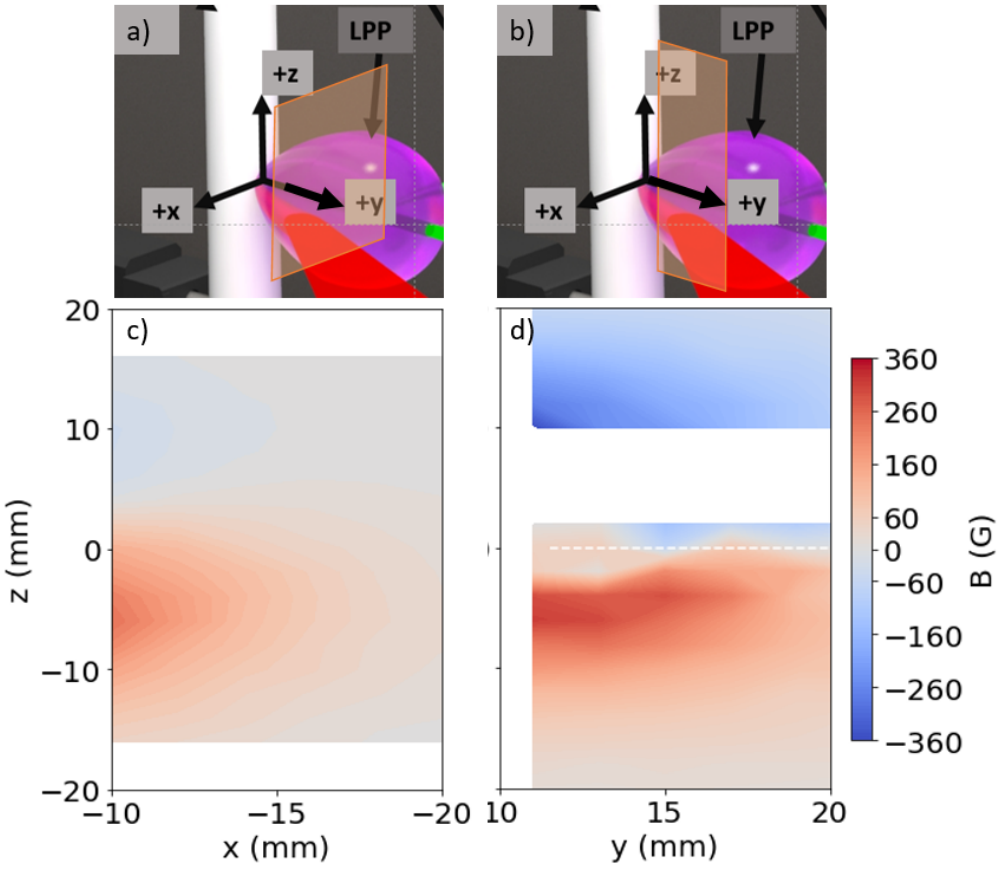

Figure 4.20: B_x component of magnetic field measurements at t=100 ns in XZ and YZ planes. Red represents fields coming out of the page and blue represents fields going into the page. **a)** Depiction showing the orientation of an XZ plane. **b)** Depiction showing the orientation of a YZ plane. **c)** B_x in an XZ plane at $y = 11$ mm, peak values reach $B_x = 300$ G. **d)** B_x in an XY plane at $x = 0$ mm, peak values reach $B_x = 360$ G. Note that the values of the magnetic fields in the XZ plane are weaker than in the YZ plane because they were taken 11 mm further from the heater beam spot.

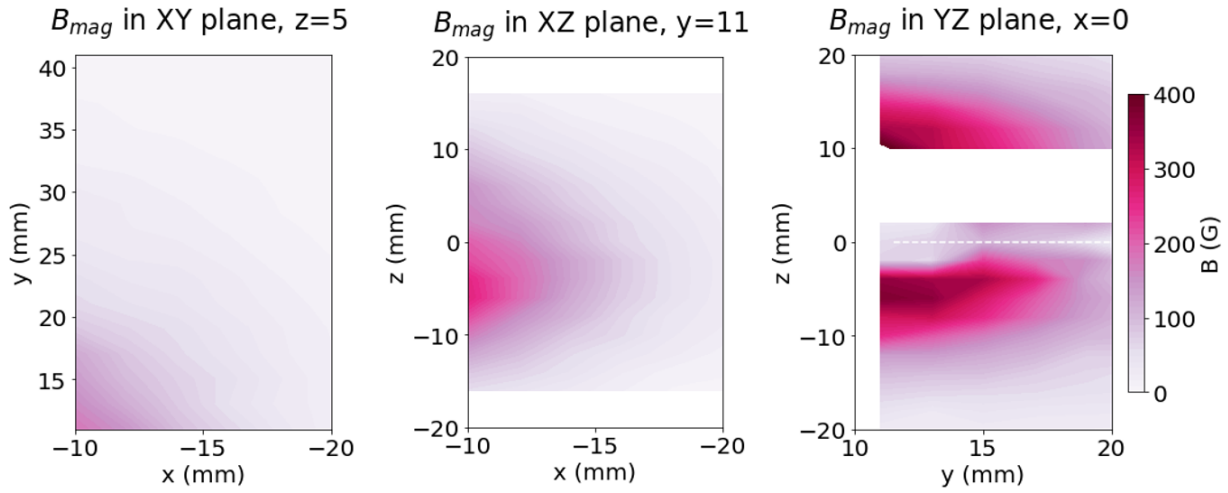

Figure 4.21: Magnetic field magnitude at t=100 ns after heater beam fire. **Left:** B_{mag} in an XY plane at z = 5 mm. Peak values reach $B_{mag} = 180$ G. **Middle:** B_{mag} in an XZ plane at y = 11 mm. Peak values reach $B_{mag} = 300$ G. **Right:** B_{mag} in an YZ plane at x = 0 mm. Peak values reach $B_{mag} = 400$ G.

was taken at $x = 0$ mm and has a hole in the middle, both due to proximity to the heater beam path. Due to the difference in position from the target surface, the magnitude and position of the fields in the YZ plane are slightly larger. Despite the difference in position of the measurements, the general structure and direction of the fields match, confirming that the fields generated in the presence of blast waves are symmetrical and that data from any plane can be compared to the 2D TS data. In a vacuum environment, the fields were always measured to be much weaker, to peak earlier, and to dissipate more quickly. This confirms that laser-driven shock waves increase the strength of the magnetic field in a plasma.

A comparison between the XY, XZ and YZ planes at t=100 ns after the heater beam fire is shown in figure 4.21. Note that each plane is taken at a different distance from the target surface due to its proximity to the heater beam path. The YZ plane was taken closest to the heater beam spot, on an axis above and below the laser path. This plane contains the highest measured fields, up to 400 G, occupying the largest spatial region. This is due to the fact

that the shock wave, and thus the fields, travel the shortest distance before detection. The XZ plane has a similar structure to the YZ plane and was recorded with similar coordinates as the YZ plane, but was measured at y=11 mm as opposed to x=0 mm of the YZ plane. The XZ plane had a peak magnitude of 260 G, which is reasonable compared to the 400 G in the YZ due to the 11 mm distance from the target surface. The XY plane had an inadvertent offset from the Z axis of z=5 mm, so the slice of the blast wave magnetic fields measured did not contain the full picture of what occurred along that axis. The fields measured in this plane only reached a peak of 180 G, which is much lower than the other planes, but due to the offset in z this is not a completely unreasonable value. In all planes it was found that the magnitude of the magnetic field measurements in the presence of blast waves was at least 100 G greater than those obtained in a vacuum environment, further confirming that blast waves lead to much higher magnetic field values. Additional data for vacuum and 95 mTorr N_2 in all planes are shown in the appendix B.

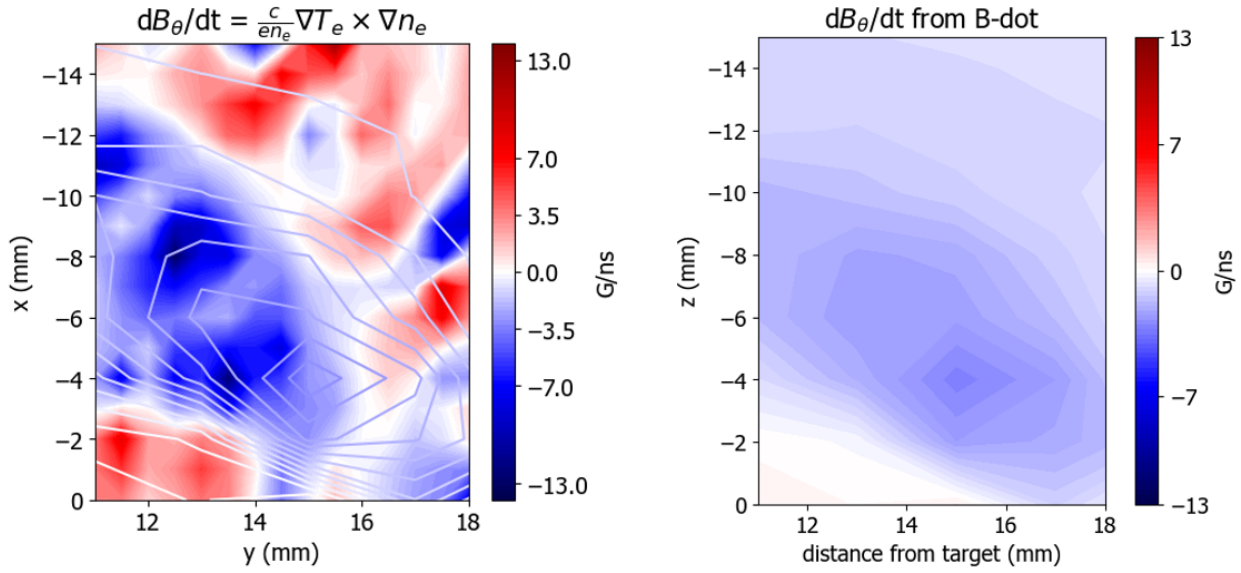

Figure 4.22: Comparison between TS dB/dt and B-dot dB/dt. **Left**: dB/dt calculated from the TS T_e and n_e gradient measurements (solid contour). The contour lines from the B-dot dB/dt are overlaid to highlight the similarity in shape. **Right:** dB/dt as measured by the B-dot probe at t=100 ns which corresponds to the time of the TS measurements.

A comparison between the calculated dB/dt from the TS gradients T_e and n_e and the dB/dt measured by the B-dot probe is shown in figure 4.22. The dB/dt from the B-dot measurements were obtained by correcting the measured signals for attenuation, gain, offset, and calibration factors, but not by integrating over time. The plot on the left of figure 4.22 shows the calculated TS dB/dt as a solid contour and is overlaid with the contour lines of the B-dot dB/dt.

Comparing the solid contours, it can be seen that the dB/dt from the B-bot is about a factor of 2 lower than the dB/dt calculated from the TS gradients. One source of the discrepancies is the low resolution of the 3 mm B-dot probe measurements, much larger than the TS resolution (0.5 mm), causing the measured dB/dt to be artificially smoothed over the region. Machine learning efforts are currently underway to improve the data analysis of the TS measurements, which will provide insight into the observed hot spots in the data. In addition, future experiments are planning the use of a 1 mm, 3-axis B-dot probe to obtain higher resolution magnetic field measurements.

4.5 Comparison to FLASH simulations

For a closer look into the physics of the Biermann process, a series of simulations using the FLASH code [28] have been employed. FLASH is a parallel, multi-physics, adaptive-mesh-refinement, finite-volume Eulerian hydrodynamics and magnetohydrodynamics (MHD)[53] code, whose high energy density physics capabilities[95] have been validated through benchmarks and code-to-code comparisons [27, 72], as well as through direct application to laser-driven laboratory experiments[63, 64, 56, 97, 12, 7].

4.5.1 Vacuum data comparison to FLASH simulations

The first suite of simulations was conduced to compare to the vacuum Biermann experiments. The two-dimensional Cartesian simulation is initialized from a "top-down"-perspective of the experimental configuration shown in Fig. 3.1a. The simulation domain is illustrated in

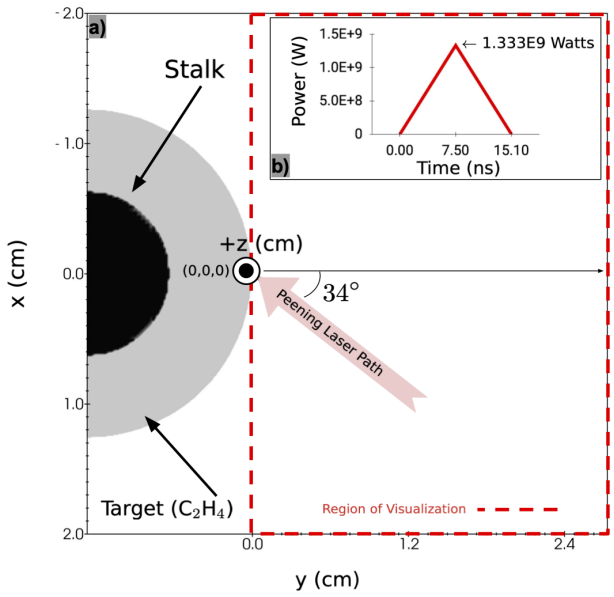

Figure 4.23: **a)** Visualization of the two-dimensional simulation domain for the xy-plane, i.e., $z = 0$, at $t = 0$ for the laser-facing side of the target. The black semi-circle region denotes the rod which supports the target material (grey). The Peening laser beam enters the simulation domain at a 34° angle from the $+\hat{y}$-direction for positive values of $\hat{x}$, reflecting the geometry of the experimental setup provided in Fig. 3.1a. The region visualized in the provided simulation results (Figs. 4.24 & 4.25) is enclosed by the dashed red line. **b)** The power profile used to model the Peening laser heater beam in FLASH with a peak of 1.333×10^9 W at 7.5 ns, which allows 10 J of energy to be deposited to the target over 15 ns as in the experiment.

Fig. 4.23a, modeling the x-y plane (i.e., $z = 0$) of the experiment. At room temperature and pressure, we initialize a cylindrical rod of C_2H_4 plastic. The equation of state and opacity material tables for C_2H_4 are computed using PrOpacEOS[1]. The rod initial mass density is $\rho = 1.047$ g/cc. We approximate the temporal profile of the laser pulse using a triangular profile, 15 ns long, with a peak power of approximately 1.33×10^9 W at 7.5 ns, as shown in Fig. 4.23b. This drive profile emulates the 10 J Peening laser drive used in collecting the magnetic field data. The laser enters from the $+\hat{x}$-direction of the simulation domain at 34 degrees with respect to the y-axis, to accurately capture the incidence angle of the experimental drive.

In our finite-volume, single-fluid Eulerian simulations, the vacuum surrounding the rod must be modeled using a low density gas. In order to image only the plasma expanding from the target rod, in Figs. 4.24 & 4.25 we applied two threshold filters to visualize only the LPP properties against a white background. First, we exclude from the visualization cells containing a mass fraction less than 95% of the rod material. Then, we exclude cells whose effective ionization $\bar{Z}$ is affected by heat flux from the compressed low-density gas material at neighboring cells. These thresholds exclude cells compromised by the presence of the low density gas from being folded into post-processing calculations. Similarly, magnetic field generation due to Biermann battery is only computed in smooth-flow regions of the LPP to ensure resolution-convergent magnetic field values[26].

We feature two simulation configurations that aim to determine (1) whether the magnetic fields measured experimentally are consistent with Biermann battery generated magnetic fields, and (2), if so, to quantify the contribution of Biermann battery magnetic field generation in the expanding LPP versus the Biermann battery magnetic fields generated due to the laser-target interaction, which are subsequently advected by the expanding plasma.

In the first simulation, we retain the Biermann battery source term in the induction equation operating throughout the entire simulation duration (i.e., "Full Biermann battery" or FBB). In the second simulation, we artificially switch off the Biermann battery source term

[1]More info on PrOpacEOS: `https://www.prism-cs.com/Software/Propaceos/overview.html`

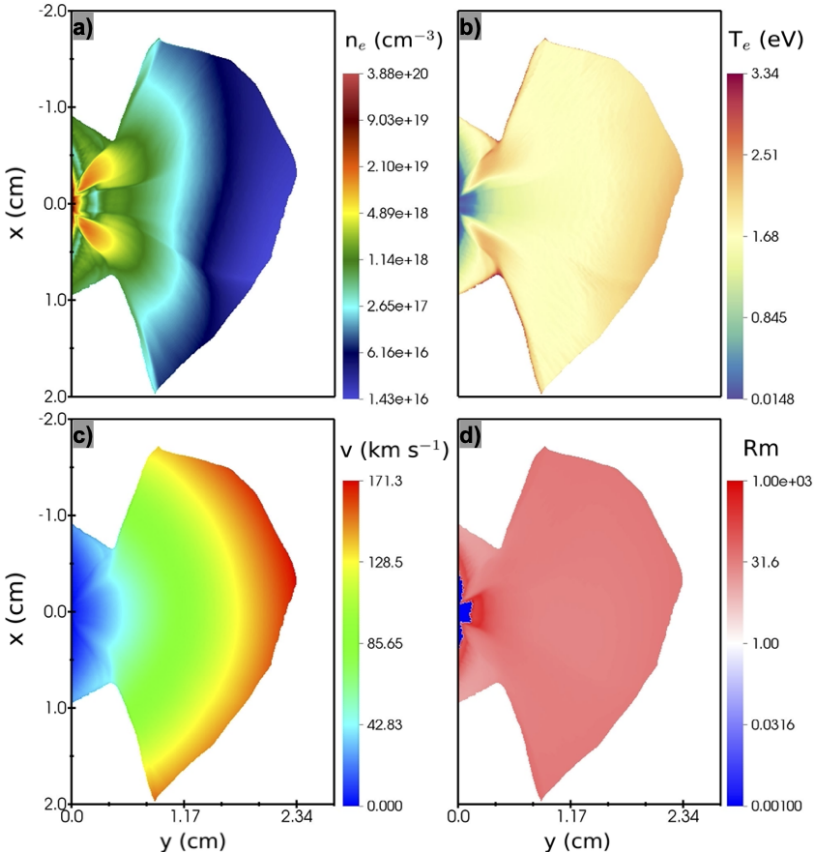

Figure 4.24: Visualization of the FBB 2D FLASH simulation for **a)** the electron number density n_e, **b)** the electron temperature T_e **c)** the magnitude of the velocity, and **d)** the magnetic Reynolds number at 150 ns after the laser fires. We describe the threshold applied to these visualizations in the text.

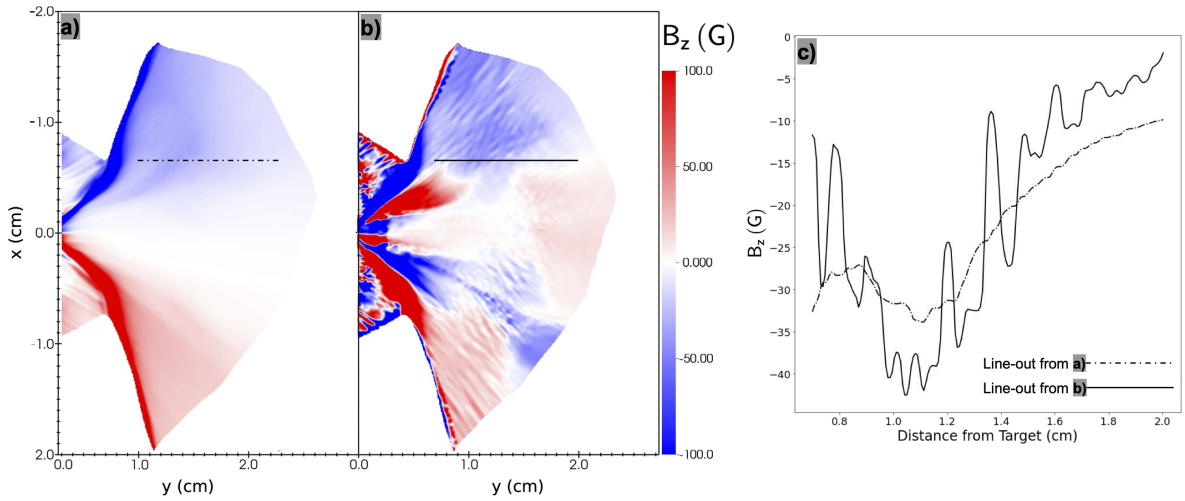

Figure 4.25: A visualization of the magnetic field values within the LPP region 150 ns after laser fire. **a)** results from a simulation where the Biermann battery source term was calculated only during the 15 ns duration of the laser (LOBB case), and **b)** results where the Biermann battery source term was calculated for the entire simulation duration of 400 ns (FBB case). Provided in **c)** are line-outs from a) LOBB and b) FBB simulations taken at $x = -0.7$ cm and $y = [0.7, 2.0]$ cm away from the target.

as soon as the laser pulse ends (i.e., "Laser Only Biermann battery" or LOBB). The plasma properties of the "realistic" FBB case are reported in Fig. 4.24, whereas the resulting magnetic field profiles for both FBB and LOBB simulations are shown in Fig. 4.25. In Fig. 4.24 we report the plasma properties of the LPP predicted by the FLASH FBB simulation. At the region of interest (i.e., the locus of the Thomson scattering measurements), we find electron number densities on the order of 6×10^{16} cm^{-3} (Fig. 4.24a) that match well with experimentally obtained values discussed in section IV. However, since the FLASH simulations have not yet been calibrated against the experimental results, we find that the simulation under-predicts the plasma electron temperatures and velocities (as shown in Fig. 4.24b,c), and is consistent with the experimental measurements only within a factor of unity. More specifically, the LPP expansion velocity in the FBB FLASH simulations is approximately 115-125 km s^{-1} on average with a peak value of around 170 km s^{-1}, when the plasma velocity is estimated to be 330 km s^{-1} in experiment. Consistent with the experimental results, we find that the LPP has magnetic Reynolds numbers Rm $\gg 1$ (Fig. 4.24d), indicating that the magnetic field advection dominates resistive diffusion.

We note the emergence of two plasma lobes near the locus of the laser drive, which are prominently seen in the visualizations of the electron density and temperature (Fig. 4.24a,b). The two lobes surrounding the laser-target spot at the origin and the overall asymmetry of the LPP are caused by the asymmetry of the laser drive via the non-normal incidence angle. One may orient themselves conceptually by considering the bottom most density lobe ($+y$-direction) on the laser-facing side of Fig. 4.24a. This ejection has expanded more quickly in comparison to its data-collection side ($-y$-direction) sibling, as hot, dense material from the target has filled the comparably low density pseudo-vacuum bore from the simulated laser. These density and temperature gradients cause the generation of Biermann battery magnetic fields, and begin nanoseconds after the laser illuminates the target. This is seen in both LOBB and FBB cases (panels a) and b) in Fig. 4.25, respectively). The two lobes surrounding the laser-target interaction region have the strongest gradients, and thus the strongest magnetic fields values in the computational domain.

Major points of comparison between panels a) and b) of Fig. 4.25 and the two resulting line-outs, taken at $x = -0.7$ cm to match the location of the experimental B-dot probe (Fig. 4.25c), are the magnitude and structure (viz., spatial variability) of the Biermann battery magnetic fields. First, the values of the magnetic fields within the simulated LPP region are consistent and within range of the experimentally-measured values (Fig. 4.1a), and are of the same direction. This observation further supports the conclusion that the experimentally-observed magnetic fields originate from the Biermann battery mechanism. Second, the magnetic fields featured in Fig. 4.25a for the LOBB FLASH simulation are smooth when compared to those obtained in the FBB FLASH simulation (Fig. 4.25b) and the experimentally-obtained magnetic field profiles (Fig. 4.1a). By maintaining the Biermann battery source term active for the entirety of the simulation, the resulting magnetic fields manifest increased variability in both large (Fig. 4.25b) and small spatial scales (Fig. 4.25c). These large-scale spatial gradients of the Biermann battery magnetic fields can therefore naturally account for the current structures seen in Figure 4.1b, thus indicating that the Biermann battery mechanism in the experiment is active inside the LPP, even after the laser has fired. These small-scale structures in Fig. 4.25b, seen also in the oscillations present in the solid line of Fig. 4.25c are the result of spatial variations in the misalignment of electron temperature and density gradients, which result in continuous Biermann battery magnetic field generation, in contrast to Fig. 4.25a. Kinetic magnetic field generation effects such as the Weibel instability cannot be modeled in FLASH, which is an Eulerian finite-volume MHD code with isotropic pressure.

Comparing our experimental parameters to simulations revealed a disparity between measured and simulated values of electron temperature and density. Adams conducted additional simulations that introduced the presence of background gases at varying pressures to further investigate the issue. It was observed that even a small amount of background gas could produce blast waves from the LPP, affecting electron temperature and density, and increasing the magnitude of the Biermann generated fields. Simulations matched experimental results T_e and n_e values when a background gas was introduced into the system. It was concluded

that blast waves were likely forming during the TS measurements, causing higher values for both T_e and n_e. These simulations motivated us to examine Biermann generated fields in the presence of background gases. Biermann generated fields are dependent on the electron temperature and density gradients in the system which would be amplified in hydrodynamic shock waves thus, creating larger fields.

4.5.2 3D FLASH simulations in the presence of Shock waves

Preliminary 3D FLASH simulations were performed for comparison with the shock wave measurements. The simulations were initialized using a similar setup as described in the 4.5.1 section, but extended to 3D and with the addition of 95 mTorr of N_2 background gas. The simulations were run under two conditions. The first simulation was run with all terms of the induction equation active at all times, including the Biermann battery term, which we will refer to as Biermann on or full Biermann battery (FBB). The second simulation was run under the same conditions, but with the Biermann battery term active only during the heater beam fire, we will refer to this case as Biermann off or laser on Biermann battery (LOBB). The comparison between the simulations and the experiments shows that the uncalibrated preliminary 3D simulations are in general agreement with the experimental results. A detailed comparison between experiments and simulations is presented below.

A comparison of the shock velocity in the simulations and experiments is shown in figure 4.26. It can be seen that the general shape of the measured shock waves and the simulated shock waves match, since they are both Sedov-Taylor shock waves. However, the speed of the shock waves in the simulations is slightly higher than that measured experimentally. We also compared the calculated Mach number in the experiments and the Mach number in the simulations. From the simulations, we obtained a $M = 50$ at t=100 ns where as in the experiments we calculated $M = 158$. This discrepancy is due to the fact that the experimentally calculated assuming the background gasses were at room temperature where as in the simulations, heating of the background gas due to the heater beam was observed. The increased temperature in the simulations would lead to a higher sound speed in the

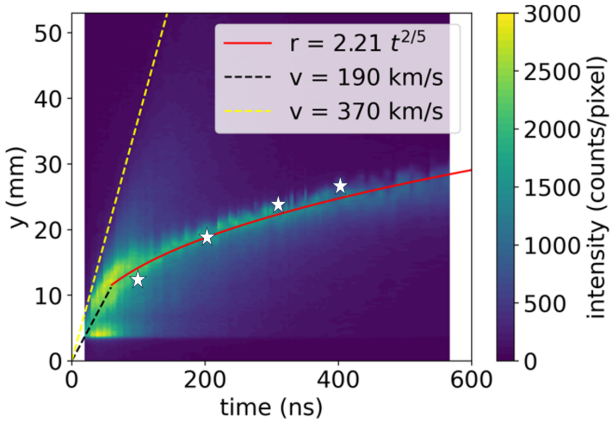

Figure 4.26: Comparison of shock wave propagation speed of a streak plot in 95 mTorr of N_2 background gas (solid contour) and FLASH simulations (white stars).

background gas and thus a higher M. Despite these small discrepancies, the dynamics seen in the simulations are very similar to what was observed experimentally.

A comparison of the experimentally measured and simulated n_e and T_e at t =100 ns after laser fire for a lineout along the blow-off axis is shown in figure 4.27. Both the Biermann on and Biermann off cases are shown. It was found that in both cases the n_e and T_e were the same as expected. The position of the shock waves in simulations are behind those seen in experiments by a few mm which is consistent with what was seen in the speed comparison in figure 4.26. The the experimentally measured quantities are also slightly wider than the simulated ones. The magnitude of T_e for both simulations and experiments is in very good agreement, with both peaking around T_e = 20 eV along this lineout. However, the n_e values do not show such agreement. We experimentally measured an electron density of $n_e = 2{\times}10^{16}\ cm^{-3}$, while the simulations show a value of $n_e = (8{-}15){\times}10^{16}\ cm^{-3}$, which is 4-7.5 times larger. The main cause of this discrepancy is that preliminary simulations shown are not yet calibrated and the laser drive needs to be adjusted to better match the experimental values. With the current laser drive, the simulation shocks have not yet expanded to where the experimental data was taken therefore the density is higher because the shock has not expanded sufficiently. Work on this front is currently in progress. 2D contours of n_e, T_e, n_i and T_i from the Biermann on FLASH simulations are shown in figure 4.28. It can be seen

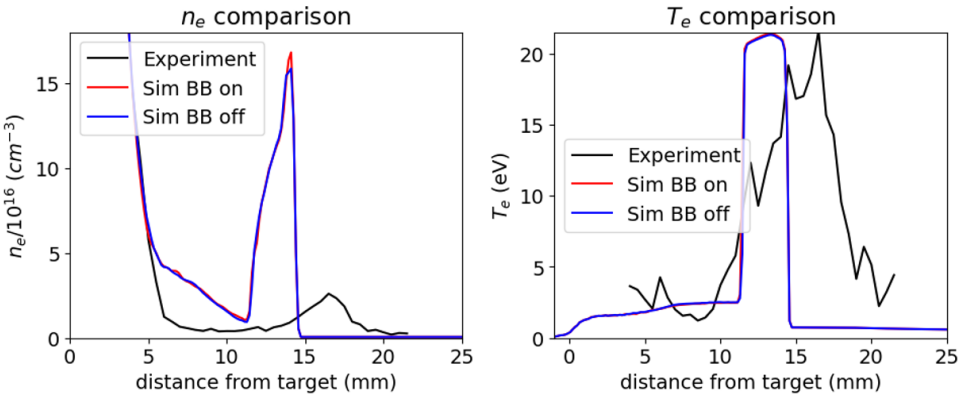

Figure 4.27: Comparison of experiment and FLASH simulation n_e and T_e at t=100 ns after hear beam fire. **Left:** Comparison between experimental n_e (black) and FLASH simulation n_e with Biermann on (red) and Biermann off (blue). **Right:** Comparison between experimental n_e (black) and FLASH simulation T_e with Biermann on (red) and Biermann off (blue).

that although the maximum values for n_e do not agree with the measured values, the shock waves formed generally agree with the shape and position observed experimentally from our 2D TS measurements in figure 4.15.

Although the simulations do not exactly match the experimental measurements, they can still help us to understand the physics occurring in our experiments. A 2D comparison between the Biermann on and Biermann off simulation cases is shown in figure 4.29. It can be seen that the position and shape of the shock waves is similar to experiments in both cases, but the magnitude of the magnetic field is much higher in the Biermann on case. Lineouts along the blow-off axis of the magnitude of the magnetic fields in the Biermann on and Biermann off cases are shown in figure 4.30 for a clearer comparison. In the Biermann off case, the magnetic field peaks at the shock wave front with a value of $B_{mag} = 1010$ G. Whereas in the Biermann on case, the magnetic field peaks just before the shock front with a value of $B_{mag} = 4700$ G and has an additional small peak at the shock front of $B_{mag} = 1620$ G. With the Biermann on case, we see a peak magnetic field about 5$\times$ higher

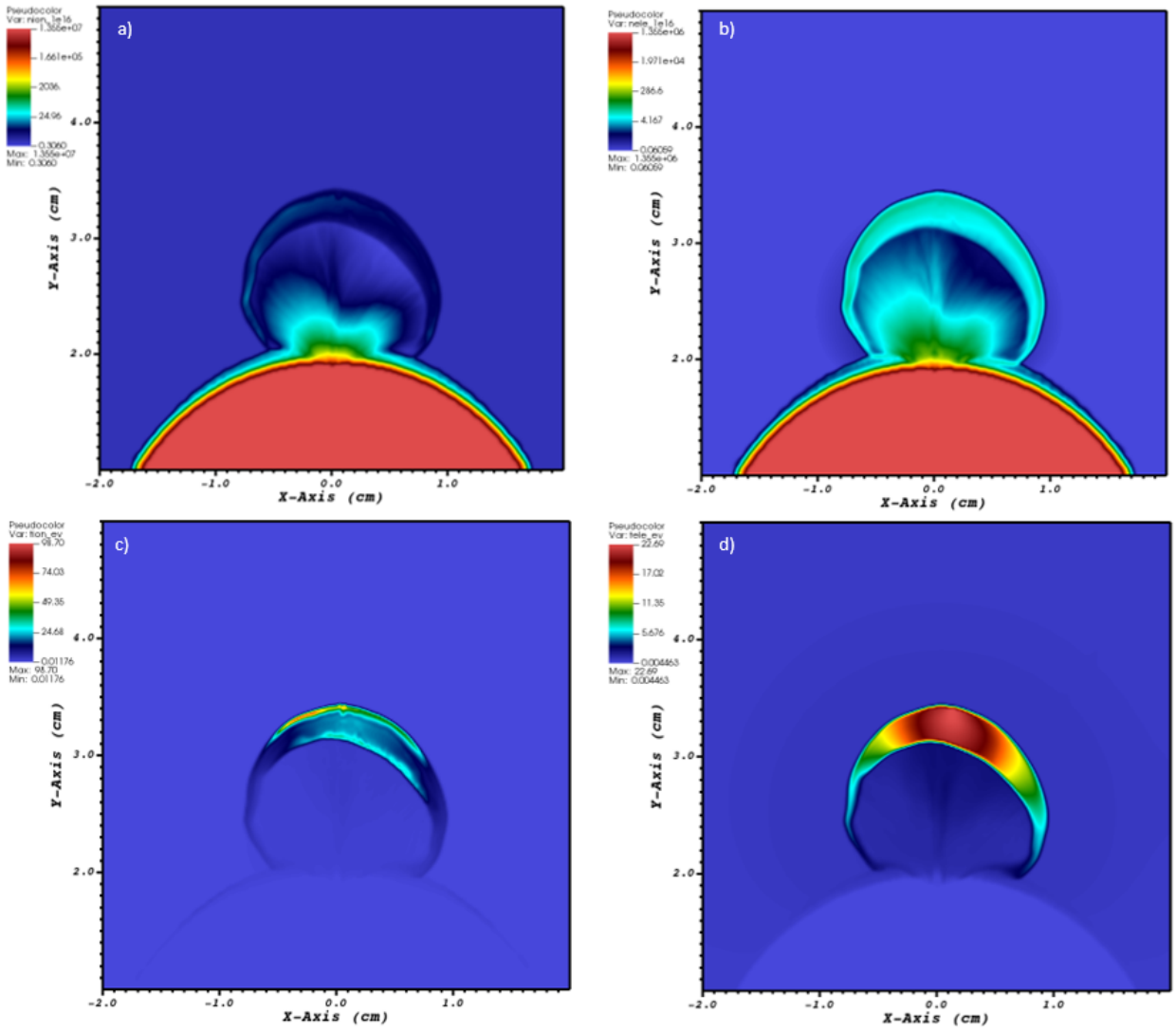

Figure 4.28: 2D contours of electron and ion temperature from FLASH simulations at t=100 ns after heater beam fire. All values were similar in both Biermann on and off cases so only the Biermann on case is shown here **a)** n_i from FLASH simulations reaching a peak value of $n_i = 8 \times 10^{16}\ cm^{-3}$ in the shock wave front. **b)** n_e from FLASH simulations with a values in the shock wave of $n_e = (8-16) \times 10^{16}\ cm^{-3}$. **c)** T_i from FLASH simulations reaching a peak value of $T_i = 63$ eV in the blast wave front. **d)** T_e from FLASH simulations reaching a peak value of $T_e = 21.5$ eV.

than in the Biermann off case. This is consistent with the experimentally measured difference between the vacuum and shock-wave cases, with fields 6× higher in the shock-wave case. The simulations, however, have much a higher resolution than what can be measured in the lab. The peaks that we see in the simulations could not be resolved by our probes and are smoothed out in measurements, leading to lower and wider experimental peak values. By taking a full width half max of the simulation peaks we get a much more comparable value to the experimental measurements. For the Biermann on case, we see a peak near the shock wave front of about $B = 500$ G where as for the Biermann off case we only see a value of around $B = 250$ G. The fields from the Biermann on simulations both show a peak of magnetic field generation behind the shock front and have similar magnetic field values to what was seen in experiments. The Biermann on simulation magnetic field values are bit higher than what was measured in the lab but this is expected as the density in the simulations at this time is higher than what was experimentally measured. From these similarities between the Biermann on simulations and our experiments, we conclude that the main source of the higher magnetic fields in the presence of shock waves is magnetic field generation by the Biermann battery effect.

The preliminary 3D FLASH simulations produced shock waves that propagate at a similar speed and have a similar structure to our experiments. A comparison of experimental and simulation parameters at t=100 ns after heater beam fire are shown in table 4.1. We see that the values at this time in the shock front agree within an order of unity for all quantities except n_e. The higher magnetic field seen in figures 4.29 and 4.30 can easily be explained by the higher n_e. If n_e is larger, then ∇n_e will naturally be higher, leading to higher Biermann generated fields. Even with these discrepancies, the ratio between Biermann on and Biermann of magnetic fields is consistent with the ratio between magnetic fields measured in shock wave and vacuum cases. This suggests that the majority of the magnetic fields measured in the presence of hydrodynamic shock waves are due to magnetic field generation by the Biermann battery effect. Work is currently in progress to calibrate the simulations and address the discrepancies we see between the FLASH simulations and experimental values.

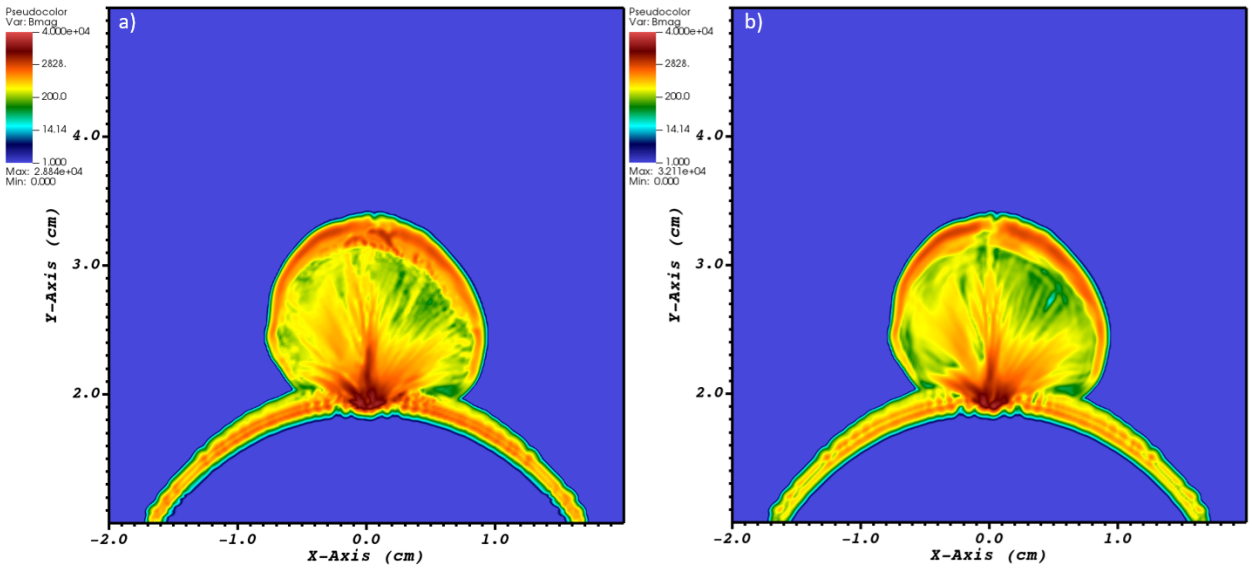

Figure 4.29: 2D contours of B_{mag} from FLASH simulations with Biermann on and off at t=100 ns after heater beam fire. **a)** Contour of B_{mag} in the Biermann on case. The magnetic fields reach a peak value of $B_{mag} = 4700$ G. **b)** Contour of B_{mag} in the Biermann off case. The magnetic fields reach a peak value of $B_{mag} = 1010$ G.

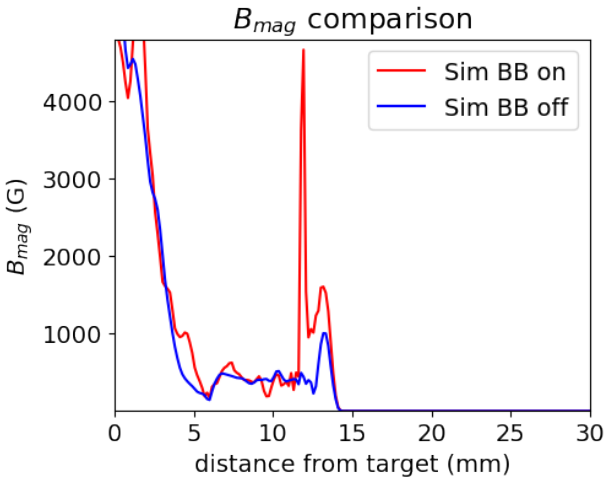

Figure 4.30: Comparison between B_{mag} from FLASH simulations in both Biermann on (red) and Biermann off (blue) simulations at t=100 ns after heater beam fire. For the Biermann on case, the magnetic fields reach a peak value of $B_{mag} = 4700$ G just behind the shock wave front. For the Biermann off case, magnetic fields reach a peak value of $B_{mag} = 1010$ G in the shock wave front.

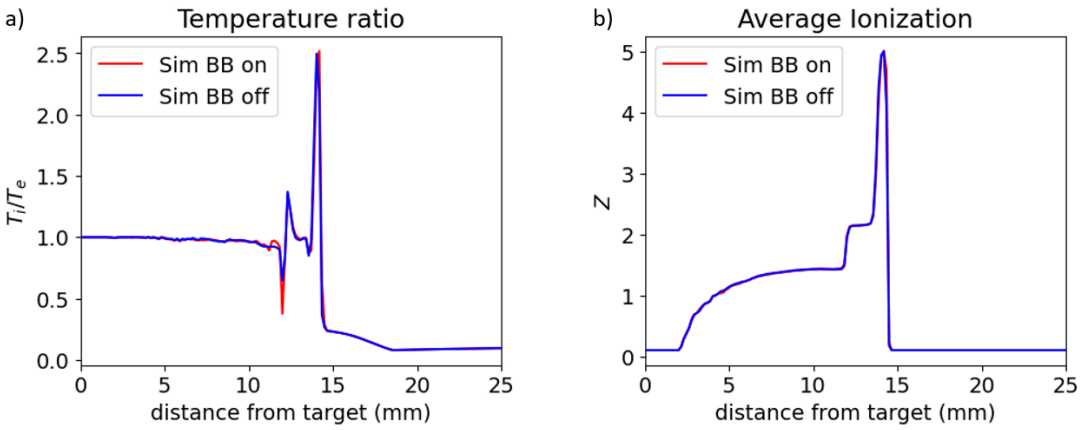

Figure 4.31: Parameters from FLASH simulations used to calculate n_i and T_i. **a)** Ratio of T_i/T_e vs distance from the target along the blow off axis. **b)** Average ionization vs distance from the target along the blow off axis.

4.6 Relevance to Astrophysics

The Reynolds number, magnetic Reynolds number and magnetic Prandtl number were calculated for our experiments at t=100 ns, using extrapolated values from the FLASH simulations for the ion temperature and density (not measured in our experiments). T_i was calculated using the formula $T_i = 2.4T_e$, which correlates with the peak T_i/T_e in Figure 4.31, and n_i was calculated using $n_i = n_e/\bar{Z}$, using the peak value of $\bar{Z} = 5$ from Figure 4.31, where $\bar{Z}$ is the average ionization. Values of various plasma properties from experiments, simulations, and selected astrophysical systems can be found in the table 4.1.

The values for R_e and R_m were calculated using the 2D TS data discussed in section 4.3.2. Contour plots of these values are shown in figure 4.32. Both R_e and R_m are higher in the shock front than the plasma upstream and the unshocked gas downstream. Even so, R_e and R_m are both much larger than unity upstream and downstream of the shock front. The peak values in the shock front were determined to be $R_e = 1.5 \times 10^3$ and $R_m = 77.5$. These peak values were used to calculate a Prandtl number of $P_m = 5.17 \times 10^{-2}$.

Interpreting these numbers, we find that the Reynolds number was much greater than one,

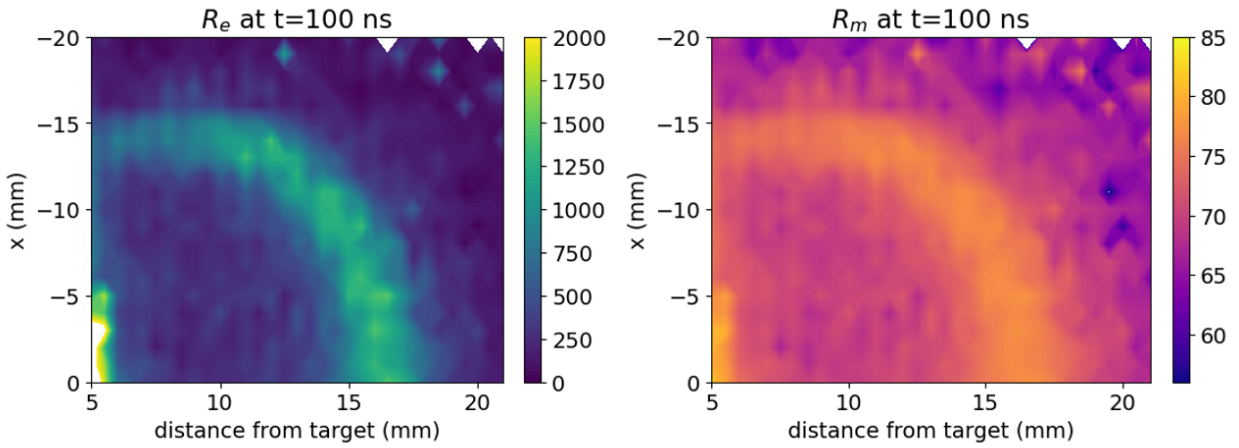

Figure 4.32: Contour plots of R_e and R_m calculated using 2D TS data. **Left:** Contour of R_e at t=100 ns after laser fire with a peak value in the shock front of $R_e = 1.15 \times 10^5$ **Right:** Contour of R_m at t=100 ns after laser fire with a peak value in the shock front of $R_m = 77.5$

which indicates a turbulent regime for the plasma flow, fact supported by our experimental observations in the self-emission images (see Figure 4.5). The magnetic Reynolds number was also much larger than unity, indicating that magnetic fields in the system, once generated, were advected with the plasma flow. The R_m values from the blast wave case also agree with those determined for the vacuum experiments discussed in section 4.1. The magnetic Prandtl number, on the other hand, was much smaller than unity, indicating that magnetic diffusion dominated over viscous diffusion.

Values from simulations of strong shocks from supernova remnants (SNR) through the interstellar medium (ISM) by Inoue et al. [46] are given in the SNR column of the table 4.1. In these simulations, the shock strength corresponded to the Sedov-Taylor phase of an SNR with a velocity of about 10^3 km/s, a Mach number of M=170, and $R_m < 100$. R_e for these simulations was not reported. However, similar simulations of an SNR expanding into the ISM by Stone et al. [93] with M=10 shocks report $R_e \geq 10^3$, so we assume that the Inoue simulations have R_e in a similar range. These values are similar to our experimental conditions, so our experimental results may be relevant to the dynamics occurring in SNR shocks.

Plasma property	Experiment	FLASH	SNR	Stellar Atm	Warm ISM
n_e (cm^{-3})	2×10^{16}	$(8-15) \times 10^{16}$	-	-	-
T_e (eV)	25	$20-22$	-	-	-
n_i (cm^{-3})	-	$(1-2) \times 10^{16}$	2	10^{15}	1
T_i (eV)	-	$35-65$	-	-	-
T (eV)	-	-	-	0.8	0.8
L (cm)	1.5	1.5	1.5×10^{17}	10^9	3×10^{18}
v ($cm\ s^-1$)	5.6×10^6	10^7	1×10^8	10^7	10^7
B (G)	4×10^2	5×10^2	10^{-3}	10^2	10^{-5}
M	158	50	170	10	10
$R_m = \frac{vL}{\eta}$	77	150	< 100	4×10^9	10^{19}
$R_e = \frac{vL}{\mu}$	1.5×10^3	3.0×10^3	$\geq 10^3$	5×10^{12}	10^8
$P_m = \frac{R_m}{R_e}$	5×10^{-2}	5×10^{-2}	$\leq 10^{-2}$	8×10^{-4}	10^{12}

Table 4.1: Table comparing experimental and simulated plasma quantities to astrophysical systems. Formulas are fully defined in section 2.4. All values for SNR simulations except R_e are from Inoue et al.[46]. R_e for SNR simulations is from Stone et al[93]. Values for Warm ISM and Stellar Atmosphere from J. I. Castor[11]

Another astrophysical system with similar parameters is stellar atmospheres. Like our experiments, stellar atmospheres have $R_m >> 1$, $R_e >> 1$, and $P_m << 1$ (column Stellar Atm, table 4.1). Based on this, the plasma and magnetic field flow conditions in our experiments should behave similarly to those in stellar atmospheres. Therefore, the physics studied in the discussed experiments may be relevant to the dynamics and shocks that occur in stellar atmospheres.

In addition, our experiments may be relevant to primordial and protogalactic magnetic field generation. The experiments presented in this paper were performed under similar conditions and have similar values of R_m and R_e as the experiments performed by Gregori

et al. [36]. However, our experiments were performed in much higher spatial detail, achieved higher magnetic field values, and obtained measurements of ∇T_e and ∇n_e. Gregori claimed that their experiments were relevant to primordial magnetic field generation, and scaling of their measured fields revealed seed fields on the order of 10^{-21} G[36]. Since both experimental systems have similar dimensionless parameters, the investigated systems behaved similarly. Therefore, the results of my experiments further support the theory that the Biermann battery effect could have generated seed magnetic fields in the early universe at values of $\geq 10^{-21}$ G. Fields of this strength could then have been amplified by turbulent and dynamo effects to the values we see in the universe today.

CHAPTER 5

Conclusions

Experiments were performed to study the Biermann battery effect in vacuum and in the presence of hydrodynamic shock waves. In the vacuum case, the fields were found to be azimuthally symmetric with strengths up to 60 G at a distance of 7 mm from the target surface. Thomson scattering measurements for these experiments recorded $n_e = 5.55 \times 10^{16} cm^{-3}$ and $T_e = 10$ eV. Simulations for the vacuum experiments were performed by M.B.P. Adams, who found that background gas may have been present during the Thomson scattering data collection, causing shock waves to form. This discrepancy inspired further investigation of Biermann generated magnetic fields due to hydrodynamic shock waves.

Laser-driven blast waves were characterized by self-emission imaging at pressures of 25-1000 mTorr of N_2 and He gas. It was found that blast waves formed in N_2 at pressures $\geq$ 50 mTorr and in He at pressures $\geq$ 250 mTorr. In both He and N_2 there was a fast plasma feature moving at 370 km/s. The bulk plasma was seen to initially propagate at a speed of 190 km/s and at 60 ns the blast wave propagation followed a trend of $r \propto t^{2/5}$. This propagation rate of the blast waves indicated that they were Sedov-Taylor blast waves. It was also seen that as the pressure increased, the width and position of the shock wave decreased, but the electron temperature and density increased.

Thomson scattering data were obtained in both 1D and 2D. 1D line-outs were obtained in vacuum (0.2 mTorr) and 25-1000 mTorr of N_2 and He gases. It was found that for the same pressures, T_e and n_e in blast waves are higher in N_2 than in He. The initial T_e and n_e in vacuum were lower than for any pressure of the background gas, and no density or temperature peaks were observed because no blast waves were formed. The shock waves in

N_2 are hotter and denser than in He at the same pressure because He has a larger mean free path than N_2 and thus the particles are less densely packed in He, leading to weaker shock waves. 2D Thomson scattering data were taken in 95 mTorr of N_2 and 700 mTorr of He at $t = 100$ ns after the heater beam fire. Blast waves were detected in both gases with n_e reaching a peak of $2 \times 10^{16}\ cm^{-3}$ in the blast wave fronts for both He and N_2 and T_e reaching peak values of 25 eV in N_2 and 30 eV in He. The He temperature was higher due to less radiation, which was reflected in the detection of fewer spectral lines.

The 2D data were used to obtain novel large scale measurements of electron temperature and density gradients within a plasma. These gradients were used to calculate a theoretical value for Biermann field generation due to the blast waves of 300-500 G. This calculation confirms that the Biermann battery effect should be active in the blast wave fronts and generate magnetic fields of significant value. Magnetic field measurements were made in the blast wave fronts for 95 mTorr of N_2. The magnetic field measurements show azimuthally symmetric fields reaching values up to 350 G. The directionality of the fields in the presence of blast waves and in a vacuum environment were consistent in all data planes. However, in a vacuum environment the fields were always measured to be much weaker, to peak much earlier, and to dissipate more quickly. The measured magnetic field values were within the predicted range of the Biermann generated fields calculated from the TS gradients. The agreement between the magnetic field measurements and the magnetic field calculated from the electron temperature and density gradients implies that a significant portion of the magnetic fields downstream of the observed blast waves are the result of magnetic field generation via the Biermann battery effect.

3D FLASH simulations were performed for the experimental shock wave conditions. It was found that the uncalibrated preliminary 3D simulations are in general agreement with the experimental results, but need to be adjusted to better match the experimentally measured n_e. Even with the discrepancies, the simulations revealed that the magnetic field generation via the Biermann battery effect is important for the entire duration of the experiment. The ratio between the Biermann on and Biermann off magnetic fields is consistent with the

ratio between the magnetic fields measured in the shock wave and vacuum cases. It can be concluded that the majority of the magnetic fields measured in the presence of hydrodynamic shock waves are due to magnetic field generation by the Biermann battery effect.

Reynolds number, magnetic Reynolds number and Prandtl number were calculated for the experimentally measured and simulated plasma values. It was found that in the shock wave at t=100 ns, $R_e = 1.5 \times 10^3$, $R_m = 77$ and $P_m = 5 \times 10^{-2}$. Thus, in the blast wave, the plasma is in a turbulent regime, any existing or generated magnetic fields are advected with the plasma flow, and magnetic diffusion dominates viscous diffusion. These figures were compared with values for astrophysical systems. It was found that the experimental, SNR shock, and stellar atmosphere values for the Reynolds and magnetic Reynolds numbers were all significantly larger than unity, and the Prandtl number was much smaller than unity. This leads to the conclusion that the dynamics and physics occurring in our experiments may be relevant to these systems. In general, astrophysical shocks have values of R_e and R_m that are much larger than unity. From this we can additionally conclude that the Biermann battery effect can be a significant source of magnetic fields in astrophysical shock waves. The confirmation of these Biermann-generated fields under such conditions in the laboratory is relevant to the understanding of magnetic fields generated by high Mach number shocks in space, and how these magnetic fields may affect star formation, the evolution of super nova remnants, and the mixing of the interstellar medium. It also supports the idea that the Biermann battery effect is a major source of protogalactic magnetic field generation.

5.1 Future Directions

There are a number of avenues that this research project could take in the future. These include the addition of new diagnostics and the study of Biermann generated fields in different laboratory environments. Future work also includes the continuation of the CMEC collaboration in which future students will work with the Flash Center for further testing and validation of the FLASH code.

The most immediate future work on this project is a second set of FLASH simulations. Although the preliminary results of the simulations agree with the experiments within an order of magnitude, they need to be calibrated to better match the experimental conditions. To do this, the simulations will be rerun with a modified laser drive. This should reduce the propagation velocity of the shock waves to match the experimentally measured velocities. A modified laser drive will also bring the simulated values of n_e and thus the magnetic fields closer to our measured values. Having calibrated simulations will provide a one-to-one comparison that will allow a more accurate measurement of what percentage of the experimentally measured fields are due to the Biermann battery. In addition, we would like to run simulations with a dummy b-dot probe that matches the dimensions of the probe used in the experiments. This will be done to determine the effect of the probe on the shock waves and magnetic field measurements.

All measurements presented in this thesis were made using a 3 mm b-dot probe. A new 1 mm, 3-axis b-dot probe could be constructed and used to collect more data. This would allow for higher resolution spatial scans. A smaller probe would also reduce the perturbation of the LPP and the blast waves generated in the system. Measurements with a 1 mm b-dot probe could be compared to the 3 mm probe measurements to ensure that the measured fields are not greatly affected by the presence of a large probe. In addition, a smaller probe would allow measurements to be made much closer to the target surface and laser path.

In addition to closer measurements with a smaller b-dot probe, Faraday rotation or Zeeman splitting could be added to obtain measurements at and very close to the target surface. In a vacuum case, the highest fields are generated extremely close to the target surface ($\leq$ 1 mm), so adding these diagnostics would allow measurements at this spatial scale. However, adding these diagnostics would be very difficult.

Experiments could also be done with different target materials. It has been observed in previous experiments that materials with higher Z values lead to higher Biermann fields generated [91, 4]. The fields generated by LPPs from targets such as aluminum could be studied in 3D to determine how the field strength and structure differ from plastic targets.

The generation of higher fields would also help in the introduction of new diagnostics such as Faraday rotation and Zeeman splitting, as these diagnostics require large fields. In addition, the dependence of Biermann generated fields as a function of laser energy for different targets could be investigated.

There are also a few avenues that this project could explore related to astrophysical processes. Fields generated by Biermann could be studied in colliding plasma bubbles, which is relevant to magnetic reconnection[58]. Not only would each bubble lead to the generation of magnetic fields, but when the bubbles collide there could be the generation of new magnetic fields due to turbulence or due to new T_e and n_e gradients created by the collision. It is also possible that, if the bubbles are energetic enough, a magnetic reconnection event could occur and the resulting magnetic fields could be studied. Another astrophysically relevant system would be the Biermann magnetic field generation in LPPs in the presence of a background plasma. Such experiments could be performed in the UCLA Large Plasma Device (LAPD) facility. The study of Biermann field generation in background plasmas could also be studied in the UCLA HEDP laboratory chambers. This could be accomplished by creating a background LPP with a first laser pulse and then shortly thereafter expanding a second LPP into it with a second laser pulse. The transition between Biermann- and Weibel-dominated field generation could also be studied. The transition between these regimes is relevant for plasma turbulence and shocks, but it occurs at $L/d_e = 100$ [80], where L is the characteristic length scale of your system and d_e is the electron inertial length.

APPENDIX A

Magnetic Flux Probe Building Guide

This probe building guide describes the materials and step by step directions on how to build a magnetic flux probe. When starting to build a probe for the first time, it will take at least 2x longer than expected and you will most likely break the wires and/or ceramic circuit board at least once during the process. It is extremely frustrating and I hope these tips make the process easier for you.

During the process of building my first probe, I broke about 5 ceramic circuit boards, had to re-solder the wires countless times, and even had to start from scratch multiple times. It's a difficult task and you will have problems along the way. Don't feel bad if you make a lot of mistakes, everyone struggles with their first probe.

Good Luck!!

A.1 Materials

- 3 2-wire twisted pairs (use ceramic coated for LAPD)
- 3 axis b-dot core
- Ceramic tube
- Ceramic cap adaptor
- Ceramic Cap
- 6 coax cables

- 6 Lemo plugs
- $3/8 - 1/2$ inch stainless steel tube
- Respective stainless steel plug/adaptor
- Circuit board (if not building for LAPD can use old design/non-ceramic circuit board)
- High temperature epoxy (if not building for LAPD epoxy does not need to be high temp)
- High temperature solder (if not building for LAPD can use any solder)
- razor (for taking coating off wires)
- Soldering iron
- Multimeter
- Tweezers
- Wire stripper/cutter
- Tape/ labels for wires
- Magnifying glass (if desired)

A.2 Winding the wires

- Optional: epoxy the adapter cap onto the ceramic tube so it has time to set while winding the coils
- You will first need to twist your wire pairs. There is a drill in the electronics lab that is used for this purpose. Get a wire 2x the desired length. Fold the wire in half and tape the loop end with blue tape. Connect drill to tape on the wire then use the drill

to twist the wires. Undo the tape and cut the loop in half to create a 2 wire pair. You will need 3 sets of 2 wires twisted together (6 wires total)

- Place the b-dot core in a small clamp stand by the two back corners. Make sure the core is as squared off as possible.
- Tape one side of your twisted wire pair to the table to hold it decently taught while winding
- Loop the wire pair around the core, pushing the wires flat onto each core side.
- When winding, make sure each loop does not overlap with others.
- Once all 5 loops are done (5 loops x 2 wires = 10 turns!), twist the two ends of the wire pair together leaving as little gap as possible between the extending wires and the core.
- Turn the cube and repeat on the remaining side(s).
- Keep in mind that the wires need to come off the cube all on the same face so that it can sit on the tube properly. You will have 4 wire ends per each face (12 total)
- When all axes are done, wind all wires together, leaving as little gap between the core and wires as possible. I suggest making each set a different length to make it easier to distinguish

A.3 Feeding wires through the probe shaft

- Cut your ceramic tube to your desired length. If you have not attached the adapter cap to your tube do so now
- Put the stainless steel cap on the ceramic tube but do not epoxy it to the tube

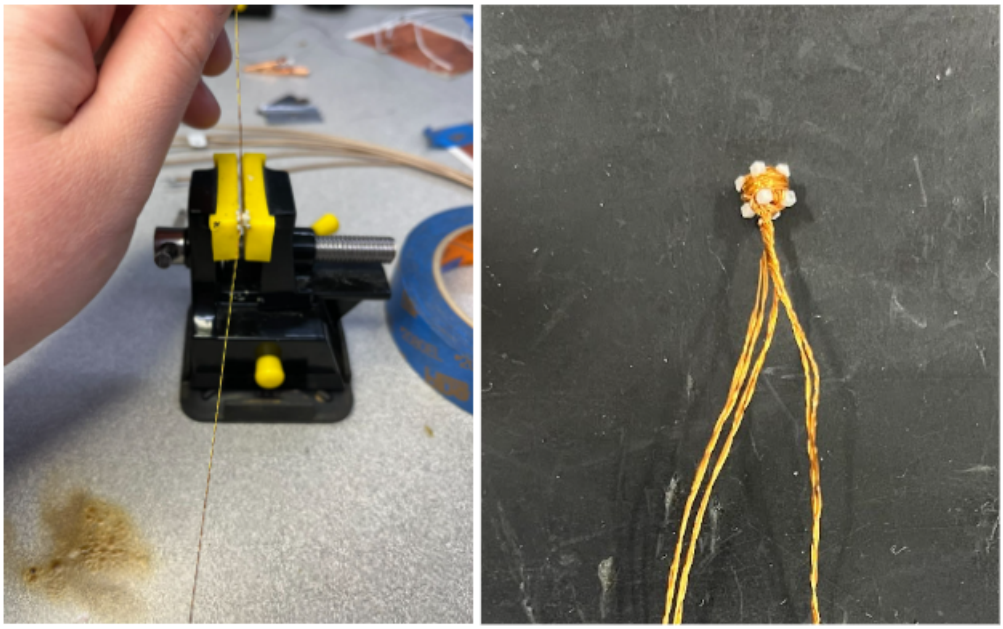

Figure A.1: (right) Winding the wires around the core (left) wound core with all wires twisted together

- You now have the option to epoxy the ceramic tube to the circuit board if you would like. I personally like to finish my soldering before attaching the tube to the circuit board to reduce stress points but this is up to your personal preference

- Once epoxy is set and the b-dot core is wound, twist the wires together and feed them through the ceramic adapter and tube combo. Then separate the wire pairs based on axis. Having three different lengths helps with separating the wires in this step

- Strip both ends of the coax cables by taking off the outer sheath, pushing back the braided wire then stripping of a small piece of the inner cable sheath (make sure the inner and outer cables don't make contact with each other)

- Connect Lemo connectors to one end of each of your coax cables and feed the coax cables through the stainless steel tube (it doesn't matter how far you feed them through the tube as long as you have stripped wires on one side and Lemos on the other).I suggest labeling each end of every coax cable so you know which one is which and can

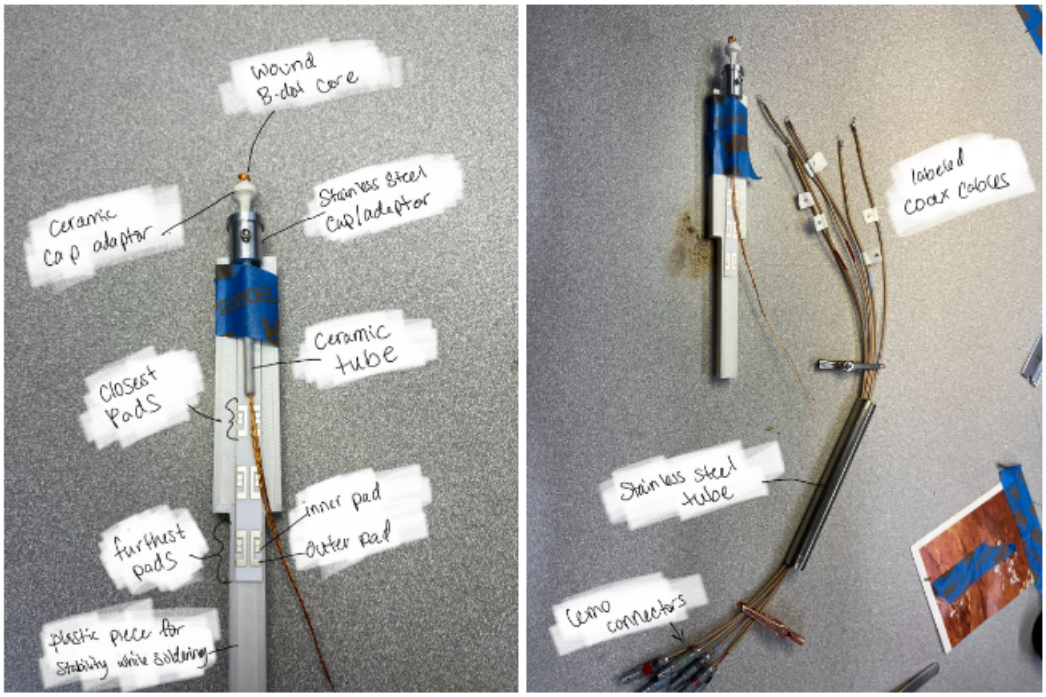

Figure A.2: (right) schematic of the b-dot assembly before soldering (left) b-dot assembly and labeled coax cable assembly needed before soldering

keep track of where they are all soldered. I like to color coat them in twos (2 labeled R, 2 labeled G, and 2 labeled B)

A.4 Soldering the wires

- First start securing the circuit board and ceramic tube to some sort of sturdy base. I like to use a piece of acrylic/plastic
- Strip the coating off a small portion of each wire end.
- Check which wires are connected to each other. For each axis you have 4 leads, when looking at the wires you should have two pairs of ends, wires from the opposite twisted ends will match with each other. Use a multi-meter to test the exposed ends of wire pairs to find out which ones are connected (ie. the ends of the same wire)

- Once you have found a wire pair you should either use tape to label them as matching or bend/twist them in a way that denotes they are connected. Do this until all wire connections are identified (should have 6 total)
- Solder one pair of coax cables to the furthest set of pads (see above picture). The outer braided wires connect to the outer pad and the inner wire to the inner pad. Solder the longest set of connected wires to the pads you just connected the coax cables to. One side of the connected wires to the inner pad and the other end to the outer pad. Do this for both connected pairs for the longest set of 4 wires
- Check with multi-meter to make sure the soldered connections are good (resistance should be around 2-4 ohms)
- Repeat this process for the shortest set of 4 wires on the closest pads
- Flip entire set up over so the soldered wires are on the bottom of the board. Repeat the soldering process with the remaining wires on the middle pads on the back of the board

A.5 Testing the probe

- Now that everything is soldered, the first test is to use a multi-meter to make sure the inside and outside of each pad are electrically connected
- Pick a face that you would like to denote at the y direction. Mark this on the cube and the ceramic tube for your reference
- Connect the B field tube and attenuator up to the multichannel analyzer in the electronics lab (can ask Kholi for help)
- Put the B-dot in the hole in the tube with the B field facing up (there is a label for directionality). Align the marked face to it is upward

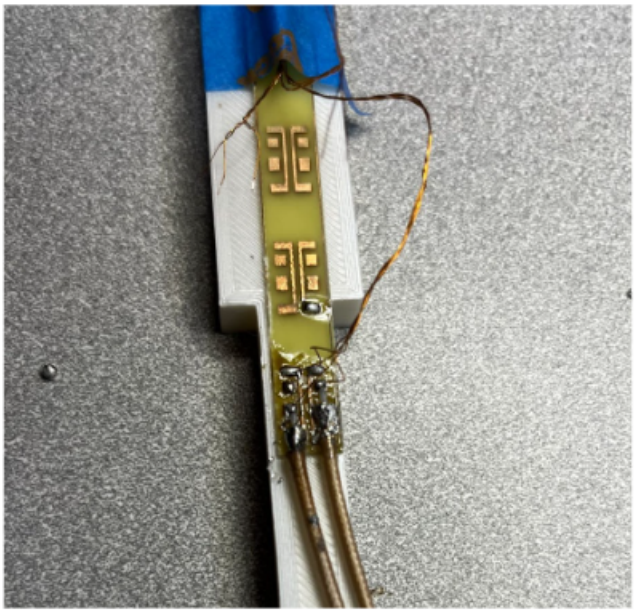

Figure A.3: Example for how wires should be soldered to board (old circuit board design shown here)

- Connect cables from difference axes until you see a good signal (around 15-25 dB). All cable connections should show low signals or noise except a single pair. The pair that shows a good signal should be marked as the y axis. The positive phase is y+ and the negative phase is y-. If they are both in the same direction, you need to flip one of the wire pairs on this set. If it all looks like noise, there is most likely a short somewhere

- Turn tube on its side but leave b-dot is same orientation still going through the hole. Connect the remaining wires for the largest signal. this is the z axis. Label these cables is positive phase +z and negative phase -z. If they are both in the same direction, you need to flip one of the wire pairs on this set

- Take the b-dot out and put it through the end of the tube with the direction of the B field going away from the side you inserted the probe. (for LAPD the direction of B should be opposite). Face the b-dot so the marked side is still facing up. Check to make sure the remaining coax connections give a good signal, this is the x axis (y axis for LAPD). Label these cables is positive phase +x and negative phase -x. If they are

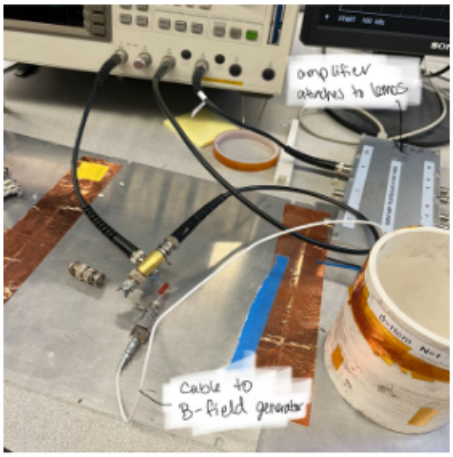

Figure A.4: Picture of set up for testing probe

both in the same direction, you need to flip one of the wire pairs on this set

A.6 Final Steps

Once all the axes are working properly and labeled, fold the wires down over the circuit board creating as few new loops in the wires as possible. Wrap the entire circuit board with teflon tape. This is hard because it isn't actually sticky but it will help getting it into the tube. If there is a lot of stray pick up, you may also need to wrap the board and wires with copper foil. Use set screws to secure the stainless steel cap to the ceramic shaft. Carefully slide the stainless steel tube over the circuit board. If you are using a 3/8 tube, this will be a very tight fit so be careful not to snap the board while doing this. If you successfully get the tube on, use a screw to secure tube onto the cap. Retest the probe to make sure no axes broke while inserting it into the tube. Denote which direction is +y on the stainless steel tube for future reference

Once everything is assembled and the probe is working properly, epoxy the cap over the b-dot core. Be sure to not get epoxy in the probe shaft, only on the cap and cap adapter. When dry, test the probe one last time to ensure it works. Calibrate the probe using the calibration set up in the electronics lab which is described in section 3.2.

APPENDIX B

Additional Data

Measurements were taken in XZ, XY and YZ planes in order to get an idea of the 3D structure of the blast waves and Biermann field generation. Representations of the orientation of the data planes are shown in figure B.1.

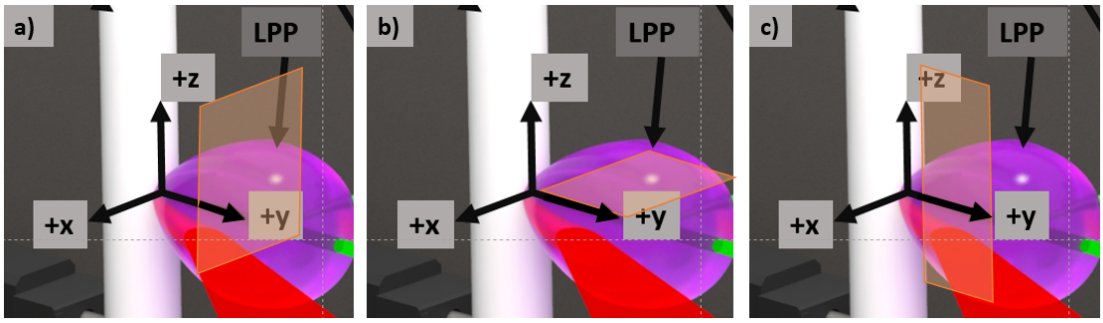

Figure B.1: Orientation of data planes (translucent orange planes) with respect to the laser path and LPP blow-off axis (+y-axis). a) Representation of an XZ plane which is perpendicular to the y-axis. b) Representation of an XY plane which is perpendicular to the z-axis. c) Representation of a YZ plane which is perpendicular to the x-axis.

The x-component,z-component and magnitude of magnetic field measurements in blast waves and in vacuum an XZ planes are shown for various times in figures B.2,B.3 and B.4 respectively. B_y is not shown because a negligible amount of the field is along this axis compared to the other components. The magnetic fields measurements in the presence of blast waves reveal much higher magnetic fields than the vacuum case reaching a magnitude of up to 350 G upstream of the blast wave fronts. These fields additionally show the same azimuthal structure which was measured previously[74]. The peak magnetic fields were

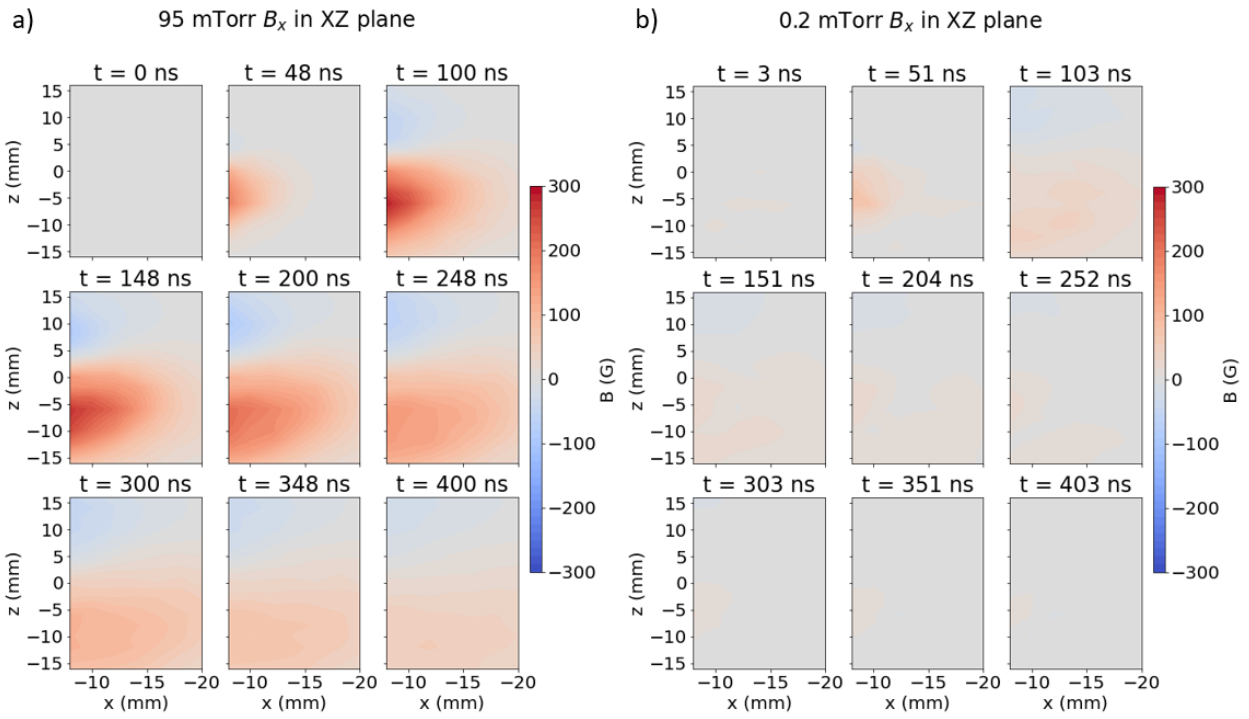

Figure B.2: Contour plots of the B_x component of magnetic field measurements in an XZ plane at $y = 11$ mm for various times after heater beam fire. Red represents fields in +x direction and blue in the -x direction. a) B_x a in the presence of a blast wave in 95 mTorr of N_2 gas. Peak fields of $B_x = 300$ G were seen to occur between 100-150 ns. b) B_x in vacuum (0.2 mTorr). Peak fields of $B_x = 50$ G were seen to occur around 50 ns.

detected at a later time and were measured to last longer than the vacuum case. This confirms that the higher magnetic fields are due to the blast waves which propagate much slower than those in vacuum.

The x-component of magnetic field measurements in a YZ plane are shown for a blast wave in 95 mTorr of N_2 gas and in vacuum (0.2 mTorr) for various times after laser fire are shown in figure B.5. The peak magnitude of the fields reached a value of $B_{mag} = 370$ G which was only 10 G higher than the x-component of the magnetic field in this plane, indicating that the primary direction of the magnetic fields in this plane are in the ±x-directions. As with the XZ planes, the fields in the presence of blast waves are much stronger than in a vacuum environment. The fields and their structure also persist for a much longer time

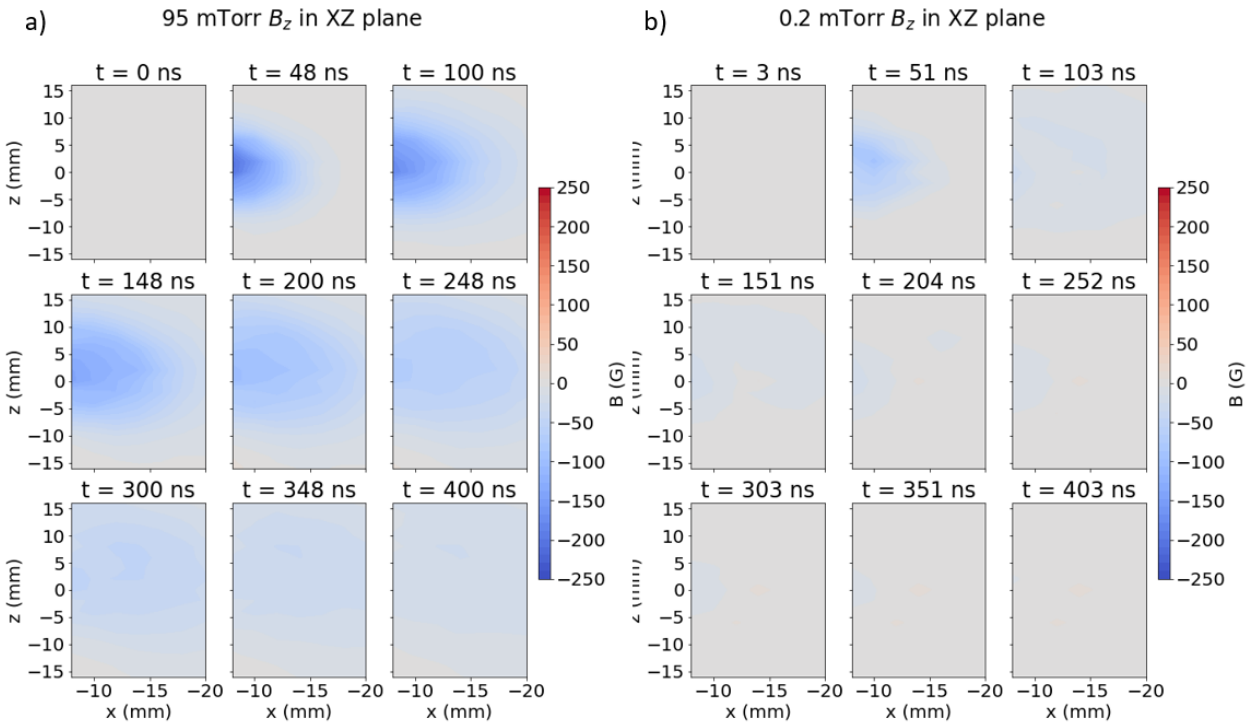

Figure B.3: Contour plots of the B_z component of magnetic field measurements in an XZ plane at $y = 11$ mm for various times after heater beam fire. Red represents fields in +x direction and blue in the -x direction. a) B_z field data in the presence of a blast wave in 95 mTorr of N_2 gas. Peak fields of $B_Z = 250$ G were seen to occur between 100-150 ns. b) B_z in vacuum (0.2 mTorr). Peak fields of $B_z = 50$ G were seen to occur around 50 ns.

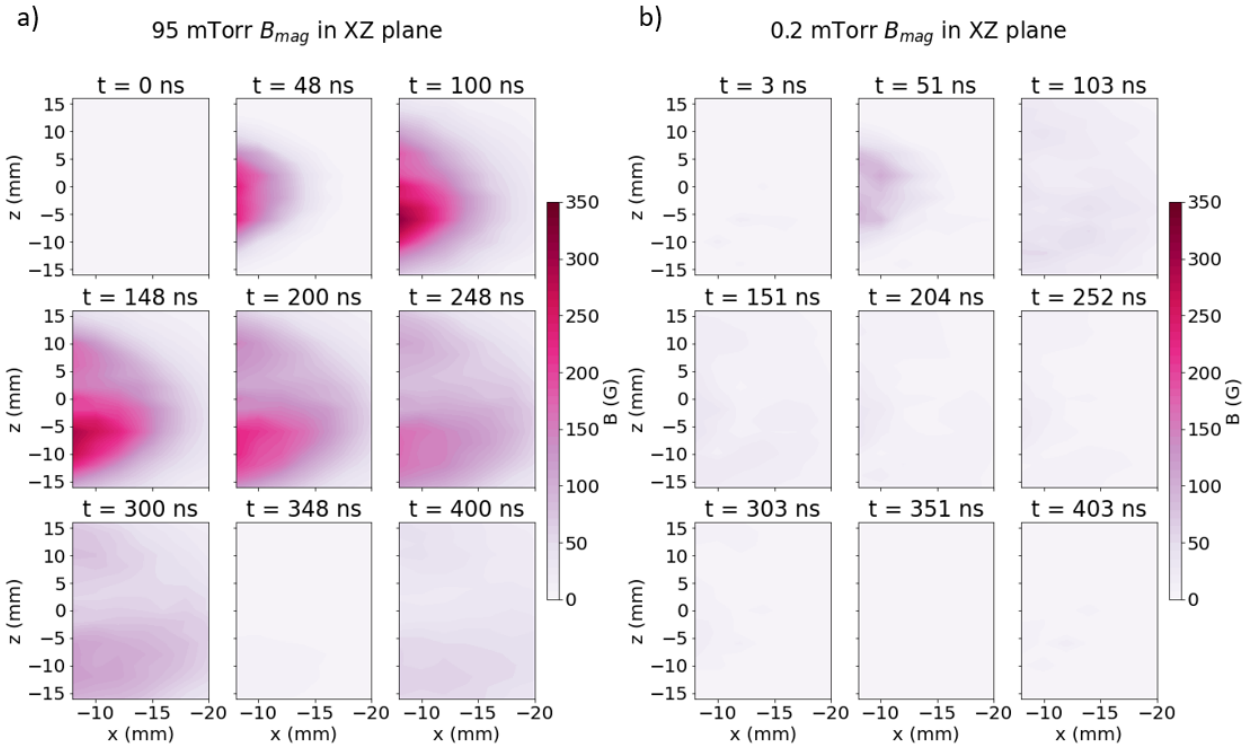

Figure B.4: Contour plots of the magnitude of the measured magnetic fields in an XZ plane at $y = 11$ mm for various times after heater beam fire. a) B_{mag} field data in the presence of a blast wave in 95 mTorr of N_2 gas. Peak fields of $B_{mag} = 350$ G were seen to occur between 100-150 ns. b) B_{mag} in vacuum (0.2 mTorr). Peak fields of $B_{mag}100$ G were seen to occur around 50 ns.

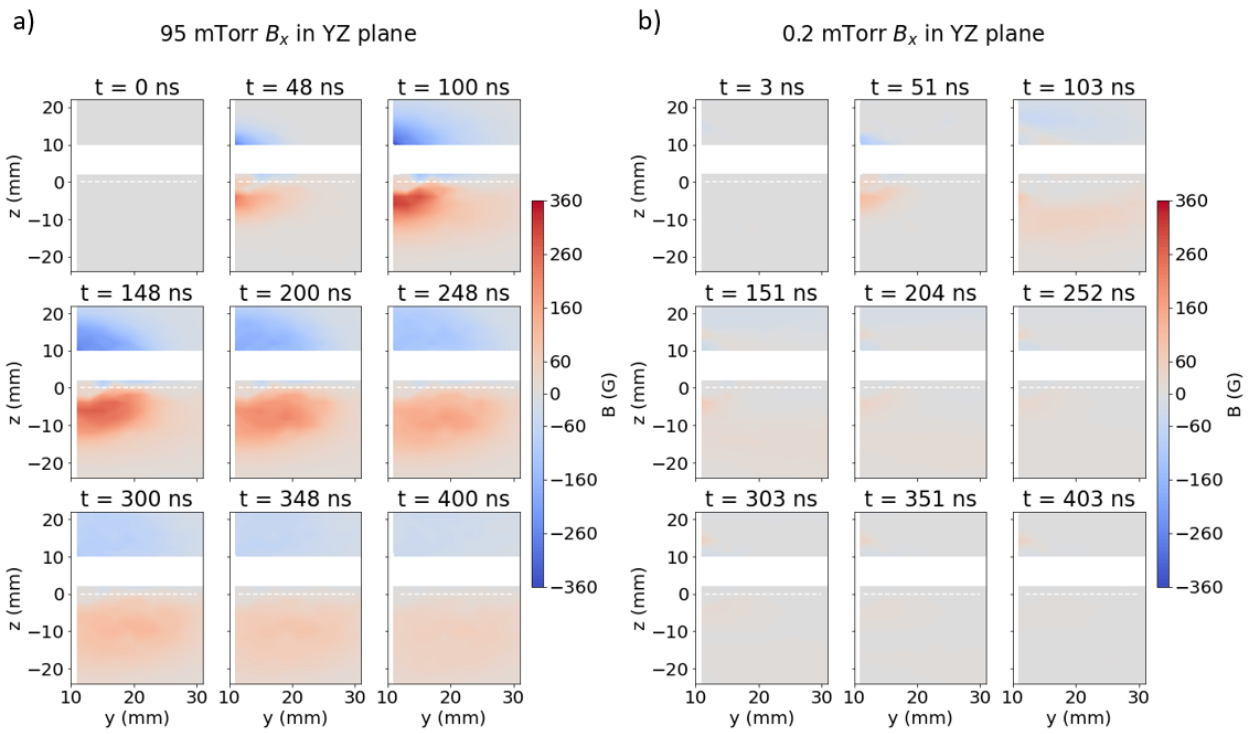

Figure B.5: Contour plots of the B_x component of magnetic field measurements in an YZ plane at $x = 0$ mm for various times after heater beam fire. Red represents fields in +x direction and blue in the -x direction. a) B_x in the presence of a blast wave in 95 mTorr of N_2 gas. Peak fields of $B_x = 360$ G were seen to occur between 100-150 ns. b) B_x in vacuum (0.2 mTorr). Peak fields of $B_x = 100$ G were seen to occur around 50 ns.

upstream of the blast wave front than fields in vacuum where no blast wave is formed.

Contour plots of the B_z component of magnetic field measurements in an XY plane at $z = -0.5$ mm for various times after heater beam fire are shown in figure B.6. As expected, B_z is in the -z direction but the fields are weaker than expected in the blast wave case. This is due to an accidental offset of the plane relative to the laser spot of -5 mm. Contour plots of the magnitude of the magnetic fields in an XY plane at $z = -5$ mm for various times after heater beam fire are shown in figure B.7. The magnitude of the magnetic fields in this plane were a bit lower than those measured in the other planes (by a factor of 0.5) but show reasonable agreement with the other plane measurements. Even though B_z and B_{mag} were

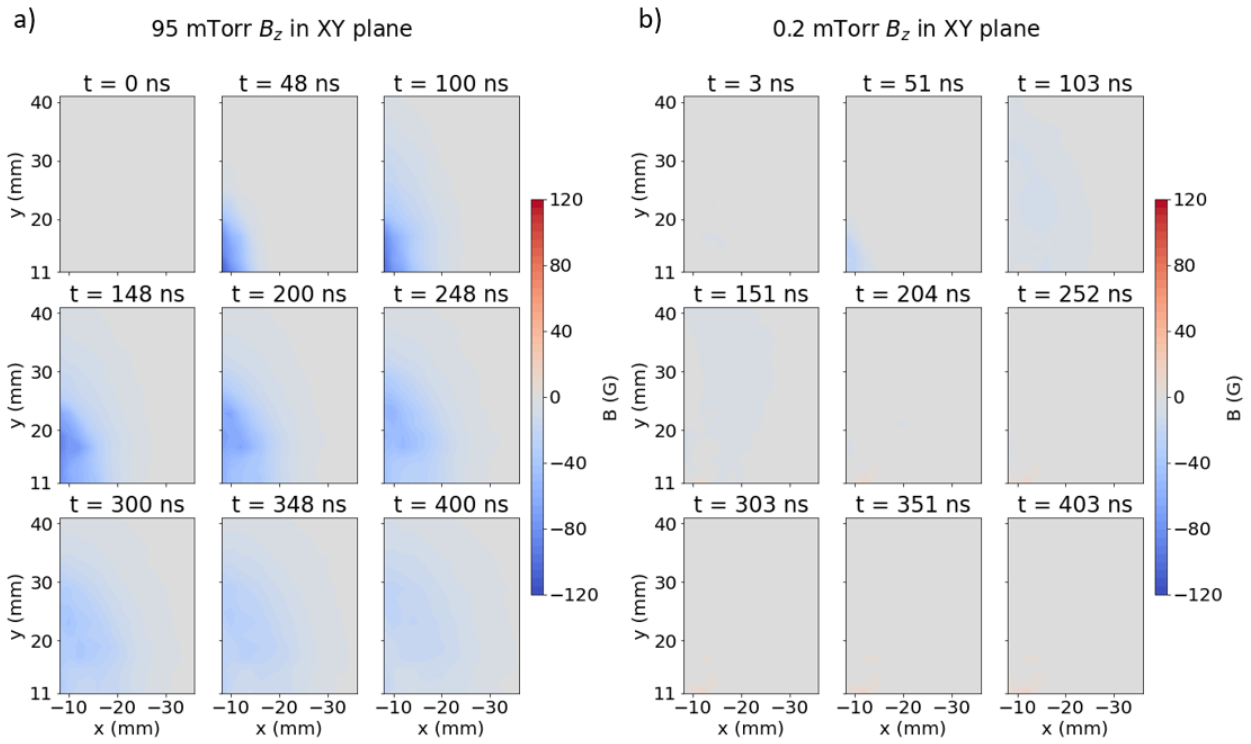

Figure B.6: Contour plots of the B_z component of magnetic field measurements in an XY plane at $z = -0.5$ mm for various times after heater beam fire. As expected, B_z is in the -z direction. a) B_z in the presence of a blast wave in 95 mTorr of N_2 gas. Peak fields of $B_z = 120$ G were seen to occur between 100-150 ns. b) B_z in vacuum (0.2 mTorr). Peak fields of $B_x = 40$ G were seen to occur around 50 ns.

lower than expected, the fields were still measured to be much higher, peak later, and persist longer in the presence of blast waves than fields in a vacuum environment.

A comparison between XY, XZ and YZ planes at t=100 ns after heater beam fire is shown in figure B.8. It should be noted that each plane is taken at a different distance from the target surface due to proximity to the heater beam path. The YZ plane was taken closest to the heater beam spot, on axis above and below the laser path. This plane contains highest measured fields reaching 400 G which take up the largest spatial region. This is due to the fact that the blast wave and thus the fields travel the smallest distance before detection. The XZ plane has a similar structure to the YZ plane and was taken over similar coordinates as

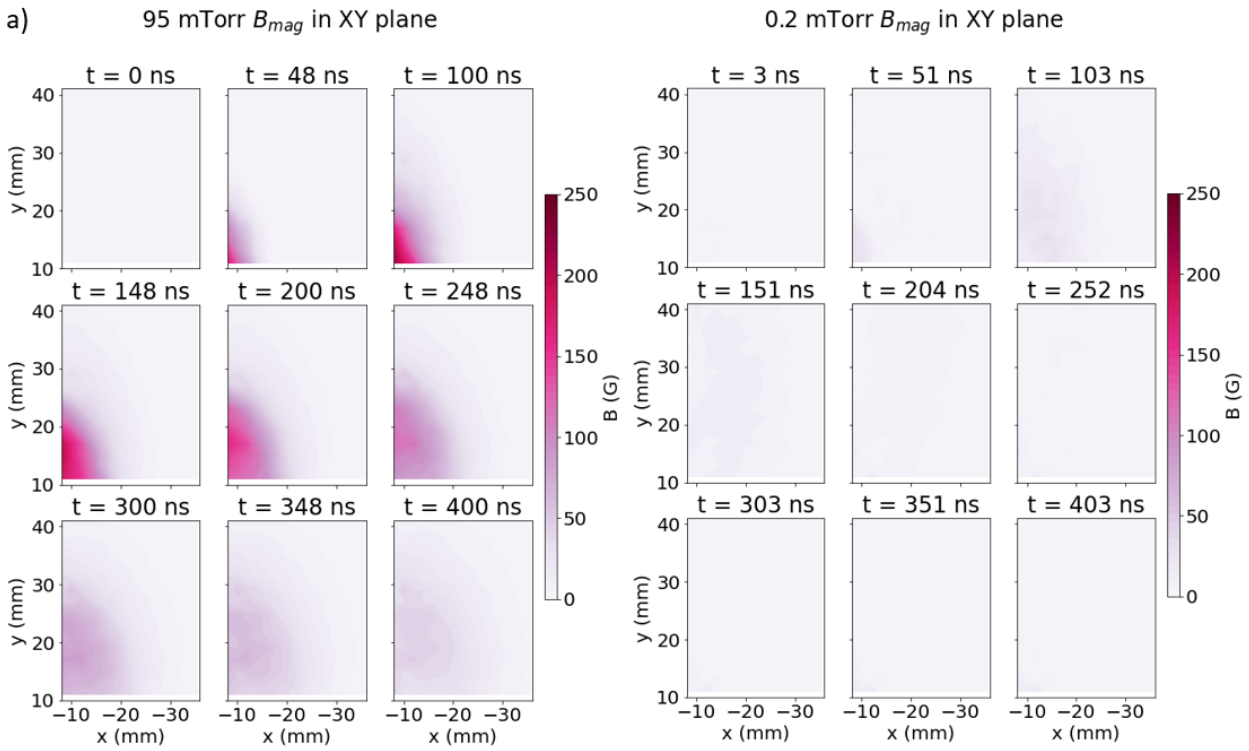

Figure B.7: Contour plots of B_{mag} measurements in an XY plane at $z = -0.5$ mm for various times after heater beam fire. a) B_{mag} in the presence of a blast wave in 95 mTorr of N_2 gas. Peak fields of $B_{mag} = 220$ G were seen to occur between 100-150 ns. b) B_z in vacuum (0.2 mTorr). Peak fields of $B_{mag} = 40$ G were seen to occur around 50 ns.

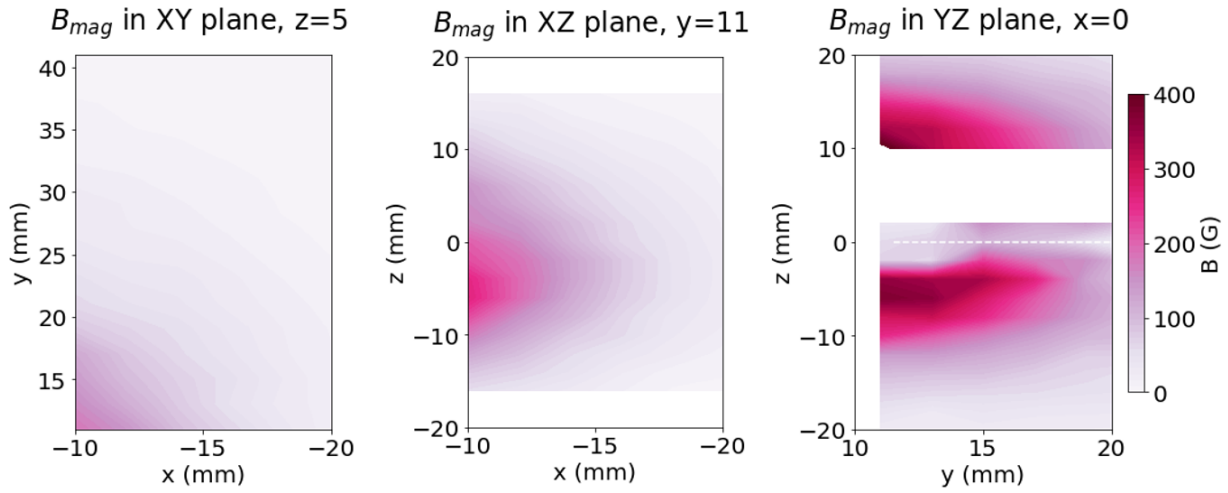

Figure B.8: Magnetic field magnitude at t=100 ns after heater beam fire. **Left:** B_{mag} in an XY plane at z = 5 mm. Peak values reach $B_{mag} = 180$ G. **Middle:** B_{mag} in an XZ plane at y = 11 mm. Peak values reach $B_{mag} = 300$ G. **Right:** B_{mag} in an YZ plane at x = 0 mm. Peak values reach $B_{mag} = 400$ G.

the YZ plane but was measured at y=11 mm as opposed the x=0 mm of the YZ plane. The XZ plane had a peak magnitude of 260 G, which is reasonable compared to the 400 G in the YZ due to the 11 mm distance from the target surface. The XY plane had an accidental offset from the z axis of z=5 mm causing the slice of the blast wave magnetic fields measured to not contain the full picture of what occurred along this axis. The fields measured in this plane only reached a peak of 180 G which is much lower than the other planes, however, due to the offset in z this is not a completely unreasonable value. In all planes, it was seen that the magnitude of the magnetic field measurements in the presence of blast waves were greater by at least 100 G than those obtained in a vacuum environment, further confirming that blast waves lead to much higher magnetic field values.

APPENDIX C

Diversity, Equity and Inclusion Involvement

It has long been known that many STEM fields are not very diverse. Though many efforts have been put toward increasing diversity, equity and inclusion (DEI) in many physics and astronomy departments, there is a lot of work still to be done. According to the NSF, only 21% of physics doctorate recipients are women, and only a meager 6% of physics doctorates are awarded to Black or African American, Indigenous, and Hispanic or Latino American students collectively[5]. The percentage of undergraduate degrees in physics also mirrors a similar trend; about 75% of bachelors' degrees in physics from 2016-2020 were awarded to white students[5]. Though these numbers have increased over the years, based on the current statistics, it is not surprising that people of marginalized identities feel under-represented, under-valued and under-supported in physics.

As a woman in physics, I understand the struggles marginalized identities face in our field. Based on my own experiences, I know how valuable strong support, mentorship, and community are for success. As such, I became very involved in diversity, equity and inclusion efforts in the UCLA physics and astronomy with hopes that I could improve the climate for other marginalized identities in the department. The DEI activities that I have been involved in include but are not limited to:

- UCLA Physics and Astronomy graduate council outreach coordinator 2019-2020 academic year
- Founding member of UCLA Marginalized Identities in Physics and Astronomy (MIPA)
- MIPA council member, 2020-2023 academic years

- Lead and head founder of MIPA Critical Mentoring and Academic Strategies for Success (MASS) program, 2020-2023 academic years
- MIPA Critical MASS undergraduate mentor, Jan 2020- June 2022
- Organized fieldtrip for physics students from local high school that serves underprivileged children, Winter 2021

I am particularly proud of my role in the founding of MIPA and its subsequent programs. I would like to expand on the ideals and efforts of UCLA MIPA to give an insight to my philosophy about and dedication to DEI in STEM.

Come the end of my second year of grad school, moral for marginalized identities in physics was at a low with the height of the Black Lives Matter protests and soon after the start of the pandemic lock downs. Through discussions with a member of my cohort who identifies as a person of color, we came to the conclusion that we needed more support groups in our department for marginalized identities. However, we realized if we created more groups on top of the existing Women in Physics and Astronomy (WiPA) group, each would have a small number of members and the bulk of the work would fall to the students we aimed to aid. Thus we came up with the idea to transition WiPA into one big umbrella group that could provide support for all marginalized identities in the department. After months of preparation and work, Marginalized Identities in Physics and Astronomy (MIPA) was born.

We wanted MIPA to be an effective support structure for all marginalized identities in the department. This led us to adopt a framework of intersectionality. The framework of intersectionality was developed by Dr. Kimberlé Crenshaw to examine how the superposition of multiple marginalized identities interface and interact to form compounding inequities and disadvantages[16, 73]. Intersectionality provides a lens for us to understand the overt and subtle discrimination faced by our intersectional communities and helps up to reflect on the social systems of privilege and oppression that limit their progress and success. We believe this framework is an important tool to allow us to provide the necessary support for every

identity MIPA serves. To help our community understand why we had created MIPA in place of other groups, we drafted a full statement on intersectionality[45] and a mission statement[45]:

> UCLA Marginalized Identities in Physics and Astronomy (UCLA MiPA) is dedicated to building a more inclusive, accessible, and equitable environment for our graduate students who identify with one or more marginalized groups, including but not limited to: women+; Black, Indigenous, and People of Color (BIPOC); LGBTQIA+ folks; neurodiverse and disabled people. We strive to provide an intersectional support network for these students who face systemic barriers to success in graduate school by building community, fostering camaraderie, and promoting allyship.

MIPA held many events for our members both during and after the pandemic lock down such as general member socials, MIPA tea where we discuss current topics and issues related to DEI in STEM, and affinity group meetings. We are also an outlet that marginalized students can reach out to when they are having problems such as micro aggressions or lacking access to accommodations. The council members take these complaints to our MIPA advisor and with him advocate to help resolve the issues. The MIPA council members have also been involved in general department DEI efforts. We worked with the department's DEI committee during their review of the department's DEI programs, we were involved in new faculty hire interviews, helped remove the ranking system on our comprehensive exam, helped remove locks on women restrooms, aided in the creation of a gender neutral restroom in our building, and more.

The most successful program organized within MIPA's range of activities, and one that I personally created and led, is the Critical Mentoring and Academic Strategies for Success (MASS) program. This is a looping undergraduate mentorship program which serves all undergraduates in the department with an emphasis on serving those of marginalized identities. Mentoring is a cause I am very passionate about as it has had a huge impact on my

success as a physicist. This program was created through months of research on successful mentoring strategies and discussions with faculty members and physics undergraduate students to ensure that we would successfully serve the undergraduate students' needs. Each mentoring group consists of a graduate student mentor, 1-2 upper division undergraduate students (including transfer students) and a small group (1-4) lower division undergraduate students. Mentorship groups are paired based first on common identities then on research interests with a priority on matching students who identify as being part of a marginalized group. Graduate mentors provide one-on-one mentoring to their upper division student(s) and the grad mentor and upper division student mentor the lower division student(s) together. Once the lower division student reaches their third year, they are transitioned to an upper division mentee and receive one-on-one mentoring from their grad mentor and help them mentor new lower division students. All people involved in the program are required to attend a mentorship training. We also provide a Critical MASS program guide and monthly mentoring reminders with suggested topics for groups who may be unsure what to discuss. I led this program from its beginning in 2020 to the end of the 2022-23 academic year. I also served as a graduate mentor through which I mentored two undergraduate women, one for her last two years at UCLA and one from her second year through graduation. The MIPA Critical MASS program has been the most successful undergraduate mentorship program the department has ever had and I believe it has made a great impact on our marginalized undergraduate students.

With our PhD journeys coming to a close, the founding members and I have helped transition new graduate students into council member roles to continue MIPA's mission. This new MIPA leadership is also continuing the Critical MASS program and expanding it to better serve transfer students in the department. Through MIPA I was able to serve and support students of marginalized identities in the physics and astronomy department while at the same time receiving that very same support and sense of belonging. I hope this program continues to serve as a source of community and support for all marginalized identities in the UCLA physics and astronomy department.

References

[1] David A. Allen and Michael G. Burton. Explosive ejection of matter associated with star formation in the orion nebula. *Nature*, 363(6424):54–56, may 1993.

[2] R. Beck. Magnetic field structure from synchrotron polarization. *EAS Publications Series*, 23:19–36, 2007.

[3] L. Biermann. Über den ursprung der magnetfelder auf sternen und im interstellaren raum. *Zeitschrift Fur Naturforschung*, 1949.

[4] R. S. Bird, L. L. McKee, F. Schwirzke, and A. W. Cooper. Pressure dependence of self-generated magnetic fields in laser-produced plasmas. *Physical Review A*, 7(4):1328–1331, apr 1973.

[5] Liz Boatmann. Newest data shows mixed progress for women and marginalized groups in physics higher ed. *APS News*, 31(10), November 2022.

[6] A. S. Bondarenko, D. B. Schaeffer, E. T. Everson, S. E. Clark, B. R. Lee, C. G. Constantin, S. Vincena, B. Van Compernolle, S. K. P. Tripathi, D. Winske, and C. Niemann. Collisionless momentum transfer in space and astrophysical explosions. *Nature Physics*, 13(6):573–577, feb 2017.

[7] Archie F. A. Bott, Petros Tzeferacos, Laura Chen, Charlotte A. J. Palmer, Alexandra Rigby, Anthony R. Bell, Robert Bingham, Andrew Birkel, Carlo Graziani, Dustin H. Froula, Joseph Katz, Michel Koenig, Matthew W. Kunz, Chikang Li, Jena Meinecke, Francesco Miniati, Richard Petrasso, Hye-Sook Park, Bruce A. Remington, Brian Reville, J. Steven Ross, Dongsu Ryu, Dmitri Ryutov, Fredrick H. Séguin, Thomas G. White, Alexander A. Schekochihin, Donald Q. Lamb, and Gianluca Gregori. Time-resolved turbulent dynamo in a laser plasma. *Proceedings of the National Academy of Sciences*, 118(11), mar 2021.

[8] S.I. Braginskii. Transport processes in a plasma. *Reviews of Plasma Physics*, 1:205, 1965.

[9] P. T. Campbell, C. A. Walsh, B. K. Russell, J. P. Chittenden, A. Crilly, G. Fiksel, L. Gao, I. V. Igumenshchev, P. M. Nilson, A. G. R. Thomas, K. Krushelnick, and L. Willingale. Measuring magnetic flux suppression in high-power laser–plasma interactions. *Physics of Plasmas*, 29(1):012701, jan 2022.

[10] Roger S. Case and Fred Schwirzke. Background gas pressure dependence and spatial variation of spontaneously generated magnetic fields in laser-produced plasmas. *Journal of Applied Physics*, 46(4):1493–1498, apr 1975.

[11] J. I. Castor. Astrophysical radiation hydrodynamics: The prospects for scaling. *Astrophysics and Space Science*, 307(1), May 2006.

[12] L. E. Chen, A. F. A. Bott, P. Tzeferacos, A. Rigby, A. Bell, R. Bingham, C. Graziani, J. Katz, M. Koenig, C. K. Li, R. Petrasso, H.-S. Park, J. S. Ross, D. Ryu, T. G. White, B. Reville, J. Matthews, J. Meinecke, F. Miniati, E. G. Zweibel, S. Sarkar, A. A. Schekochihin, D. Q. Lamb, D. H. Froula, and G. Gregori. Transport of high-energy charged particles through spatially intermittent turbulent magnetic fields. *The Astrophysical Journal*, 892(2):114, apr 2020.

[13] PlasmaPy Community. Plasmapy, version 2023.1.0, zenodo. 2023. Available online: https://zenodo.org/record/7529964, (accessed on 29 July 2023).

[14] R. S. Craxton and M. G. Haines. Hot spots in laser plasmas. *Physical Review Letters*, 35(20):1336–1339, nov 1975.

[15] R S Craxton and M G Haines. J b acceleration of fast ions in laser-target interactions. *Plasma Physics*, 20(6):487–502, jun 1978.

[16] K. Crenshaw. Demarginalizing the intersection of race and sex: A black feminist critique of antidiscrimination doctrine, feminist theory and antiracist politics. *University of Chicago Legal Forum*, (8), 1989.

[17] C.B. Dane, L.E. Zapata, W.A. Neuman, M.A. Norton, and L.A. Hackel. Design and operation of a 150 w near diffraction-limited laser amplifier with SBS wavefront correction. *IEEE Journal of Quantum Electronics*, 31(1):148–163, 1995.

[18] AW DeSilva and GC Goldenbaum. 3. plasma diagnostics by light scattering. In *Methods in experimental physics*, volume 9, pages 61–113. Elsevier, 1971.

[19] R. S. Dorst, C. G. Constantin, D. B. Schaeffer, J. J. Pilgram, and C. Niemann. Planar laser induced fluorescence mapping of a carbon laser produced plasma. *Review of Scientific Instruments*, 93(10), oct 2022.

[20] R. S. Dorst, P. V. Heuer, D. B. Schaeffer, C. G. Constantin, and C. Niemann. Measurements of ion velocity distributions in a large scale laser-produced plasma. *Review of Scientific Instruments*, 91(10):103103, oct 2020.

[21] R. S. Dorst, D. B. Schaeffer, A. Le, J. J. Pilgram, C. G. Constantin, S. Vincena, S. K. P. Tripathi, D. Winske, D. Larson, M. Cowee, and C. Niemann. High repetition rate mapping of the interaction between a laser plasma and magnetized background plasma via laser induced fluorescence. *Physics of Plasmas*, 29(8), aug 2022.

[22] A. D. Edens, R. G. Adams, P. Rambo, L. Ruggles, I. C. Smith, J. L. Porter, and T. Ditmire. Study of high mach number laser driven blast waves in gases. *Physics of Plasmas*, 17(11):112104, nov 2010.

[23] A. D. Edens, T. Ditmire, J. F. Hansen, M. J. Edwards, R. G. Adams, P. Rambo, L. Ruggles, I. C. Smith, and J. L. Porter. Study of high mach number laser driven blast waves. *Physics of Plasmas*, 11(11):4968–4972, nov 2004.

[24] D E Evans and J Katzenstein. Laser light scattering in laboratory plasmas. *Reports on Progress in Physics*, 32(1):207–271, jan 1969.

[25] E. T. Everson, P. Pribyl, C. G. Constantin, A. Zylstra, D. Schaeffer, N. L. Kugland, and C. Niemann. Design, construction, and calibration of a three-axis, high-frequency magnetic probe (b-dot probe) as a diagnostic for exploding plasmas. *Review of Scientific Instruments*, 80(11):113505, nov 2009.

[26] M. Fatenejad, A.R. Bell, A. Benuzzi-Mounaix, R. Crowston, R.P. Drake, N. Flocke, G. Gregori, M. Koenig, C. Krauland, D. Lamb, D. Lee, J.R. Marques, J. Meinecke, F. Miniati, C.D. Murphy, H.-S. Park, A. Pelka, A. Ravasio, B. Remington, B. Reville, A. Scopatz, P. Tzeferacos, K. Weide, N. Woolsey, R. Young, and R. Yurchak. Modeling HEDLA magnetic field generation experiments on laser facilities. *High Energy Density Physics*, 9(1):172–177, mar 2013.

[27] M. Fatenejad, B. Fryxell, J. Wohlbier, E. Myra, D. Lamb, C. Fryer, and C. Graziani. Collaborative comparison of simulation codes for high-energy-density physics applications. *High Energy Density Physics*, 9(1):63–66, mar 2013.

[28] B. Fryxell, K. Olson, P. Ricker, F. X. Timmes, M. Zingale, D. Q. Lamb, P. MacNeice, R. Rosner, J. W. Truran, and H. Tufo. FLASH: An adaptive mesh hydrodynamics code for modeling astrophysical thermonuclear flashes. *The Astrophysical Journal Supplement Series*, 131(1):273–334, nov 2000.

[29] L. Gao, P. M. Nilson, I. V. Igumenshchev, M. G. Haines, D. H. Froula, R. Betti, and D. D. Meyerhofer. Precision mapping of laser-driven magnetic fields and their evolution in high-energy-density plasmas. *Physical Review Letters*, 114(21), may 2015.

[30] S. Ghazaryan, M. Kaloyan, W. Gekelman, Z. Lucky, S. Vincena, S. K. P. Tripathi, P. Pribyl, and C. Niemann. Thomson scattering on the large plasma device. *Review of Scientific Instruments*, 93(8):083514, aug 2022.

[31] S. Ghazaryan, M. Kaloyan, and C. Niemann. Silica raman scattering probe for absolute calibration of thomson scattering spectrometers. *Journal of Instrumentation*, 16(08):P08045, aug 2021.

[32] Stephen Gibson, Daniel D. Hickstein, Roman Yurchak, Mikhail Ryazanov, Dhrubajyoti Das, and Gilbert Shih. Pyabel/pyabel: v0.9.0, 2022.

[33] A. Gopal, M. Tatarakis, F. N. Beg, E. L. Clark, A. E. Dangor, R. G. Evans, P. A. Norreys, M. S. Wei, M. Zepf, and K. Krushelnick. Temporally and spatially resolved measurements of multi-megagauss magnetic fields in high intensity laser-produced plasmas. *Physics of Plasmas*, 15(12):122701, dec 2008.

[34] Carlo Graziani, Petros Tzeferacos, Dongwook Lee, Donald Q. Lamb, Klaus Weide, Milad Fatenejad, and Joshua Miller. THE BIERMANN CATASTROPHE IN NUMERICAL MAGNETOHYDRODYNAMICS. *The Astrophysical Journal*, 802(1):43, mar 2015.

[35] G. Gregori, F. Miniati, B. Reville, and R.P. Drake. Magnetic field generation by biermann battery and weibel instability in laboratory shock waves. *EAS Publications Series*, 58:23–26, 2012.

[36] G. Gregori, A. Ravasio, C. D. Murphy, K. Schaar, A. Baird, A. R. Bell, A. Benuzzi-Mounaix, R. Bingham, C. Constantin, R. P. Drake, M. Edwards, E. T. Everson, C. D. Gregory, Y. Kuramitsu, W. Lau, J. Mithen, C. Niemann, H.-S. Park, B. A. Remington, B. Reville, A. P. L. Robinson, D. D. Ryutov, Y. Sakawa, S. Yang, N. C. Woolsey, M. Koenig, and F. Miniati. Generation of scaled protogalactic seed magnetic fields in laser-produced shock waves. *Nature*, 481(7382):480–483, jan 2012.

[37] J. Grun, J. Stamper, C. Manka, J. Resnick, R. Burris, J. Crawford, and B. H. Ripin. Instability of taylor-sedov blast waves propagating through a uniform gas. *Physical Review Letters*, 66(21):2738–2741, may 1991.

[38] M. G. Haines. Magnetic-field generation in laser fusion and hot-electron transport. *Canadian Journal of Physics*, 64(8):912–919, aug 1986.

[39] J. L. Han, R. N. Manchester, A. G. Lyne, G. J. Qiao, and W. van Straten. Pulsar rotation measures and the large-scale structure of the galactic magnetic field. *The Astrophysical Journal*, 642(2):868–881, may 2006.

[40] J. F. Hansen, M. J. Edwards, D. H. Froula, G. Gregori, A. D. Edens, and T. Ditmire. Laboratory observation of secondary shock formation ahead of a strongly radiative blast wave. *Physics of Plasmas*, 13(2):022105, feb 2006.

[41] C. Heiles. Zeeman splitting opportunities and techniques at arecibo. *Astrophysical Letters and Communications*, 37:85–107, 1998.

[42] P. V. Heuer, M. S. Weidl, R. S. Dorst, D. B. Schaeffer, A. S. Bondarenko, S. K. P. Tripathi, B. Van Compernolle, S. Vincena, C. G. Constantin, C. Niemann, and D. Winske. Observations of a field-aligned ion/ion-beam instability in a magnetized laboratory plasma. *Physics of Plasmas*, 25(3), mar 2018.

[43] Peter V. Heuer, Martin. S. Weidl, Robert S. Dorst, Derek B. Schaeffer, Shreekrishna K. P. Tripathi, Stephen Vincena, Carmen G. Constantin, Christoph Niemann, Lynn B. Wilson III, and Dan Winske. Laboratory observations of ultra-low-frequency analog waves driven by the right-hand resonant ion beam instability. *The Astrophysical Journal*, 891(1):L11, feb 2020.

[44] P.V. Heuer, D.B. Schaeffer, E.N. Knall, C.G. Constantin, L.R. Hofer, S. Vincena, S. Tripathi, and C. Niemann. Fast gated imaging of the collisionless interaction of a laser-produced and magnetized ambient plasma. *High Energy Density Physics*, 22:17–20, mar 2017.

[45] UCLA Marginalized Identies in Physics and Astronomy. https://mipa.pa.ucla.edu/. website.

[46] Tsuyoshi Inoue, Ryo Yamazaki, and Shu ichiro Inutsuka. TURBULENCE AND MAGNETIC FIELD AMPLIFICATION IN SUPERNOVA REMNANTS: INTERACTIONS BETWEEN a STRONG SHOCK WAVE AND MULTIPHASE INTERSTELLAR MEDIUM. *The Astrophysical Journal*, 695(2):825–833, apr 2009.

[47] M. Kaloyan, S. Ghazaryan, C. G. Constantin, R. S. Dorst, P. V. Heuer, J. J. Pilgram, D. B. Schaeffer, and C. Niemann. Raster thomson scattering in large-scale laser plasmas produced at high repetition rate. *Review of Scientific Instruments*, 92(9):093102, sep 2021.

[48] Marietta Kaloyan, Sofiya Ghazaryan, Shreekrishna P. Tripathi, Walter Gekelman, Mychal J. Valle, Byonghoon Seo, and Christoph Niemann. First results from the thomson scattering diagnostic on the large plasma device. *Instruments*, 6(2):17, apr 2022.

[49] Richard I. Klein and D. Tod Woods. Bending mode instabilities and fragmentation in interstellar cloud collisions: A mechanism for complex structure. *The Astrophysical Journal*, 497(2):777–799, apr 1998.

[50] Russell M. Kulsrud, Renyue Cen, Jeremiah P. Ostriker, and Dongsu Ryu. The protogalactic origin for cosmic magnetic fields. *The Astrophysical Journal*, 480(2):481–491, may 1997.

[51] Russell M Kulsrud and Ellen G Zweibel. On the origin of cosmic magnetic fields. *Reports on Progress in Physics*, 71(4):046901, mar 2008.

[52] L.D. Landau and E.M. Lifshitz. *Fluid Mechanics*. Pergamon Press Ltd., 3 edition, 1959.

[53] Dongwook Lee. A solution accurate, efficient and stable unsplit staggered mesh scheme for three dimensional magnetohydrodynamics. *Journal of Computational Physics*, 243:269–292, jun 2013.

[54] M. M. Leroy, D. Winske, C. C. Goodrich, C. S. Wu, and K. Papadopoulos. The structure of perpendicular bow shocks. *Journal of Geophysical Research: Space Physics*, 87(A7):5081–5094, jul 1982.

[55] C. K. Li, F. H. Séguin, J. R. Rygg, J. A. Frenje, M. Manuel, R. D. Petrasso, R. Betti, J. Delettrez, J. P. Knauer, F. Marshall, D. D. Meyerhofer, D. Shvarts, V. A. Smalyuk, C. Stoeckl, O. L. Landen, R. P. J. Town, C. A. Back, and J. D. Kilkenny. Monoenergetic-proton-radiography measurements of implosion dynamics in direct-drive inertial-confinement fusion. *Physical Review Letters*, 100(22), jun 2008.

[56] C. K. Li, P. Tzeferacos, D. Lamb, G. Gregori, P. A. Norreys, M. J. Rosenberg, R. K. Follett, D. H. Froula, M. Koenig, F. H. Seguin, J. A. Frenje, H. G. Rinderknecht, H. Sio, A. B. Zylstra, R. D. Petrasso, P. A. Amendt, H. S. Park, B. A. Remington, D. D. Ryutov, S. C. Wilks, R. Betti, A. Frank, S. X. Hu, T. C. Sangster, P. Hartigan, R. P. Drake, C. C. Kuranz, S. V. Lebedev, and N. C. Woolsey. Scaled laboratory experiments

explain the kink behaviour of the crab nebula jet. *Nature Communications*, 7(1), oct 2016.

[57] A Marocchino, S Atzeni, and A Schiavi. Magnetic field generation and diffusion by a laser-produced blast wave propagating in non-homogenous plasma. *New Journal of Physics*, 17(4):043052, apr 2015.

[58] J. Matteucci, W. Fox, A. Bhattacharjee, D. B. Schaeffer, C. Moissard, K. Germaschewski, G. Fiksel, and S. X. Hu. Biermann-battery-mediated magnetic reconnection in 3d colliding plasmas. *Physical Review Letters*, 121(9), aug 2018.

[59] Jackson Van Horn Matteucci. *Magnetic Field Generation and Reconnection in High Energy Density Plasmas*. Thesis, Princeton University, April 2020.

[60] Christopher F. McKee and Bruce T. Draine. Interstellar shock waves. *Science*, 252(5004):397–403, apr 1991.

[61] L. L. Mckee, R. S. Bird, and F. Schwirzke. Self-generated magnetic fields associated with a laser-produced plasma. *Physical Review A*, 9(3):1305–1311, mar 1974.

[62] E. A. McLean, J. A. Stamper, C. K. Manka, H. R. Griem, D. W. Droemer, and B. H. Ripin. Observation of magnetic fields in laser-produced plasma using the zeeman effect. *Physics of Fluids*, 27(5):1327, 1984.

[63] J. Meinecke, H. W. Doyle, F. Miniati, A. R. Bell, R. Bingham, R. Crowston, R. P. Drake, M. Fatenejad, M. Koenig, Y. Kuramitsu, C. C. Kuranz, D. Q. Lamb, D. Lee, M. J. MacDonald, C. D. Murphy, H-S. Park, A. Pelka, A. Ravasio, Y. Sakawa, A. A. Schekochihin, A. Scopatz, P. Tzeferacos, W. C. Wan, N. C. Woolsey, R. Yurchak, B. Reville, and G. Gregori. Turbulent amplification of magnetic fields in laboratory laser-produced shock waves. *Nature Physics*, 10(7):520–524, jun 2014.

[64] Jena Meinecke, Petros Tzeferacos, Anthony Bell, Robert Bingham, Robert Clarke, Eugene Churazov, Robert Crowston, Hugo Doyle, R. Paul Drake, Robert Heathcote, Michel Koenig, Yasuhiro Kuramitsu, Carolyn Kuranz, Dongwook Lee, Michael MacDonald, Christopher Murphy, Margaret Notley, Hye-Sook Park, Alexander Pelka, Alessandra Ravasio, Brian Reville, Youichi Sakawa, Willow Wan, Nigel Woolsey, Roman Yurchak, Francesco Miniati, Alexander Schekochihin, Don Lamb, and Gianluca Gregori. Developed turbulence and nonlinear amplification of magnetic fields in laboratory and astrophysical plasmas. *Proceedings of the National Academy of Sciences*, 112(27):8211–8215, jun 2015.

[65] B. Meyer and G. Thiell. Experimental scaling laws for ablation parameters in plane target–laser interaction with 1.06 μm and 0.35 μm laser wavelengths. *Physics of Fluids*, 27(1):302, 1984.

[66] Francesco Miniati and A. R. Bell. RESISTIVE MAGNETIC FIELD GENERATION AT COSMIC DAWN. *The Astrophysical Journal*, 729(1):73, feb 2011.

[67] Smadar Naoz and Ramesh Narayan. Generation of primordial magnetic fields on linear overdensity scales. *Physical Review Letters*, 111(5), jul 2013.

[68] C Niemann, C G Constantin, D B Schaeffer, A Tauschwitz, T Weiland, Z Lucky, W Gekelman, E T Everson, and D Winske. High-energy nd:glass laser facility for collisionless laboratory astrophysics. *Journal of Instrumentation*, 7(03):P03010–P03010, mar 2012.

[69] C. Niemann, W. Gekelman, C. G. Constantin, E. T. Everson, D. B. Schaeffer, A. S. Bondarenko, S. E. Clark, D. Winske, S. Vincena, B. Van Compernolle, and P. Pribyl. Observation of collisionless shocks in a large current-free laboratory plasma. *Geophysical Research Letters*, 41(21):7413–7418, nov 2014.

[70] C. Niemann, W. Gekelman, C. G. Constantin, E. T. Everson, D. B. Schaeffer, S. E. Clark, D. Winske, A. B. Zylstra, P. Pribyl, S. K. P. Tripathi, D. Larson, S. H. Glenzer, and A. S. Bondarenko. Dynamics of exploding plasmas in a large magnetized plasma. *Physics of Plasmas*, 20(1), jan 2013.

[71] P. M. Nilson, L. Willingale, M. C. Kaluza, C. Kamperidis, S. Minardi, M. S. Wei, P. Fernandes, M. Notley, S. Bandyopadhyay, M. Sherlock, R. J. Kingham, M. Tatarakis, Z. Najmudin, W. Rozmus, R. G. Evans, M. G. Haines, A. E. Dangor, and K. Krushelnick. Magnetic reconnection and plasma dynamics in two-beam laser-solid interactions. *Physical Review Letters*, 97(25), dec 2006.

[72] Chris Orban, Milad Fatenejad, Sugreev Chawla, Scott C. Wilks, and Donald Q. Lamb. A radiation-hydrodynamics code comparison for laser-produced plasmas: Flash versus hydra and the results of validation experiments. *arXiv1306.1584v1 [physics.plasm-ph]*, June 2013.

[73] Mike C. Parent, Cirleen DeBlaere, and Bonnie Moradi. Approaches to research on intersectionality: Perspectives on gender, LGBT, and racial/ethnic identities. *Sex Roles*, 68(11-12):639–645, apr 2013.

[74] J.J. Pilgram, M. B. P. Adams, C. G. Constantin, P. V. Heuer, S. Ghazaryan, M. Kaloyan, R. S. Dorst, D. B. Schaeffer, P. Tzeferacos, and C. Niemann. High repetition rate exploration of the biermann battery effect in laser produced plasmas over large spatial regions. *High Power Laser Science and Engineering*, pages 1–11, feb 2022.

[75] T. Pisarczyk, S. Yu. Gus'kov, R. Dudzak, T. Chodukowski, J. Dostal, N. N. Demchenko, Ph. Korneev, Z. Kalinowska, M. Kalal, O. Renner, M. Smid, S. Borodziuk, E. Krousky, J. Ullschmied, J. Hrebicek, T. Medrik, J. Golasowski, M. Pfeifer, J. Skala, and P. Pisarczyk. Space-time resolved measurements of spontaneous magnetic fields in laser-produced plasma. *Physics of Plasmas*, 22(10):102706, oct 2015.

[76] Richard J. Rand and Shrinivas R. Kulkarni. The local galactic magnetic field. *The Astrophysical Journal*, 343:760, aug 1989.

[77] A. Raven, O. Willi, and P. T. Rumsby. Megagauss magnetic field profiles in laser-produced plasmas. *Physical Review Letters*, 41(8):554–557, aug 1978.

[78] Bruce A. Remington, R. Paul Drake, Hideaki Takabe, and David Arnett. A review of astrophysics experiments on intense lasers. *Physics of Plasmas*, 7(5):1641–1652, may 2000.

[79] D. D. Ryutov, B. A. Remington, H. F. Robey, and R. P. Drake. Magnetohydrodynamic scaling: From astrophysics to the laboratory. *Physics of Plasmas*, 8(5):1804–1816, may 2001.

[80] D. B. Schaeffer, A. S. Bondarenko, E. T. Everson, S. E. Clark, C. G. Constantin, and C. Niemann. Characterization of laser-produced carbon plasmas relevant to laboratory astrophysics. *Journal of Applied Physics*, 120(4):043301, jul 2016.

[81] D. B. Schaeffer, E. T. Everson, D. Winske, C. G. Constantin, A. S. Bondarenko, L. A. Morton, K. A. Flippo, D. S. Montgomery, S. A. Gaillard, and C. Niemann. Generation of magnetized collisionless shocks by a novel, laser-driven magnetic piston. *Physics of Plasmas*, 19(7), jul 2012.

[82] D. B. Schaeffer, D. Winske, D. J. Larson, M. M. Cowee, C. G. Constantin, A. S. Bondarenko, S. E. Clark, and C. Niemann. On the generation of magnetized collisionless shocks in the large plasma device. *Physics of Plasmas*, 24(4):041405, apr 2017.

[83] K. M. Schoeffler, N. F. Loureiro, R. A. Fonseca, and L. O. Silva. The generation of magnetic fields by the biermann battery and the interplay with the weibel instability. *Physics of Plasmas*, 23(5):056304, may 2016.

[84] K. M. Schoeffler, N. F. Loureiro, R. A. Fonseca, and L. O. Silva. Magnetic-field generation and amplification in an expanding plasma. *Physical Review Letters*, 112(17), apr 2014.

[85] L.I. Sedov. Foreword to first edition. In *Similarity and Dimensional Methods in Mechanics*, pages ix–x. Elsevier, 1959.

[86] John Sheffield, Dustin Froula, Siegfried H Glenzer, and Neville C Luhmann Jr. *Plasma scattering of electromagnetic radiation: theory and measurement techniques*. Academic press, 2010.

[87] R. K. Singh, O. W. Holland, and J. Narayan. Theoretical model for deposition of superconducting thin films using pulsed laser evaporation technique. *Journal of Applied Physics*, 68(1):233–247, July 1990.

[88] Rajiv K. Singh and J. Narayan. Pulsed-laser evaporation technique for deposition of thin films: Physics and theoretical model. *Physical Review B*, 41(13):8843–8859, May 1990.

[89] E.E. Slapeter. Electron density flucuations in a plasma. *Physical Review*, 5(120):1528–1535, December 1960.

[90] J. A. Stamper. Review on spontaneous magnetic fields in laser-produced plasmas: Phenomena and measurements. *Laser and Particle Beams*, 9(4):841–862, dec 1991.

[91] J. A. Stamper, K. Papadopoulos, R. N. Sudan, S. O. Dean, E. A. McLean, and J. M. Dawson. Spontaneous magnetic fields in laser-produced plasmas. *Physical Review Letters*, 26(17):1012–1015, apr 1971.

[92] J. A. Stamper and B.H. Ripin. Faraday-rotation measurements of megagauss magnetic fields in laser-produced plasmas. *Physical Review Letters*, 1974.

[93] James M. Stone and Micheal L. Norman. The three-dimensional interaction of a supernova remnant with an interstellar cloud. *The Astrophysical Journal*, 390:L17–L19, May 1992.

[94] E. R. Tubman, R. H. H. Scott, H. W. Doyle, J. Meinecke, H. Ahmed, R. A. B. Alraddadi, R. Bolis, J. E. Cross, R. Crowston, D. Doria, D. Lamb, B. Reville, A. P. L. Robinson, P. Tzeferacos, M. Borghesi, G. Gregori, and N. C. Woolsey. Time evolution and asymmetry of a laser produced blast wave. *Physics of Plasmas*, 24(10):103124, oct 2017.

[95] P. Tzeferacos, M. Fatenejad, N. Flocke, C. Graziani, G. Gregori, D.Q. Lamb, D. Lee, J. Meinecke, A. Scopatz, and K. Weide. FLASH MHD simulations of experiments that study shock-generated magnetic fields. *High Energy Density Physics*, 17:24–31, dec 2015.

[96] P. Tzeferacos, A. Rigby, A. Bott, A. R. Bell, R. Bingham, A. Casner, F. Cattaneo, E. M. Churazov, J. Emig, N. Flocke, F. Fiuza, C. B. Forest, J. Foster, C. Graziani, J. Katz, M. Koenig, C.-K. Li, J. Meinecke, R. Petrasso, H.-S. Park, B. A. Remington, J. S. Ross, D. Ryu, D. Ryutov, K. Weide, T. G. White, B. Reville, F. Miniati, A. A. Schekochihin, D. H. Froula, G. Gregori, and D. Q. Lamb. Numerical modeling of laser-driven experiments aiming to demonstrate magnetic field amplification via turbulent dynamo. *Physics of Plasmas*, 24(4), mar 2017.

[97] P. Tzeferacos, A. Rigby, A. F. A. Bott, A. R. Bell, R. Bingham, A. Casner, F. Cattaneo, E. M. Churazov, J. Emig, F. Fiuza, C. B. Forest, J. Foster, C. Graziani, J. Katz, M. Koenig, C.-K. Li, J. Meinecke, R. Petrasso, H.-S. Park, B. A. Remington, J. S. Ross, D. Ryu, D. Ryutov, T. G. White, B. Reville, F. Miniati, A. A. Schekochihin, D. Q. Lamb, D. H. Froula, and G. Gregori. Laboratory evidence of dynamo amplification of magnetic fields in a turbulent plasma. *Nature Communications*, 9(1), feb 2018.

[98] T. Ueta, R. E. Stencel, I. Yamamura, K. M. Geise, A. Karska, H. Izumiura, Y. Nakada, M. Matsuura, Y. Ita, T. Tanabé, H. Fukushi, N. Matsunaga, H. Mito, and A. K. Speck. The interface between the stellar wind and interstellar medium around r cassiopeiae revealed by far-infrared imaging. *Astronomy and Astrophysics*, 514:A16, may 2010.

[99] Tessa Vernstrom, Jennifer West, Franco Vazza, Denis Wittor, Christopher John Riseley, and George Heald. Polarized accretion shocks from the cosmic web. *Science Advances*, 9(7), feb 2023.

[100] C. A. Walsh, J. P. Chittenden, K. McGlinchey, N. P. L. Niasse, and B. D. Appelbe. Self-generated magnetic fields in the stagnation phase of indirect-drive implosions on the national ignition facility. *Physical Review Letters*, 118(15), apr 2017.

[101] Dan Winske, Joseph D. Huba, Christoph Niemann, and Ari Le. Recalling and updating research on diamagnetic cavities: Experiments, theory, simulations. *Frontiers in Astronomy and Space Sciences*, 5, jan 2019.

[102] Ya.P. Zel'dovich and Yu.P. Raizer. *Physics of Shock Waves and High-Temperature Hydrodynamic Phenomena*. Elsevier, 1967.

[103] Haiping Zhang, Jessica J. Pilgram, Carmen G. Constantin, Lucas Rovige, Peter V. Heuer, Sofiya Ghazaryan, Marietta Kaloyan, Robert S. Dorst, Derek B. Schaeffer, and Christoph Niemann. Two-dimensional thomson scattering in laser-produced plasmas. *Instruments*, 7(3):25, sep 2023.

[104] Ellen Zweibel. The seeds of a magnetic universe. *Physics*, 6, jul 2013.

[105] Ellen G. Zweibel and Carl Heiles. Magnetic fields in galaxies and beyond. *Nature*, 385(6612):131–136, jan 1997.